The role of atomic excited states in laboratory plasmas and a study in fine structure diagnostics for far infra-red astrophysical observations

by

A. Jonathan Pearce

A dissertation submitted to the Graduate Faculty of
Auburn University
in partial fulfillment of the
requirements for the Degree of
Doctor of Philosophy

Auburn, Alabama
December 10, 2016

Keywords: electron-impact ionization, electron-impact excitation, fusion plasmas, astrophysical plasmas, C^+, Ar^{2+}

Approved by

Stuart Loch, Chair, Associate Professor of Physics
Connor Ballance, Associate Professor of Physics
David Ennis, Assistant Professor of Physics
Mike Fogle, Associate Professor of Physics
Hans-Werner van Wyk, Assistant Professor of Mathematics

Abstract

This dissertation has a focus on the role of atomic excited states in laboratory and astrophysical plasmas. The emphasis is on systems for which perturbation theory is not expected to produce accurate results. The work includes new electron-impact excitation and ionization data for C^+, which is used to produce density and temperature dependent generalized collisional radiative coefficients that can be used for C II spectral diagnostics and C impurity transport. We compare excitation and ionization cross sections with existing calculations and experimental results finding reasonable agreement (within ∼10–15%) for the transitions involving the lower excited states. However, for transitions involving highly excited states ($n > 3$) the existing electron-impact excitation rate data are from perturbative plane-wave Born calculations and the results from our non-perturbative approach differ greatly. This leads to differences with the currently used ADAS excitation rate coefficients that can be larger than a factor of 10 for these higher n-shells.

The issue of final state resolution for C^+ excited state ionization is also explored, and evidence is presented that some excited states are unable to ionize directly to the ground term of C^{2+}, instead ionizing to the C^{2+} metastable term. Additionally, we show that the non-perturbative R-Matrix method can resolve both the initial and the final metastable states in the ionization cross sections. For instance, ionization from the $1s^2 2s^2 2p(^2P^o)$ term of C^+ has a ∼30% peak contribution from the direct ionization to the ground term of C^{2+}, ∼20% peak contribution from the direction ionization to the metastable term of C^{2+}, and ∼50% contribution from the indirect (excitation-autoionization) processes. Resolution of these final states has significant consequences for impurity transport modeling in laboratory fusion experiments and astrophysical spectroscopy. The dissertation presents an overview of

the main differences between these new atomic generalized collisional-radiative rate coefficients and the data currently used in the ADAS database.

A study is also presented for neutral N ionization as it introduces a number of scenarios not previously encountered in generalized collisional-radiative modeling. The final-state resolution issues presented for C^+ are more involved for N and this work is used to outline the methodology for dealing with ionization processes requiring careful consideration of the possible final states, allowing future non-perturbative calculations to fit into the metastable resolved generalized collisional-radiative picture.

The remaining topic of this dissertation is the calculation of new fine-structure electron-impact excitation collision strengths for the ground term of Ar^{2+} for applications in very low temperature astrophysical plasmas that emit in the far-IR and near UV. The temperature range of interest for this work is 10–1,000K, noting that existing atomic data has not been calculated for temperatures lower than 1,800K. The challenge in diagnosing such low temperature plasmas is that the contribution to the cross section from the indirect processes is expected to be very significant, so particular care was given to the resolution of the resonance structure. A progressively finer energy mesh was applied until differences upon successive iterations dropped to less than 0.1%, which resulted in a mesh spacing of 2–40 μeV for the relevant transitions. This fine resolution allowed us to deduce the behavior of the rate coefficients in the 50–100K temperature range that differed significantly from the apparent trends implied by the existing atomic data - by roughly 20%. We evaluate Breit-Pauli R-matrix and Dirac R-matrix calculations, using a comparison of the two datasets to determine the likely uncertainties on the recommended dataset. These uncertainties are typically less than 10% for the temperature range of interest.

Acknowledgments

Working towards a Ph.D. is a long and arduous process and I would not have made it through without a great deal of support.

I would first like to thank the Astronomy and Physics Research and Analysis Program (APRA) of the National Aeronautics and Space Admininstration (NASA) for funding my research and the Auburn University Physics Department for financial assistance in the early stages of my graduate career.

I would like to extend my gratitude to Dr. Stuart Loch, my research supervisor and graduate advisor. Supervising a graduate student is always a significant undertaking; supervising a graduate student who moves 1,300 miles away for the final two years of their studies is another thing entirely. Between early morning Skype conferences, late night edits, long discussions about physics theory, and conversations on teaching pedagogy, Stuart has done more to shape my professional path over the past six years than anyone else and I am extremely grateful for all of his work.

Throughout graduate school, I always claimed that I had a second supervisor in Dr. Connor Ballance. He has helped me learn more about programming, analysis, and the gritty details of the math behind the physics than I could have hoped to learn on my own. He even went so far as to create an unofficial course on R-matrix theory so that three clueless grad students could develop in our field. I appreciate all of his work and his patience in dealing with my never-ending stream of questions.

I would also like to thank the other members of my committee: Drs. Michael Fogle, David Ennis, and Hans Werner van Wyk. I appreciate their time and the lending of their expertise.

Next, I would like to thank the faculty and staff of the Bowdoin College Department of Physics and Astronomy for their patience as I struggled through the past couple of years. I am especially grateful to Emily Briley for her constant encouragement and Drs. Karen Topp, Thomas Baumgarte, Juan Burciaga, and Stephen Naculich who graciously gave their time to sit through - and suggest improvements to - a very rough first draft of my defense presentation.

I do not have a large family, but I have never lacked for support. My mother, Linda Pearce, has worked tirelessly her entire life to provide for my brother and me. She has always overflowed with love and encouragement and never once allowed me to doubt myself and I will always be grateful for her. My father, Chuck Pearce, uniquely understood me. He pushed, challenged, and inspired me and I would not be where I am now without him. I miss him daily and I hope he would be proud of me. The rest of my close family - Bradley and Britney (and Caden and Hannah) Pearce, Kay Kay Green, LaVon and Sandi Chastang, and Becky Britton - have always provided a steadying presence for me by the simple and profoundly comforting fact that finishing my Ph.D. was a given in their eyes. I am also very lucky to have a wonderful group of in-laws whose positivity provides me constant reassurance. My entire family's unwavering belief in me is both humbling and encouraging and I am indebted to them all.

I am fortunate to have a similarly comforting group of friends, both fellow grad students who have provided various means of support and stress relief as we have all pushed through our respective programs and those that I made outside of grad school. In particular, I can confidently state that I would not have passed my qualifying exams were it not for Ivan Arnold and his absurdly complete problem sets, makeshift whiteboards, and very strong (and occassionally quite terrible) cups of coffee. Additionally, Meagan Davis and Michael Owens have at various times propped me up when I needed more help than I knew how to ask for. I am grateful for them and for the support from all of my friends - old, new, and a few that are no longer in my life. Thank you all.

At the end of my first year in grad school, I had a chance encounter with an amazing woman who has become more to me than I could have imagined. My wife, Patricia, pushes and challenges me, and supports me by never letting me consider settling for less than what I can be. She is my lodestone, my compass, and my peace. I am grateful to have her in my life.

And, finally, to my son, Charlie. You're already inspiring me to be better and we haven't even met yet.

Table of Contents

List of Figures

List of Tables

Chapter 1

Introduction and theory

1.1 Introduction

The focus of this dissertation is the creation of new atomic cross sections and rate coefficients to investigate the role of atomic excited states with applications in laboratory fusion plasmas and in astrophysical plasmas. For the former, we will focus on C^+ atomic data for use in impurity transport in laboratory fusion plasmas. This requires the creation of new electron-impact excitation and ionization data for singly-ionized carbon. For the latter, we will apply our new excitation and ionization data for carbon and create new atomic data for the fine-structure transitions in the ground state of doubly-ionized argon for very low temperature interstellar environments.

An interesting issue arises in the C^+ ionization study regarding resolving the final states in the ionization processes. This issue is much more pronounced for neutral nitrogen. Thus, the lessons from C^+ ionization are explored in more depth for N, with both C^+ and N presenting several new issues not previously encountered in the use non-perturbative data in generalized collisional-radiative modeling. The nitrogen case is used to develop a framework within which future non-perturbative calculations can address this issue of final state resolution in the ionization cross sections.

In this chapter, we provide an overview of the relevant plasma environments and a description of the theoretical methods used to calculate the atomic data and the spectral modeling. In chapters 2 and 3, we describe the R-matrix calculations used to evaluate the new cross-sections and rate coefficients for the electron-impact excitation and ionization of

C^+ and compare with both literature values and the current ADAS data. ADAS (Atomic Data and Analysis Structure) is a suite of codes and an associated database that is used for plasma spectral diagnostics and modeling [1]. In chapter 4, we apply a generalized collisional-radiative (GCR) model to generate GCR coefficients for C^+, comparing with existing ADAS data. The current ADAS data has been used on a wide range of fusion and astrophysical studies [2, 3, 4, 5]. Chapter 5 contains the new cross-section and effective collision strengths for Ar^{2+}. Our discussion of the final-state resolution of excited state ionization of N and the implications for similar systems can be found in Chapter 6. Finally, we present our conclusions and future work in Chapter 7.

1.1.1 Impurities in laboratory plasmas

Magnetically confined plasmas for fusion energy have been the subject of research for more than 50 years. The ultimate goal is to magnetically confine a plasma that is of sufficient temperature such that tritium and deuterium can fuse. A number of confinement schemes have been developed, with tokamaks and stellarators currently the most viable candidates for fusion energy. The ITER device currently under construction in Caradache, France is the newest tokamak experiment, while the W-7X facility in Germany is the latest stellarator experiment.

One critical issue for such experiments is the radiative power loss due to impurities in the plasma core. This radiation is driven by collisional excitation and carries energy away from the plasma core, which can then destabilize the plasma and quench the fusion reaction. Since these impurities largely originate from the walls of the containment vessel, understanding both the rates at which they enter the plasma and the subsequent transport from the edge to the core is crucial to establishing a sustained fusion reaction. There are many codes that attempt to model impurity transport (SANCO[6], SOLPS[7], TRANSP[8], XGC[9]) and they all depend on accurate atomic data. Of specific use are effective ionization

and recombination rate coefficients, which are used directly in these codes.

Impurities ablated from the chamber walls enter the plasma at neutral or near-neutral ion stages and rapidly encounter a sharp temperature gradient, from $T_e = \ 1 - 10$ eV at the edge to $T_e = \ 10 - 20$ keV in the plasma core. Because of the high speed of these ablated impurities, these ions can remain in these near neutral stages as they are transported into the plasma and experience temperatures that are sufficient to ionize them. Thus, it is important to produce accurate ionization and recombination rate coefficients to allow the aforementioned impurity transport codes to be able to predict what charge states of each impurity will be transported into the plasma core.

When a plasma destabilizes, the energy contained in the tokamak plasma is primarily deposited in the vessel walls. Until recently, these plasma facing components (PFCs) were made of a Carbon-Fiber Composite (CFC), but the plasma produced by ITER will contain too much energy for walls made from these lighter elements to be viable long-term. Ultimately, ITER will use heavier metals, such as tungsten, in the PFCs. Calculations using existing atomic data alongside theoretical values for radiative power loss show that tungsten impurity ratios of 1.9×10^{-4} under ITER conditions would be sufficient to quench the fusion reaction [2, 3]. Given the importance and potential of the ITER device, many other tokamak research facilities (for example, the JET tokamak in Oxforshire, UK) have switched to these heavier metals.

However, the DIII-D tokamak (see Fig 1.1) in San Diego, CA and the NSTX-Upgrade experiment at the Princeton Plasma Physics Lab still use CFC panels in the walls and will continue to do so for the near future[10]. It is in support of these tokamaks that we produce high quality atomic data for carbon. Our GCR data will be especially useful when applied to the impurity transport models to calculate how much carbon will make it into the plasma

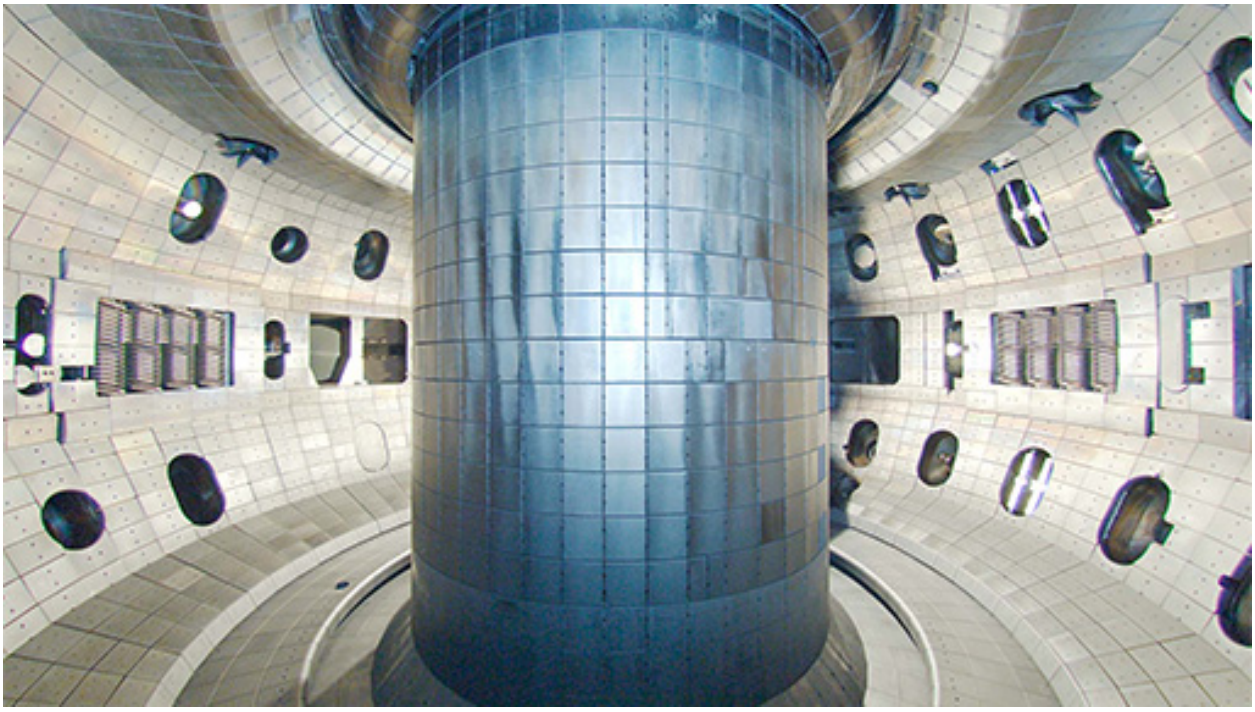

Figure 1.1: Interior of the DIII-D tokamak device in San Diego, CA. Taken from U.S. Department of Energy, http://science.energy.gov/

core.

1.1.2 Astrophysical plasmas

Carbon in astrophysical plasmas

Carbon is also useful for analysis of astrophysical objects. This is partially because carbon is one of the most abundant elements in the universe [11] and this prevalence allows for it to be frequently used as a diagnostic. Singly-ionized carbon is particularly useful because of it's relatively high ionization energy (24.4 eV) as compared to that of neutral carbon (11.3 eV). This energy difference is noteworthy because of the relationship with the ionization potential of hydrogen (13.6 eV) - higher than that of neutral carbon. Thus singly-ionized carbon can be abundant - and can thus be used as a diagnostic - in both H I [12] and H II [13] regions. The C^+ atomic data produced for this dissertation will therefore also be useful

for the analysis of astrophysical plasmas.

For specific examples: calculations for the electron density in the chromospheres of giant and supergiant stars relies on emission lines resulting from transitions between the C II $1s^2 2s^2 2p$ (^{2}P) and $1s^2 2s 2p^2$ (^{4}P) multiplets [14]. The CII 1334.5 Åspectral line, originating from the $1s^2 2s^2 2p$ ($^2P^0_{1/2}$) $\rightarrow$ $1s^2 2s 2p^2$ ($^2D_{3/2}$) transition has been used in recent study of the solar chromosphere and chromosphere-corona transition region [15] and the transitions between the $^2P^o_j \rightarrow {}^2D_{j'}$ multiplets have been used in elemental abundance calculations of planetary nebulae [16]. All of the aforementioned transitions as well as those from the $1s^2 2s^2 2p$ ($^2P^0_j$) $\rightarrow$ $1s^2 2s 2p^2$ ($^2S_{1/2}$) multiplet have been used for analysis of the solar chromosphere and transition regions [17]. Because these transitions are used as astrophysical diagnostics, many in the lower-energy multiplets have been thoroughly investigated by prior calculations, providing a useful benchmark for our calculations, which have been extended to higher n-shells.

A common approach when evaluating atomic processes in the low-density, high-temperature environments common in astrophysics (e.g. upper stellar atmospheres) is to apply the coronal approximation. Since it only allows for population of excited states by collisional excitation from the ground and depopulation by radiative decay, this approach ignores density-dependent effects; it specifically neglects collisional redistribution among excited states and the population of metastable states, which lead to errors in ion balance calculations. It has been shown that the error in calculating the differential emission measure for Li-like ions by neglecting these density-dependent effects is as large as a factor of 2 or 3 [4].

Given the more involved electron structure, we expect that the ionization balance between lower charge states (such as singly-ionized carbon) should be more sensitive to electron density, thus accounting for density-dependent effects is crucial for accurate spectroscopic analysis. For this reason, we generate temperature and density dependent generalized collisional-radiative coefficients for C^+ in this work.

Argon in astrophysical plasmas

Fine-structure excitation of atoms and ions due to collisions with electrons and the dominant neutral species provides the primary cooling mechanism in most interstellar environments. In diffuse and translucent clouds, atomic hydrogen collisions dominate, while H_2 collisions can be important in dense clouds and molecular regions. For regions where there is a significant ionization fraction, electron and proton collisions become important and may be the primary colliders in, for example, photoionized gas. Fine-structure excitation also plays a role in interpreting ultraviolet (UV) absorption lines which are split due to the fine structure of the ground state. Intensity ratios from fine-structure lines are used to deduce the density, pressure, temperature, and/or ambient radiation fields.

The fine-structure lines from neutral atoms and low-charged ions are primarily observable from the infrared (IR) to the submillimeter (submm), therefore falling within the detector windows of the *Spitzer Space Telescope*, the *Stratospheric Observatory for Infrared Astronomy (SOFIA)*, the *Herschel Space observatory*, and the up-coming *James Webb Space Telescope (JWST)*. As an example, Fig. 1.2 shows an IR spectrum of the Circinus galaxy observed with the European *Infrared Space Observatory (ISO)*.

Current models of interstellar environments adopt rate coefficients for fine-structure excitation (mostly due to atomic hydrogen) using a simple model developed by Bahcall & Wolf

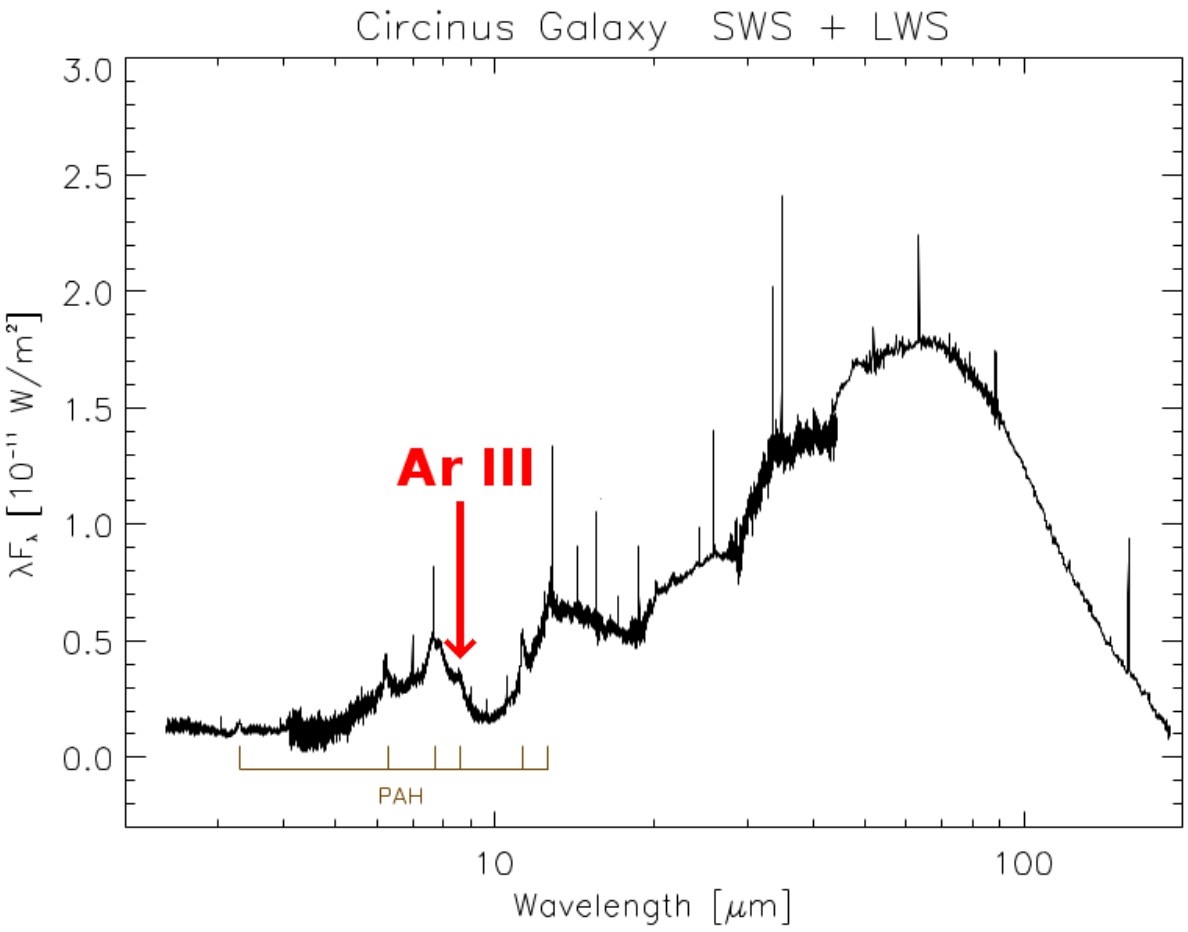

Figure 1.2: Observation of the Circinus Galaxy with *ISO*.

[18], when explicit calculations are not available (see, for example, Table 4 of Tielens & Hollenbach [19]). It should be noted that this process is difficult to measure in the laboratory and little, if any, experimental data exist. Meijerink et al. [20] have pointed out that comparison of rate coefficients using the Bahall-Wolf model to detailed quantum calculations, $C^+ + H$ for example (Barinovs et al. [21]), find the former overestimates the rate coefficients by nearly an order of magnitude over the temperature range 500-4000 K.

Work on H^+, He, and H_2 is rare, while electron collisions for fine-structure excitation have been studied fairly extensively[5]. However, electron collision calculations have primarily focused on higher energies relevant to collisionally-ionized plasmas for energy research or for relatively simple atomic ions. A review of the status of fine-structure excitation rate coefficients for astrophysics was given in the 2010 NASA Laboratory Astrophysics Workshop (Savin et al [22]) by Stancil [23]. Our collaborators are working on improving the fine-structure ion collisional data, while this dissertation focuses on the electron-impact of Ar^{2+}.

From a quantum mechanical standpoint, transitions within the same ground term do not involve a change of parity and therefore the resulting background cross-sections are typically small and can be strongly influenced by Rydberg resonance structure. Further, since the ground term target levels are close to degenerate, this also implies a strong background cross section at low energies. For Ar^{2+}, the ground configuration is $1s^2 2s^2 2p^6 3s^2 3p^4$, which results in 5 J-resolved levels in these terms: ${}^3P_{2,1,0}, {}^1D_2, {}^1S_0$. The electron-impact excitation of Ar^{2+} as investigated by Munoz Burgos et al. [5] highlights an important issue. They found that in the $3p^4({}^1D_2) - 3p^4({}^1S_0)$ transition a *single* $3s3p^5 3d$ resonance line very close to the upper excitation threshold was enough to change the excitation rate by a factor of two (see Fig. 3 and Fig. 5 in [5]) depending on whether it was below or above an excitation threshold. In fact, due to the temperature and density diagnostic potential of Ar^{2+} this was reanalyzed by

Stancalie et al [24], who independently verified Munoz Burgos' conclusion. These resonance positions, especially those with a low principal quantum number are directly correlated to the accuracy of the underlying atomic structure, which must be given due consideration.

To the best of our knowledge, there are no experimental measurements of excitation cross sections for Ar^{2+}. Additionally, the existing theoretical data were intended for diagnostic use on collisionally-ionized fusion plasmas or on higher-temperature astrophysical plasmas and thus are focused on higher energies than is needed for astrophysical diagnostics. In this work, we evaluate both semi-relativistic and relativistic atomic structure for Ar^{2+} as a basis for R-Matrix scattering calculations with a very fine energy mesh to allow for the resolution of resonances and the ultimate determination of thermal rate coefficients from 200K to 2,000K. These calculations are completely independent of each other, providing the ability to cross-check and evaluate the sensitivity of the final collisional rate to the underlying atomic structure and resonance positions from both approaches.

1.2 Theory

1.2.1 Atomic processes

Electron-impact ionization

The primary contributions to the electron-impact ionization are from the direct ionization process:

$$e^- + X^Z \rightarrow X^{Z+1} + e^- + e^- \tag{1.1}$$

where Z is the charge state, and from the indirect process of electron-impact excitation followed by direct autoionization or autoionization via Auger decay:

$$e^- + X^Z(j) \rightarrow X^Z(i) + e^- \rightarrow X^{Z+1} + e^- + e^- \tag{1.2}$$

where $X(j)$ is the initial level of the target ion, $X^Z(i)$ is an excited (autoionizing) state, $X^{Z+1}$the next ion stage of X. It is also possible that the excited ion, $X^Z(i)$, can radiatively stabilize to a non-autoionizing state, however for low charge states the radiative rates are typically orders of magnitude lower than the autoionizing and Auger rates, so we can safely assume that the contribution from autoionizing states is 100%. We discuss the lifetimes of the atomic and plasma processes in more detail in section 1.2.2.

In equation 1.2, it is possible for the electron in the first step to capture into the ion X (i.e. dielectronic recombination), then autoionize to the excited state, X^*, before continuing the process as shown:

$$e^- + X \rightarrow (X^-)^* \rightarrow X^* + e^- \rightarrow X^+ + e^- + e^- \tag{1.3}$$

This process is known as Resonant-Excitation Double-Autoionization (REDA). Alternatively, the excited state formed from the dielectronic recombination of the impact electron can doubly auto-ionize

$$e^- + X \rightarrow (X^-)^* \rightarrow X^+ + e^- + e^- \tag{1.4}$$

in a process known as Resonant-Excitation Auto-Double ionization. These two processes are, however, usually very small and are not expected to contribute significantly to the ionization cross sections. The process REDA is included in the R-matrix ionization cross

sections, while Resonant-Excitation Auto-Double ionization is not.

We can find the total ionization cross section by summing the direct ionization process with the indirect processes:

$$\sigma_{total} = \sum_i \sigma_{direct} + \sum_j \sigma_{indirect} \tag{1.5}$$

where the first sum is over the direct ionization channels and the second sum is over the inner subshell electrons which can be excited to an autoionizing state.

Direct ionization is a simple process of exciting a bound electron to the continuum, so as the impact electron energy increases, those cross sections increase until they plateau at some maximum value, and then fall off at higher energies. Conversely, indirect processes correspond to many possible electron impact excitations. Thus, direct ionization provides a smooth background curve in the cross section plot, while the indirect processes lead to peaks at their allowed energies. Figure 1.3 shows an example cross section for the ionization of the ground state of C^+ (which will be discussed in detail in chapter 2). The general increasing trend of the cross section is a product of direct ionization, while the spiky structure of the curve is a result of the indirect processes.

Electron-impact excitation

Electron-impact excitation cross sections also have a direct and indirect contribution. The direct excitation of level j in X^Z to level l is represented by

$$e^- + X^Z(j) \rightarrow X^Z(l) + e^- \tag{1.6}$$

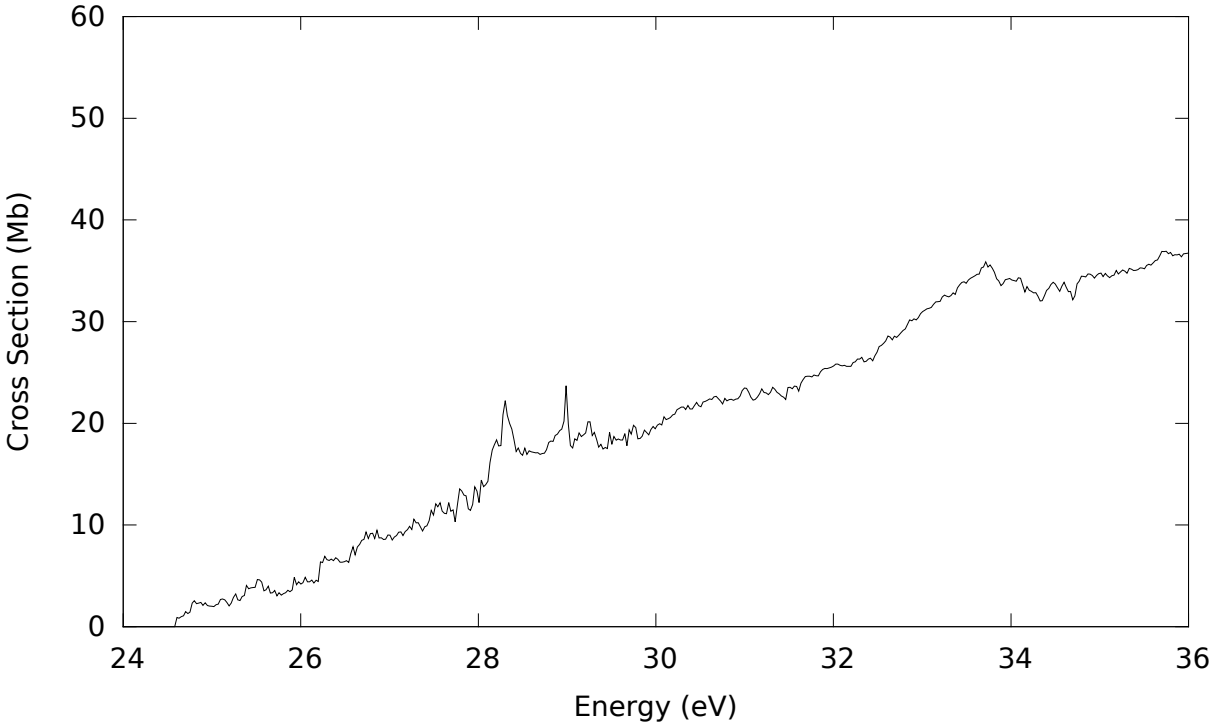

Figure 1.3: Electron-impact ionization from $1s^2 2s^2 2p\ {}^2P^o$

Resonant excitation involves a dielectronic capture (into a doubly excited state), followed by an Auger decay to an excited state of the ion:

$$e^- + X^Z(j) \rightarrow X^{Z-1}(k) \rightarrow X^Z(l) + e^- \tag{1.7}$$

where X^Z is the target ion, X^{Z-1} is the recombined ion of X^Z, and $X^Z(l)$ is an excited state of X^Z.

1.2.2 Collisional Radiative Theory

The basic model for Collisional-Radiative Theory was established by Bates, Kingston, and McWhirter [25]. In this approach, the ionization balance is solved by considering only the connections between the ground state populations of each ion. As a result, the solution to the equilibrium fractional abundances are only a function of electron temperature. Our

aim is to find fractional abundances and emissivities that are also dependent on density. To accomplish this, we employ the Generalized Collisional-Radiative (GCR) model [1], which accounts for long-lived (relative to the scale of the plasma dynamics) metastable states in each ion stage and the role of excited states.

$$\begin{aligned} \frac{dN_\rho}{dt} &= N_e S_{\rho\mu'} N^-_{\mu'} + \left(C_{\rho\sigma} - C_{\rho j} C^{-1}_{ji} C_{i\sigma}\right) N_\sigma + N_e \left(r_{\rho\nu'} - C_{\rho j} C^{-1}_{ji} r_{i\nu'}\right) N^+_{\nu'} \\ \frac{dN^+_\nu}{dt} &= N_e \left(S_{\nu\sigma} - S_{\nu j} C^{-1}_{ji} C_{i\sigma}\right) N_\sigma + \left(C_{\nu\nu'} - N_e^2 S_{\nu j} C^{-1}_{ji} r_{i\nu'}\right) N^+_{\nu'} \end{aligned} \tag{1.8}$$

The variables used are defined in section 1.2.2 along with the derivation of these equations. Note that the fractional abundances are metastable resolved. The excited states have negligible population because we assume that they are in equilibrium with the ground / metastable states (more in section 1.2.2). We need to derive the GCR coefficients to model metastable time dependencies so that we can form an accurate picture.

We also intend to find emissivities, which have both time-dependent (populations) and time-independent (GCR coefficients) parts:

$$\begin{aligned} PEC^{(exc)}_{\sigma, j\to k} &= A_{j\to k} \mathcal{F}^{(exc)}_{j\sigma} \\ PEC^{(rec)}_{\nu', j\to k} &= A_{j\to k} \mathcal{F}^{(rec)}_{j\nu'} \end{aligned} \tag{1.9}$$

Thus, we need to derive the GCR coefficients: F, C, S, r, α, and χ. This will help emphasize the importance of resolving the final states and will prompt the discussion on what atomic data has been omitted.

Time constants and lifetimes

Before we begin our derivation of the GCR coefficients, it is helpful to discuss the lifetimes and relevant time scales, as there is quite a bit of variation in the radiative and collisional processes involving the atoms, ions, and electrons within the plasma. In particular, we are interested in the translational states of free electrons, atoms, and ions and the internal excited and ionized states of atoms and ions. These states determine the relaxation times of various populations, and are thus crucial to spectroscopic models.

We first consider the lifetimes of the relevant atomic parameters: metastable radiative decay, τ_m, ordinary excited state radiative decay, τ_o, and auto-ionizing state decay (radiative and Auger), τ_a. In general, the lifetimes are ordered

$$\tau_m \gg \tau_o \gg \tau_a \tag{1.10}$$

and they have tyipcal values

$$\tau_m \sim \frac{10^1}{z^8} s \qquad \tau_o \sim \frac{10^{-8}}{z^4} s \qquad \tau_a \sim 10^{-13} s \tag{1.11}$$

where z is the ion charge. Note that this order holds until an ion charge of greater than 10.

For comparison, we also consider the time scales of states which depend on plasma conditions, especially particle density. This includes free particle thermalization (including electron-electron τ_{e-e}, ion-ion τ_{i-i}, and ion-electron τ_{i-e}), charge-state change (ionization τ_{ion} and recombination τ_{rec}) and redistribution of population amongst excited ion states, τ_{red}. This group is typically ordered

$$\tau_{ion,rec} \gg \tau_{i-e} \gg \tau_{i-i} \gg \tau_{e-e} \tag{1.12}$$

with the approximate expressions for each time constant given by:

$$\begin{aligned}
\tau_{rec} &\sim [10^{11} - 10^{13}]\frac{1}{(z+1)^2}(\frac{kT_e}{I_H})^2(\frac{cm^{-3}}{N_e})s \\
\tau_{ion} &\sim [10^5 - 10^7](z+1)^4(\frac{I_H}{kT_e})^{1/2}e^{\frac{I_P}{kT_e}}(\frac{cm^{-3}}{N_e})s \\
\tau_{i-i} &\sim [7.0 \times 10^7](\frac{m_i}{m_p})^{1/2}(\frac{kT_e}{I_H})^{3/2}\frac{1}{z^4}(\frac{cm^{-3}}{N_i})s \\
\tau_{i-e} &\sim [1.4 \times 10^9](\frac{m_i}{m_p})^{1/2}((\frac{kT_e}{I_H}) + 5.4 \times 10^{-4}(\frac{kT_i}{I_H})(\frac{m_p}{m_i}))^{3/2}\frac{1}{z^2}(\frac{cm^{-3}}{N_i})s \\
\tau_{e-e} &\sim [1.6 \times 10^6](\frac{kT_e}{I_H})^{3/2}(\frac{cm^{-3}}{N_i})s
\end{aligned} \tag{1.13}$$

Where m_i is the ion mass, m_p is the proton mass, I_P is the ionization potential, N_i is the ion density, N_e is the electron density, T_i is the ion temperature, T_e is the electron tempature, and I_H is the ionization energy of Hydrogen. τ_{red} values can range across those in 1.12.

We also introduce τ_{plasma}, which represents the timescales for plasma ion diffusion across temperature or density scale lengths, relaxation times of transient phenomena, and observation times. For most magnetically confined fusion and astrophysical plasmas, a comparison between 1.10, 1.12, and τ_{plasma} yields

$$\tau_{plasma} \sim \tau_g \sim \tau_m \gg \tau_o \gg \tau_{e-e} \tag{1.14}$$

where τ_g represents the relaxation time of ground state populations of ions (a combination of τ_{rex} and τ_{ion}). The important result here is that the ground and metastable lifetimes are on the same order as the plasma dynamics, while the time scales of the excited states and of the electron-impact excitation and ionization are much quicker. Thus, the ground and metastable populations should be modelled dynamically alongside the rest of the plasma model. However, we can perform the atomic modelling to account for the electron collisions and the role of the excited states in a manner that separates the ground and metastable

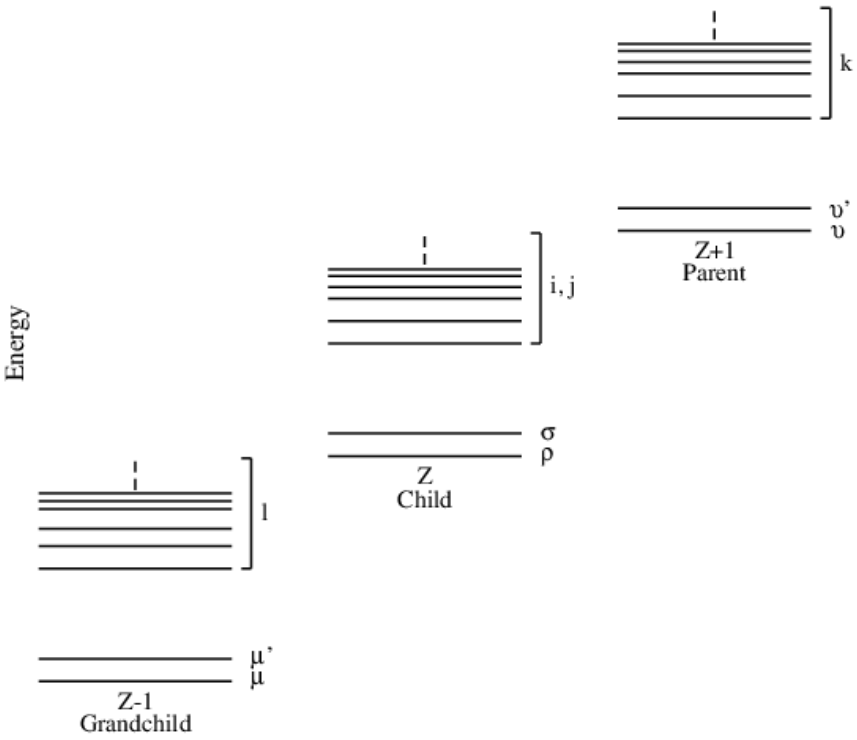

Figure 1.4: Energy level diagram showing three connected ion stages in the GCR picture components from the excited states.

Derivation of GCR Coefficients

We consider a general case of three connected ion stages as shown in Figure 1.2.2:

$Z - 1 =$ grandchild

$Z =$ child

$Z + 1 =$ parent

Because they are all long-lived, both the metastable and ground states have significant populations and there is no real distinction between them. So, for the purposes of this discussion and throughout this dissertation, we will use the term "metastable" to refer to both the ground and metastable states. When necessary for clarification, we will use the terms "ground-metastable" and "excited-metastable" to distinguish between the two. The term "excited state" refers to a state that has a dipole decay path to a state below it. Finally, for consistency in notation, we adopt the following convention for each ion stage's metastable and excited states:

$Z-1$: μ , μ' (metastables), l (excited)
Z : ρ , σ (metastables), i, j (excited)
$Z+1$: ν , ν' (metastables), k (excited)

The excited states have such short lifetimes that we can assume they are in a quasi-equilibrium with the metastable states. Thus we can set dN/dt to zero for the excited states. We will still consider the time dependence of the metastables. Our goal is to extract the connections between the metastable states while accounting for transitions that include the excited states.

There is a set of radiative (coefficient A_{ij}) and collisional (coefficient q_{ij}) couplings between levels, which we will denote as C_{ij} (this is an element of the collisional-radiative matrix representing the transition from j to i), and to which we will add the direction ionization from each level of the ion to the next ion stage (coefficient S_i) and direct recombination to each level of the ion from the next ion stage (coefficient r_i). So for each level, we can write the total loss rate coefficient for the population number density, N_i, as

$$C_{ii} = -\sum_{j \neq i} (q_{ji} + A_{ji}) - N_e S_i = -\sum_{j \neq i} C_{ji} - N_e S_i \tag{1.15}$$

Since the excited state populations are so small compared to that of the metastable states, recombination from the metastables of the adjacent ion stage dominate, so we only need consider the recombination events that begin at a metastable state, $r_{i\nu}$. Similiarly, we need only include the direct ionization from each child level to the parent metastable, such that $S_i = \sum_{\nu} S_{\nu i}$, and the direct ionization from the grandchild metastables to the child metastables, $S_{\rho\mu'}$. Thus the continuity equations for the populations can be written (in matrix form) as:

$$\begin{bmatrix} dN_{\mu}^{-}/dt \\ dN_{\rho}/dt \\ dN_{i}/dt \\ dN_{\nu}^{+}/dt \end{bmatrix} = \begin{bmatrix} C_{\mu\mu'} & N_e R_{\mu\sigma} & 0 & 0 \\ N_e S_{\rho\mu'} & C_{\rho\sigma} & C_{\rho j} & N_e r_{\rho\nu'} \\ 0 & C_{i\sigma} & C_{ij} & N_e r_{i\nu'} \\ 0 & N_e S_{\nu\sigma} & N_e S_{\nu j} & C_{\nu\nu'} \end{bmatrix} \begin{bmatrix} N_{\mu'}^{-} \\ N_{\sigma} \\ N_{j} \\ N_{\nu'}^{+} \end{bmatrix} \tag{1.16}$$

Our focus is on the Z-times ionized stage, so the equations for the (Z-1) and (Z+1) stages have been put into an abbreviated form. The first and last lines represent the rate equations for all of the metastable and excited levels for the (Z-1) and (Z+1) ions, respectively. The second line represents the metastable populations for the Z stage and the third line represents all of the excited states in that stage.

Employing the approximation that $\frac{dN_i}{dt} = 0$, we can solve the third line in the matrix for the excited state population:

$$N_j = -C_{ji}^{-1} C_{i\sigma} N_{\sigma} - N_e C_{ji}^{-1} r_{i\nu'} N_{\nu'}^{+} \tag{1.17}$$

Note that we adopt Einstein's summation convention for repeated indices. Substituting 1.17 into line two of 1.16 yields:

$$\frac{dN_{\rho}}{dt} = N_e S_{\rho\mu'} N_{\mu'}^{-} + \left(C_{\rho\sigma} - C_{\rho j} C_{ji}^{-1} C_{i\sigma} \right) N_{\sigma} + N_e \left(r_{\rho\nu'} - C_{\rho j} C_{ji}^{-1} r_{i\nu'} \right) N_{\nu'}^{+} \tag{1.18}$$

This equation is the total time-dependent population of the Z stage metastable state, ρ. The first term is the direct ionization from the $(Z-1)$ stage metastables to ρ, noting that the excited levels of the $(Z-1)$ ion have a very small population relative to the metastables, so the primary contribution will come from the metastable states. The second term gives us the GCR metastable cross-coupling coefficients (for $\rho \neq \sigma$):

$$Q_{\sigma\to\rho} = \frac{C_{\rho\sigma} - C_{\rho j}C_{ji}^{-1}C_{i\sigma}}{N_e} \tag{1.19}$$

This coefficient gives the connections between ρ and σ, both directly and through all of the excited states i and j. Note that the on-diagonal coefficient with $\rho = \sigma$ is a total loss coefficient from ρ.

The third term in 1.18 is the net recombination from $(Z+1)$ stage metastable, ν' to ρ, including both direct recombination from ν to ρ and recombination to a Z excited state, i, redistribution from i to excited state j, and transition from j to ρ. So we define an effective recombination rate coefficient

$$\alpha_{\nu'\to\rho} = r_{\rho\nu'} - C_{\rho j}C_{ji}^{-1}r_{i\nu'} \tag{1.20}$$

If we substitute 1.17 into 1.16 line four, we get an equation for the total time-dependent $(Z+1)$ stage metastable state, ν:

$$\frac{dN_\nu^+}{dt} = N_e\left(S_{\nu\sigma} - S_{\nu j}C_{ji}^{-1}C_{i\sigma}\right)N_\sigma + \left(C_{\nu\nu'} - N_e^2 S_{\nu j}C_{ji}^{-1}r_{i\nu'}\right)N_{\nu'}^+ \tag{1.21}$$

From the first term, we can define an effective ionization rate coefficient

$$S_{\sigma\to\nu} = S_{\nu\sigma} - S_{\nu j}C_{ji}^{-1}C_{i\sigma} \tag{1.22}$$

which represents the direction ionization from σ to ν and the collisional excitation from σ to i, redistribution from i to j, and collisional ionization from j to ν.

We can define the second term in 1.21 as the parent cross-coupling coefficient

$$\chi_{\nu' \to \nu} = -N_e S_{\nu j} C^{-1}_{ji} r_{i\nu'} \tag{1.23}$$

which represents recombination from ν' to i, redistribution from i to j, then ionization from j to ν.

We have now derived a set of rate coefficients that are both density and temperature dependent, where the density dependence can be found in the role of the excited states. Thus, we can now solve for the fractional abundances of the metastable (including ground) states as functions of both density and temperature.

Finally, we can discuss the emissivity related to a specific spetral line, which is defined by

$$\epsilon_{j \to k} \equiv A_{j \to k} N_e N_j \tag{1.24}$$

where, again, we substitute 1.17, which yields:

$$\begin{aligned} \epsilon_{j \to k} &= A_{j \to k} N_e (-C^{-1}_{ij} C_{i\sigma} N_\sigma - C^{-1}_{ji} N_e^2 r_{i\nu'} N^+_{\nu'}) \\ &= A_{j \to k} (\mathcal{F}^{(exc)}_{j\sigma} N_e N_\sigma + \mathcal{F}^{(rec)}_{j\nu'} N_e N^+_{\nu'}) \end{aligned} \tag{1.25}$$

The two terms in this equation allow us to separate the excitation photon emissivity and the recombination photon emissivity coefficients:

$$PEC^{(exc)}_{\sigma,j\to k} = A_{j\to k}\mathcal{F}^{(exc)}_{j\sigma}$$
$$PEC^{(rec)}_{\nu',j\to k} = A_{j\to k}\mathcal{F}^{(rec)}_{j\nu'} \tag{1.26}$$

Approximations within the GCR model

From our discussion leading to the relationship between timescales in equation 1.14, we note that the excited states have very short lifetimes relative to the metastables, so we consider them to be in quasi-equilibrium with the metastables. Thus, we set $\frac{dN_i}{dt}$ to zero. This approximation holds until an ion charge of $z \sim 50+$, when the metastable lifetimes start approaching those of the autoionizing states.

In our GCR discussion, we neglected the recombination from the excited states of the parent, $(z+1)$, ion to the child, z, ion. We can set r_{ik}, $r_{\rho k}$, and $r_{\sigma k}$ to zero because the excited population, N_k, is very small. Since these excited states are primarily populated through electron collisions, this approximation is density dependent and varies for different ions and charge states. However, the densities where N_k becomes significant are far beyond those typically found in laboratory plasmas or low-temperature astrophysical plasmas.

We also neglect the ionization from the child ion to the parent excited states. In general, $S_{\nu i} \gg S_{ki}$, so in most cases we can safely neglect this term. However, there are some cases where this is not the case, as is seen in the later discussion of the ionizing states of Nitrogen in chapter 6 and in Lithium [4].

1.2.3 Atomic Structure for Collisional Excitation

1.2.4 R-matrix theory

R-Matrix theory was introduced by Wigner and Eisenbud in 1946 and 1947 [26, 27] for applications in nuclear resonance reactions. It was later realized that the same method could be applied to the resonance processes in electron-atom/ion collisions and the process was formalized by Burke etal [28]. A comprehensive overview of the R-Matrix theory can be found in the text by Burke and Berrington [29].

The fundamental concept of the R-Matrix theory is the partitioning of the configuration space into two regions: inner and outer. For electron-ion collisions, this partition occurs at a boundary defined by the size of the ion's most diffuse bound orbital. For the inner region, electron exchange and correlation effects between the impact and target electrons are important and must be accounted for. For the outer region, the correlation effects are minor, so it is sufficient to solve the simpler case of a perturbed electron moving in a shielded nuclear potential, where the scattered electron moves in the long-range multipole potential of the target. To ensure continuity of the wavefunction, we set the solutions to the inner and outer region equal to each other at the boundary of the inner and outer regions, referred to as the "R-Matrix box". The energy eigenvalues for this continuity condition form the elements of the R-matrix.

We begin by partitioning configuration space at a radius of $r = a_0$, where r is the radial distance of the scattering electron from the nucleus, and a_0 is chosen such that the charge distribution of the target ion is contained within the sphere. This choice for a_0 is by definition the same as selecting a radius equal to the size of the target ion's most diffuse bound orbital. Critically, the $(N + 1)$-electron system behaves in a way similar to

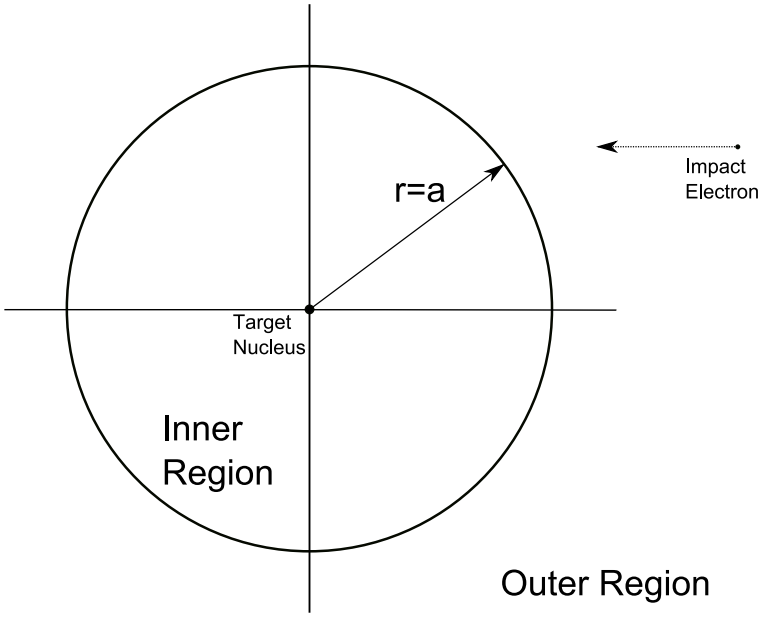

Figure 1.5: Partitioning of configuration space

a bound state and these states are described by a configuration interaction (CI) basis expansion of the total wavefunctions, analogous to that used in many bound state calculations.

For scattering of an electron by a light atom of N electrons, the time-independent Schrödinger equation describing the interaction is

$$H_{N+1}\Psi = E\Psi \tag{1.27}$$

where E is the total energy and the non-relativistic Hamiltonian is defined by

$$H_{N+1} = \sum_{i=1}^{N+1}(-\frac{1}{2}\nabla_i^2 - \frac{Z}{r_i}) + \sum_{i>j=1}^{N+1}\frac{1}{r_{ij}} \tag{1.28}$$

where Z is the nuclear charge and $r_{ij} = |r_i - r_j|$, r_i and r_j are the vector coordinates of electrons i and j relative to an origin placed at the target nucleus, which is assumed to have infinite mass.

To solve equation 1.27, we first create the eigenstates Φ_i of the target using

$$\langle \Phi_i | H_N | \Phi_j \rangle = \omega_i \delta_{ij} \tag{1.29}$$

where ω_i is the eigenenergy of state i and H_N is the Hamiltonian of the target, which has the same form as equation 1.28 using N instead of $N+1$. These eigenstates are written as a CI expansion in terms of some basis configurations ϕ_i by

$$\Phi_i(x_1 ... x_N) = \sum_j \phi_j(x_1 ... x_N) c_{ji} \tag{1.30}$$

where $x_i \equiv r_i \sigma_i$ represents the space and spin coordinates of the ith electron and the coefficients c_{ji} are determined by diagonalizing the target Hamiltonian. For our work involving carbon, argon, and nitrogen ions, we use the atomic structure package AUTOSTRUCTURE [30] to generate the spectroscopic radial orbitals for use in our scattering calculation.

The basis states that provide the solution to 1.27 applied to the inner region have the form:

$$\psi_k^{N+1} = A \sum_{i,j} a_{ijk} \psi_i^{N+1} \frac{u_{ij}(r_{N+1})}{r_{N+1}} + \sum_i b_{ik} \chi_i^{N+1} \tag{1.31}$$

where A is an antisymmetrization operator, ψ_i^{N+1} are channel functions obtained by coupling N-electron target states with the angular and spin functions of the scattered electron, $u_{ij}(r)$ are radial continuum basis functions. The square integrable (or quadratically integrable) functions χ_i^{N+1} are bound functions included to account for electron correlation effects, to ensure completeness of the total wavefunction, and - given that they are constructed solely from target orbitals - they will have negligible value on the R-matrix boundary. As they are the solution to the radial part of the Hamiltonian, the continuum basis orbitals $u_{ij}(r)$ are only defined over the range $0 \leq r \leq a_0$. These orbitals represent the radial motion of the scattered electron in the internal region, thus they must vanish at the origin and are

typically chosen such that they are non-zero at the R-matrix boundary, $r = a_0$, to provide a link between the solutions to the internal and external regions. Finally, the coefficients a_{ijk} and b_{ik} are determined by diagonalization of the $(N+1)$-electron Hamiltonian.

The resulting eigenfunctions and eigenvectors are used to form the R-matrix:

$$R_{ij}(E) = \frac{1}{2a} \sum_k \frac{\omega_{ik}\omega_{jk}}{E_k - E} \tag{1.32}$$

where E_k are the eigenvalues of the $(N+1)$-Hamiltonian and $\omega_i k$ are surface amplitudes given by

$$\omega_{ik} = \sum_j u_{if} c_{ijk}|_{r=a_0} \tag{1.33}$$

where the c_{ijk} correspond to the eigenvectors of the Hamiltonian.

The R-matrix relates the reduced radial wavefunction $F_i(r)$, which describes the radial motion of the scattered electron in the ith channel, to its derivative on the R-matrix boundary $(r = a_0)$. The reduced radial wavefunctions satisfy

$$F_i(r = a_0) = \sum_j R_{ij}(E)(a\frac{dF_j}{dr} - bF_j)_{r=a_0} \tag{1.34}$$

In the external region, the total wavefunction is expanded similar to equation 1.31 without the antisymmetrization because the scattered and target electrons no longer occupy the same region of the configuration space. The external wavefunction is of the form

$$\Psi^{N+1} = \sum_i \psi_i^{N+1} \frac{F_i(r_{N+1})}{r_{N+1}} \tag{1.35}$$

where the channel functions ψ_i are the same as those used in the inner region. Applying this to equation 1.27 yields:

$$(\frac{d^2}{dr^2} - \frac{l_i(l_i+1)}{r^2} + \frac{2Z}{r} + k_i^2)F_i(r) = 2\sum_{j=1}^{n} V_{ij}(r)F_j(r) \tag{1.36}$$

where both i and j sum over the n coupled channels of the close-coupled expression, l_i are the channel angular momenta, and k_i^2 are the channel energies, defined terms of the eigenenergies E_i by

$$k_i^2 = 2(E - E_i) \tag{1.37}$$

The potential matrix V_{ij} is defined by

$$V_{ij} = \langle \psi_i^{N+1} | \sum_{k}^{N} \frac{1}{r_{kN}} | \psi_j^{N+1} \rangle \tag{1.38}$$

where the integration is carried out over all coordinates except those of the impact electron. To solve for the elements V_{ij} of the potential matrix, we use the expansion

$$\sum_{k}^{N} \frac{1}{r_{kN}} = \sum_{\lambda=0}^{\infty} \sum_{k=1}^{N} r_k^{\lambda} P_{\lambda}(cos\theta_{kN+1}) \tag{1.39}$$

where in practice, we keep only the dipole and quadrapole Legendre Polynomial terms. The elements V_{ij} can be expressed in terms of a finite inverse power series in the radial coordinate,

$$V_{ij}(r) = \sum_{\lambda=0}^{\lambda_m} \frac{C_{ij}^{(\lambda)}}{r^{\lambda+1}} \tag{1.40}$$

where $C_i j^{(\lambda)}$ are the long-range potential coefficients. From the form of this expansion, it is apparent that the primary contribution for V_{ij} comes from the region $r < a_0$, which allows us to construct the element V_{ij} from the target N-electron dipole matrix elements. The $n \times n$ R-matrix can thus be related to the asymptotic form $n \times n$ K or S matrices. The final cross section in the LSπ coupling scheme for the transition from state $\alpha_i L_i S_i$ to state $\alpha_j L_j S_j$ is given by

$$\sigma_{i\to j} = \frac{\pi}{k_i^2}\sum_{l_i,l_j}\frac{(2L+1)(2S+1)}{(2L_i+1)(2S_i+1)}\delta_{ij} - \delta_{ij}^2 \tag{1.41}$$

1.2.5 R-matric with PseudoState Calculations

As mentioned in the previous section, the standard R-matrix method treats the scattering (N+1)-electron system as a bound state. For our work involving the ionization of singly-ionized carbon, we need a method of representing the high Rydberg states and of coupling to continuum states. To accomplish this, we use a finite number of pseudostates as introduced by Griffin et al [31]. In this scheme, we represent the target with the spectroscopic states outlined above and by using non-orthogonal Laguerre pseudo-orbitals to represent both the higher Rydberg states and the continuum. These pseudo-orbitals are subsequently orthogonalized to each other and to the spectroscopic states. These pseudo-orbitals do not have spectroscopic eigenvalues and only agree with their spectroscopic counterparts in having the same number of radial nodes. The eigenenergies of the pseudostates range from just below the ionization limit to far above and can thus be used to discretize the continuum. It should be noted that the pseudostate complex only serves as a computational representation of the continuum, but individual pseudostates have no physical significance.

1.2.6 Relativistic R-matrix theory

In the work involving electron collisions with carbon and nitrogen ions, we account for relativistic effects by solving equation 1.27 using the Breit-Pauli (BP) Hamiltonian:

$$H_{(N+1)}^{BP} = H_{(N+1)}^{NR} + H_{(N+1)}^{rel} \tag{1.42}$$

Where $H_{(N+1)}^{NR}$ is the non-relativistic Hamiltonian

$$H^{NR}_{(N+1)} = \sum_{i=1}^{N+1}(-\frac{1}{2}\nabla_i^2 - \frac{Z}{r_i}) + \sum_{i>j=1}^{N+1}\frac{1}{R_{ij}} \tag{1.43}$$

and $H^{rel}_{(N+1)}$ are relativistic correction terms, including the one-body mass correction term, the Darwin term, and the spin-orbit term. In this representation, the conserved quantum numbers are now JM_J and π rather than LSM_LM_S and π.

In the work involving electron collisions with Argon, we use both the solutions for the Breit-Pauli Hamiltonian and the full Dirac equation.

$$H^{D}_{N+1} = \sum_{i=1}^{N+1}(c\alpha_i \cdot p_i + \beta' c^2 - \frac{Z}{r_i}) + \sum_{i>j=1}^{N+1}\frac{1}{r_{ij}} \tag{1.44}$$

where α_i and β' are the usual Dirac matrices. We used the relativistic atomic structure package GRASP [32] to generate the spectroscopic radial orbitals for use in our scattering calculations.

1.2.7 Rate Coefficient Calculation

Rate coefficients / effective collision strengths are generated from our R-Matrix collision strength data via convolution with a Maxwellian electron distribution:

$$\Upsilon_{ij} = \int_0^\infty \Omega_{ij} \exp\frac{-E_j}{kT} d(\frac{E_j}{kT}) \tag{1.45}$$

where E_j is the energy of the outgoing electron, Γ_{ij} is the collision strength between states i and j.

1.3 Outline of dissertation work

The aim of this dissertation is to generate the fundamental atomic data required to construct a GCR dataset for carbon. This will require both the assembly of existing data, and the calculation of new RMPS data for C^+, both for excitation and ionization. The ionization of C^+ will present some challenges that have not been previously addressed when using RMPS data for GCR data, namely the issue of final state resolution for excited states of open p-shell systems. This issue is more complex for neutral N and we will use that case to explore the future direction required for such calculations going beyond simple systems. We also present fine-structure electron-impact excitation calculations for Ar^{2+}, for application in ultra-low temperature environments. Thus, the common thread to this work is the calculation of non-perturbative data for plasma modeling.

Chapter 2

Electron-impact ionization of C^+

In this section, we will focus on electron-impact ionization of C^+. New RMPS cross section calculations will be presented and compared with the literature values. An important new aspect of this work will be to resolve the final states in the ionization processes, the first time this has been achieved for an RMPS calculation.

2.1 Introduction

Previous ionization calculations made by Ludlow et al. [33] include ionization from the ground term and those made by Ballance et al. [34] include ionization from the (^2S) terms of the $1s^2 2s^2 3l$ excited configurations. We expand these results to include ionization from the ground and all excited terms through the $1s^2 2s^2 4l$ excited configurations, including the important metastable term $1s^2 2s 2p^2$ (^{4}P). Additionally, Ludlow et al. [33] reported on single ionization cross section measurements using the cross-beam apparatus at the Oak Ridge National Laboratory facility. We will use the previous calculations and measurements as a benchmark for our extended calculations.

We performed our ionization calculations using two models, denoted A and B, both of which are carried out in LS coupling. We employ the standard RMPS approach of the R-Matrix II codes, utilizing Laguerre pseudo-orbitals to represent high Rydberg and continuum states. The difference between our two calculations is that Model B expands the included pseudo-state orbitals to higher orbital angular momentum, testing the convergence with higher angular momentum over that of Model A. Comparison between these models

allows us to speculate on the lower bound of the uncertainty for our cross section calculations.

2.2 Atomic structure

For our Model A, we included spectroscopic orbitals 1s $\leq$ nl $\leq$ 5p and pseudo-orbitals 5d $\leq$ nl $\leq$ 12g. We used the configurations $1s^2 2s^2$nl (3s $\leq$ nl $\leq$ 12g), $1s^2 2s2p$nl (2p $\leq$ nl $\leq$ 12g), $1s^2 2p^2$nl (2p $\leq$ nl $\leq$ 12g), $1s^2 2s3s^2$, $1s^2 2s3d^2$. These configurations generate a maximum number of 890 terms for use in the close-coupling expansion.

In this implementation of the RMPS method, we employ 33 continuum basis orbitals, which yields an R-Matrix box size of 50 a.u. Partial-wave calculations were made ranging from L=0–43 for this LS-resolved calculation. The contributions from higher partial waves were estimated for dipole transitions using the method originally described by Burgess [35] and for nondipole transitions assuming a geometric series in L, using energy ratios, with special procedures for addressing transitions between near-degenerate LS terms.

For our Model B, we included the same spectroscopic orbitals and the same configurations as in our Model A. The pseudo-orbitals were increased slightly to 5d $\leq$ nl $\leq$ 12h, which resulted in a total of 1044 terms. We chose 36 continuum basis orbitals. The size of the R-matrix box remained unchanged at 50 a.u. Partial-wave calculations were performed using a range of L=0–43. Higher partial wave contributions were calculated using the same method as in the calculation of Model A.

The total ionization cross sections are determined from the summation of excited-state transitions to energetically accessible LS terms in the continuum, which include several non-pseudostate and several pseudostate configurations (i.e. some are excitation and some are direct ionizations). We assume that the sum of these cross sections is the total ionization.

This contains an inherent approximation since we do not allow for radiative decay of the doubly excited states into a bound state below the ionization potential; however, as discussed in Section 1.2.2, the auto-ionization decay rate is several orders of magnitude larger than the radiative decay rate, so this approximation should be valid. Additionally, these excitation-autoionization transitions ensure that the total ionization cross section will always exhibit a degree of structure superimposed on the direct ionization cross section. This large RMPS calculation was made feasible due to the development of a new parallelization scheme of the inner region of the calculation. The diagonalization of the large (N+1)-Hamiltonian was modified so that each symmetry could be diagonalized simultaneously. Previous versions of the code diagonalized each partial wave sequentially. Our capacity to reduce the inner region calculation to the time required for the formation and diagonalization of a single partial wave, though carried out concurrently with every other partial wave, has made the ionization from excited LS terms involving excitation-autoionization possible. The RMPS method also provides a comprehensive dataset (required by collisional-radiative modeling) of every excited-state ionization in a single calculation.

For spectroscopic accuracy in diagnostics, we shifted the term and level energies from the calculated values in AUTOSTRUCTURE to those found in the NIST database. This was done for terms/levels with energies from the ground term/level to the ionization limit. Table 2.1 is a representative sample of the shifts for the first eighteen terms.

2.3 Comparison between Models A and B

To check the convergence with angular momentum in the pseudostate expansion, we first compare our models A and B. Figures 2.1 and 2.2 show the cross sections for ionization from the C^+ ground state and the $1s2s2p^2$ excited state and demonstrate the effect of including the l=5 pseudostates in our Model B. In both graphs, the red curve is our Model

Configuration	Term	Energy	NIST Energy	Absolute Difference
$1s^2 2s^2 2p$	$^2P^o$	0.000000	0.000000	0.000000
$1s^2 2s 2p^2$	^4P	0.385542	0.391786	0.006244
$1s^2 2s 2p^2$	^2D	0.695680	0.682437	0.013243
$1s^2 2s 2p^2$	^2S	0.937749	0.878930	0.058819
$1s^2 2s 2p^2$	^2P	1.037454	1.007948	0.029506
$1s^2 2s^2 3s$	^2S	1.063694	1.061584	0.002110
$1s^2 2s^2 3p$	$^2P^o$	1.181608	1.200043	0.018435
$1s^2 2s^2 3d$	^2D	1.302221	1.325965	0.023744
$1s^2 2p^3$	$^4S^o$	1.324491	1.293861	0.030630
$1s^2 2p^3$	$^2D^o$	1.395941	1.370740	0.025201
$1s^2 2s^2 4s$	^2S	1.410050	1.432437	0.022387
$1s^2 2s^2 4p$	$^2P^o$	1.458922	1.480627	0.021705
$1s^2 2s^2 4d$	^2D	1.505126	1.531675	0.026549
$1s^2 2s^2 4f$	$^2F^o$	1.511477	1.539459	0.027982
$1s^2 2s 2p 3s$	$^4P^o$	1.519942	1.521515	0.001573
$1s^2 2s^2 5s$	^2S	1.553881	1.579276	0.025395
$1s^2 2s 2p 3s$	$^2P^o$	1.555923	1.619731	0.063808
$1s^2 2s^2 5p$	$^2P^o$	1.583310	1.596996	0.013686

Table 2.1: C^+ Model A Term Shifts

A, the black curve is our Model B, and the blue curve is the previously discussed Ludlow calculation. For ionization from ground, inclusion of the l=5 pseudostate increased our cross sections by 3–5Mb or up to around 20% at the peak of the cross section. The effect on the ionization of the $1s2s2p^2$ excited state was much larger, around a 20 Mb increase at all energies, which is again about 20% at the peak.

Since very few of the C^+ spectroscopic states have a total angular momentum of L=5 or greater, we expect that the inclusion of pseudo-orbitals with $l = 6$ or greater would have even less of an effect on the cross section values than inclusion of the $l = 5$ orbitals. Thus, we can conclude that our calculations have converged and can now compare to existing cross section calculations.

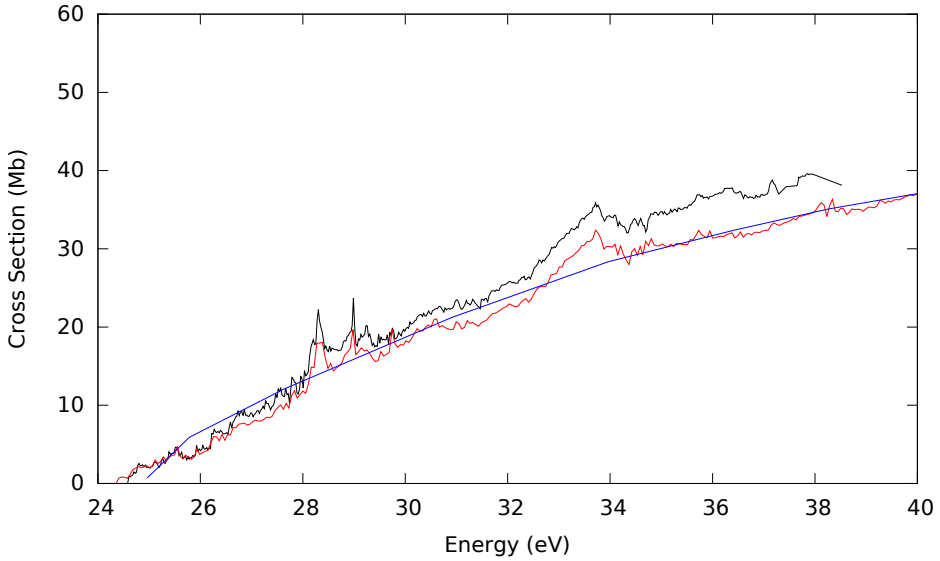

Figure 2.1: Electron-impact ionization from $1s^2 2s^2 2p$ ($^2P^o$). Solid red curve, present Model A; solid black curve, present Model B; solid blue curve, Ludlow R-Matrix.

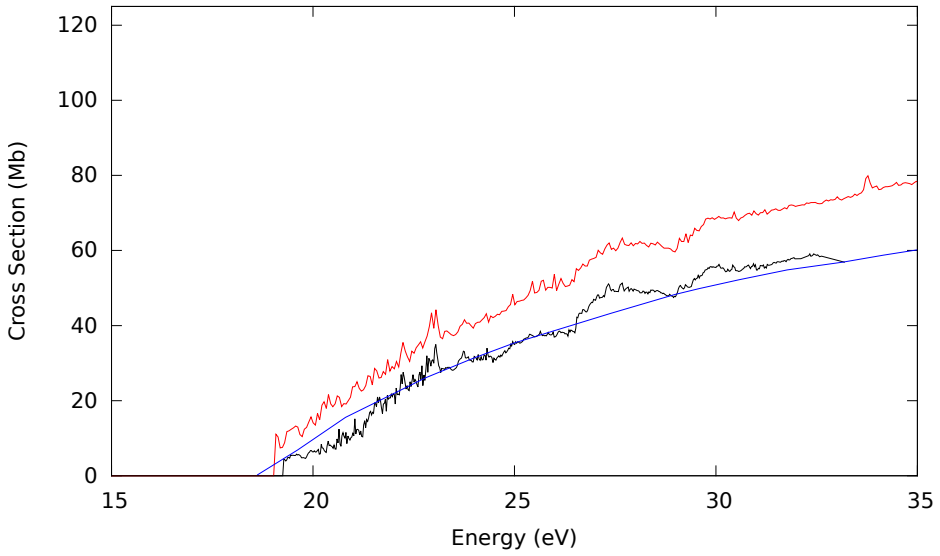

Figure 2.2: Electron-impact ionization from $1s^2 2s 2p^2$ (^4P). Solid red curve, present Model A; solid black curve, present Model B; solid blue curve, Ludlow R-Matrix.

2.4 Comparison with existing data

As a benchmark for our calculations, we compare with existing data. The data used for comparison in this section was obtained by extracting the data from the graphs in the relevant published work. There is an inherent error in this technique for data acquisition, but as this data is only being used for comparison, those minor errors are not significant. Where possible, the resonance structure was preserved, but in cases where that was not possible, we plot only a representative sample of the data. In general, we have good agreement with previous calculations and experimental results.

Electron-impact ionization cross-sections for the ground $1s^2 2s^2 2p$ ($^2P^o$) term are presented in Fig. 2.3. The solid black curve is Model B of our calculation, the solid blue curve is the R-Matrix calculation by Ludlow et al. [33], the filled circles are Ludlow's experimental crossed-beam results, and the filled squares are the results of the Yamada crossed-beam experiment [36]. Our model B is typically about 10% higher than the Ludlow calculation and around 30% higher than the results of both experiments. The Ludlow calculation shows the smooth structure expected from the direct ionization processes (see Section 1.2.1), whereas our calculation includes extra indirect processes, which explains the higher cross-section values.

Considering next the ionization from the $1s^2 2s^2 3l$ configurations, electron-impact ionization cross-sections for $1s^2 2s^2 3s$ (^2S) are presented in Fig. 2.4. The solid black curve is our Model B and the solid blue curve is the R-Matrix calculation of Ballance et al. [34]. Our calculation is about 10-20% lower than the Ballance calculation. Electron-impact ionization cross-sections for $1s^2 2s^2 3p$ ($^2P^o$) are presented in Fig. 2.5. These cross sections agree within about 5-10%. Electron-impact ionization cross-sections for $1s^2 2s^2 3d$ (^2D) are presented in Fig. 2.6. These cross sections agree within 5-15%.

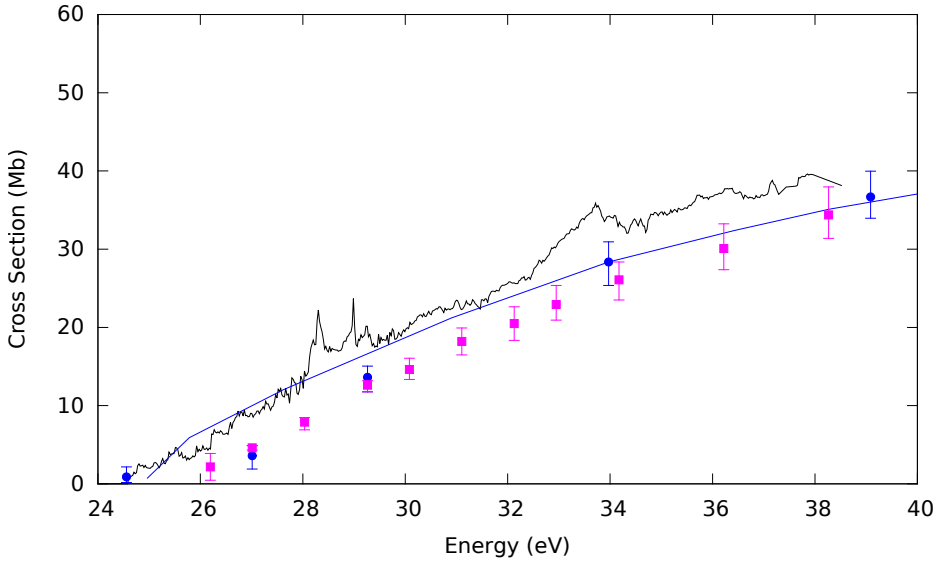

Figure 2.3: Electron-impact ionization from $1s^2 2s^2 2p\ (^2P^o)$. Solid black curve, present Model B; solid blue curve, Ludlow R-Matrix; filled circles, Ludlow experiment; filled squares, Yamada experiment.

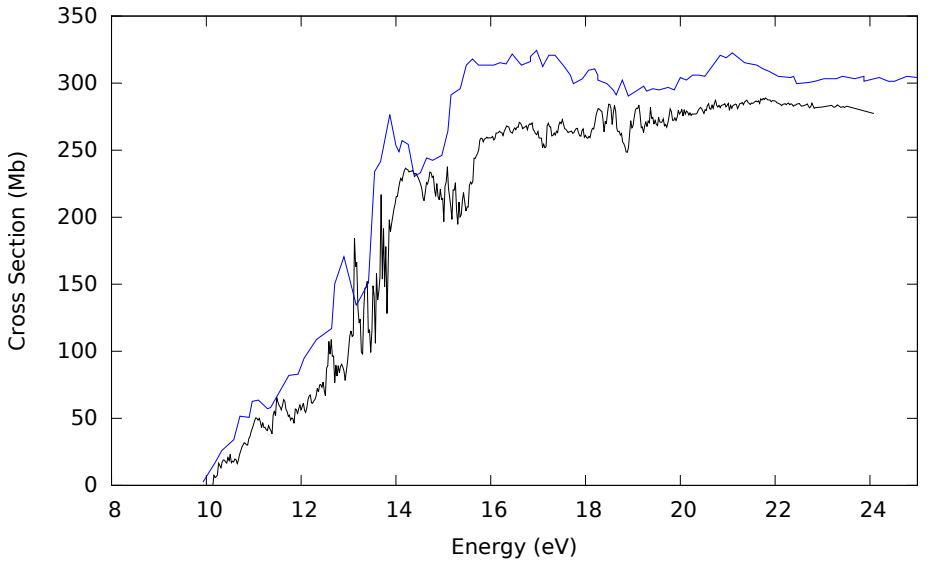

Figure 2.4: Electron-impact ionization from $1s^2 2s^2 3s\ (^2S)$. Solid black curve, present Model B; solid blue curve, Ballance R-Matrix.

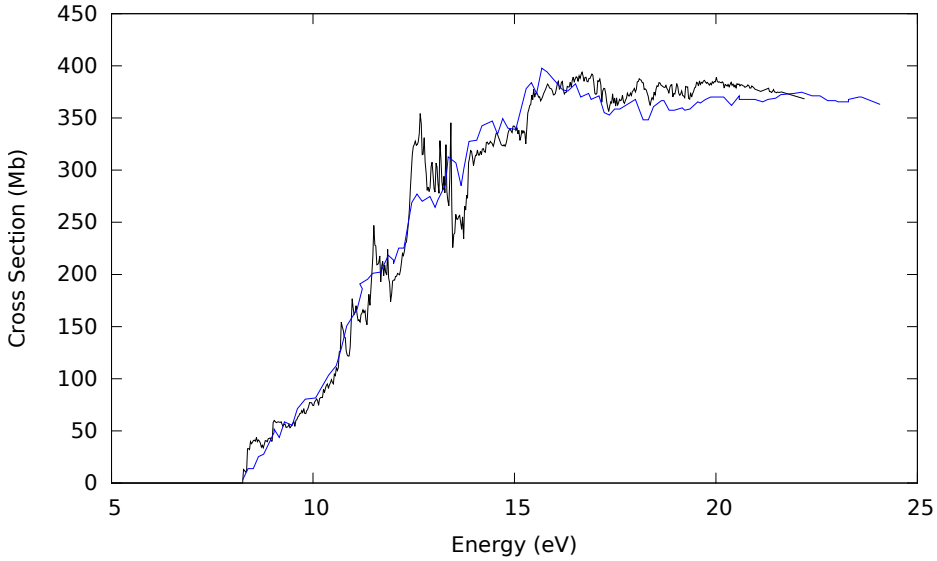

Figure 2.5: Electron-impact ionization from $1s^2 2s^2 3p$ ($^2P^o$). Solid black curve, present Model B; solid blue curve, Ballance R-Matrix.

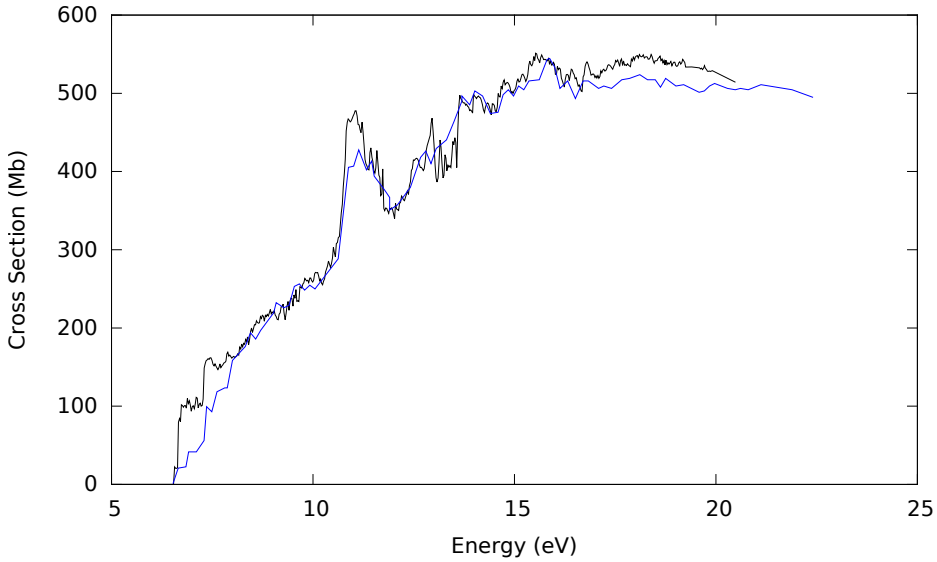

Figure 2.6: Ionization from $1s^2 2s^2 3d$ (^2D). Solid black line, present Model B; solid blue line, Ballance.

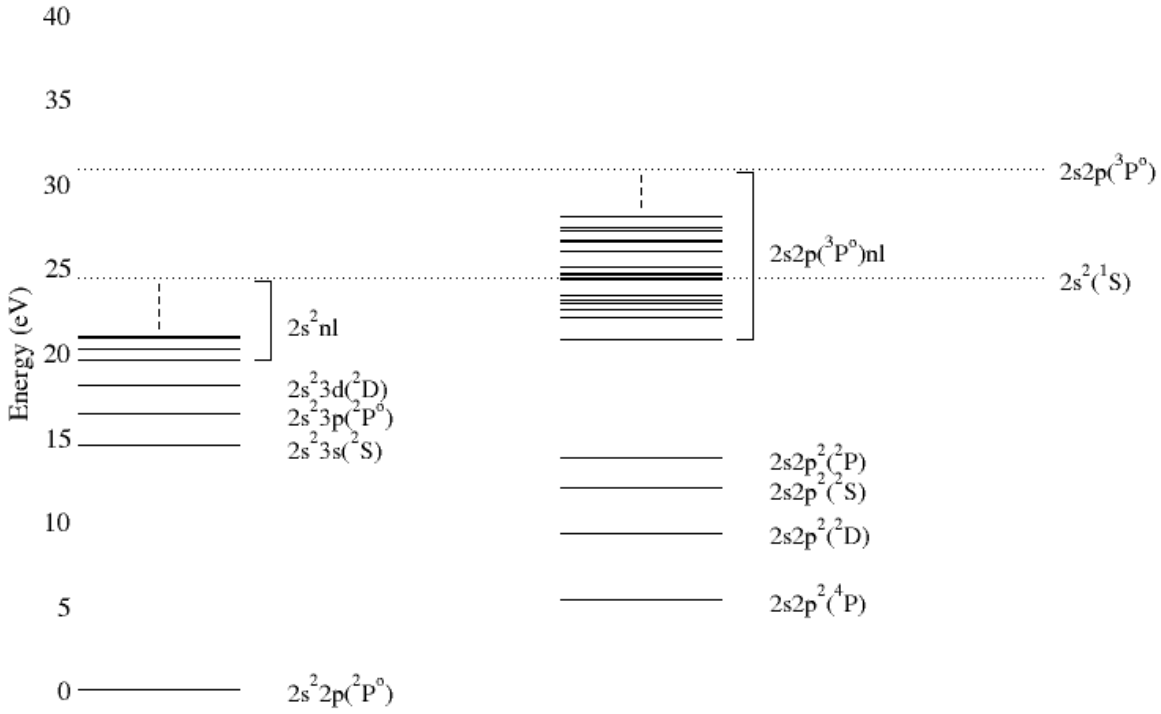

Figure 2.7: Energy level diagram for C^{+}, showing the energies of the C^{2+} final states.

2.5 Ionization to C^{2+} ground- and excited-metastable states

Figure 2.7 is an energy level diagram showing the energies of C^{+} with the $1s^2 2s^2 (^1S)$ ground-metastable and $1s^2 2s 2p (^3P^o)$ excited-metastable states of C^{2+} denoted by the horizontal hashed lines. The features of note for this discussion are the $1s^2 2s^2 nl$ and $1s^2 2s 2pnl$ Rydberg series. For the former, ionization of the nl valence electron yields the expected direct ionization which has to go to the ground term of C^{2+}. The latter Rydberg series, however, may directly ionize to the $2s2p$ excited-metastable state, which cannot dipole decay to the ground-metastable.

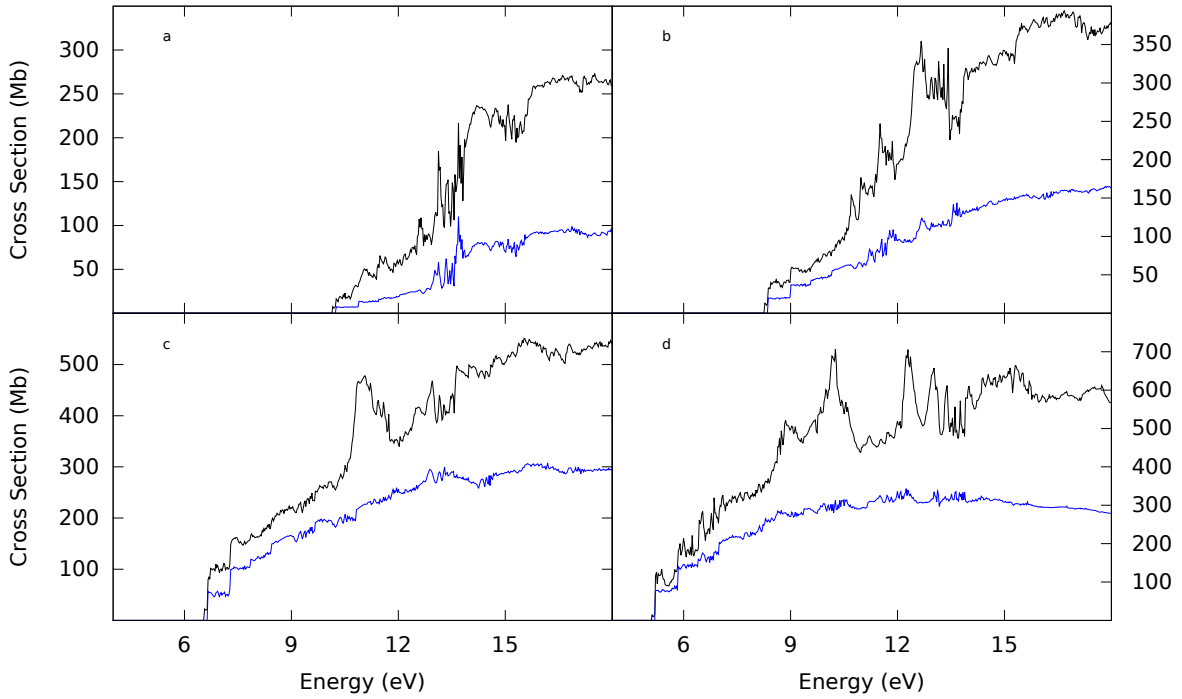

Figure 2.8: Comparison between total cross section (black) and contribution from $2s^2nl$ terms (blue): a) $1s^22s^23s(^2S)$, b) $1s^22s^23p(^2P^o)$, c) $1s^22s^23d(^2D)$, d) $1s^22s^24s(^2S)$.

We will begin by investigating the $1s^22s^2nl$ series. As discussed in Section 2.2, we determine our total ionization cross sections by summing over all excited-state transitions above the C^{2+} threshold. However, since the continuum is represented by discrete states (including both spectroscopic states and pseudostates), we can select a subset of the total to highlight the contribution from only those states that can auto-ionize to the ground-metastable of C^{2+}. Thus, we limit our summation to those terms in the $1s^22s^2nl$ Rydberg series whose energies lie above the 24.4 eV ionization potential. This should correspond to the direct ionization to the ground term of C^{2+}.

Figure 2.8 shows a comparison between the total cross sections and the limited summation over the $2s^2nl$ terms for the first four terms that can directly ionize to the ground-metastable of C^{2+}. These plots indicate clearly that the contribution of the direct ionization

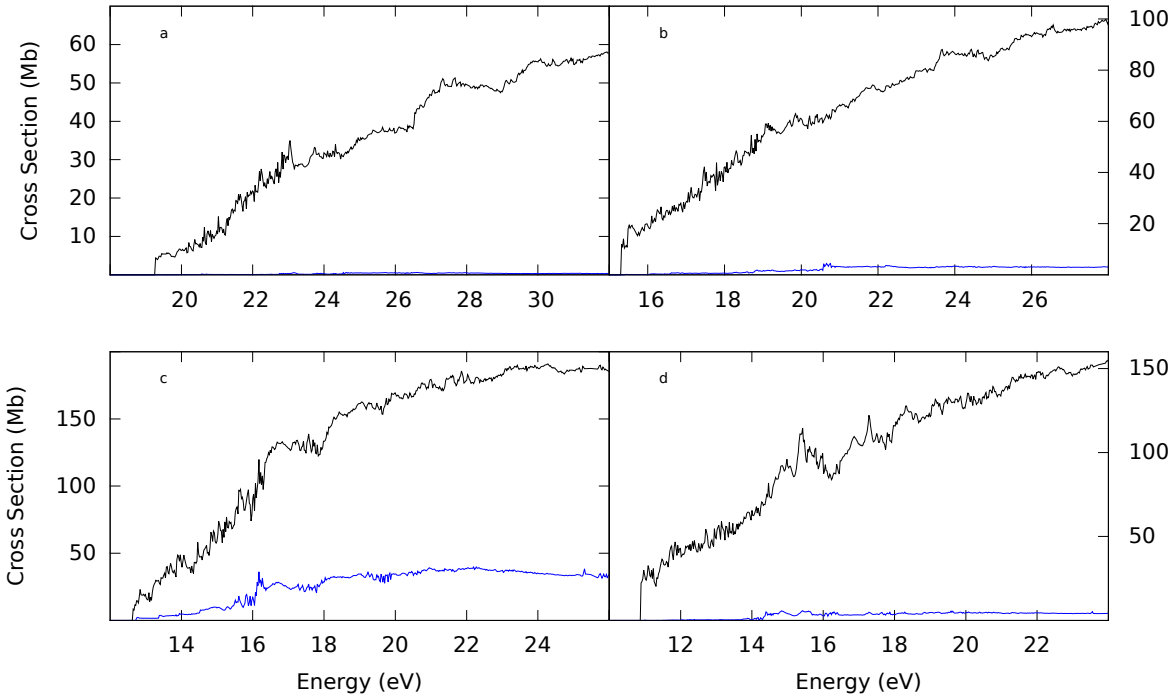

Figure 2.9: Comparison between total cross section (black) and contribution from $2s^2nl$ terms (blue) for the four $1s^22s2p^2$ terms: a) (^4P), b) (^2D), c) (^2S), d) (^2P).

to the ground of C^{2+} is significant, typically 50-80% of the total. The remaining contribution is excitation-autoionization/Auger which will also lead to a C^{2+} ground term final state (see Figure 2.11).

Figure 2.9 shows another comparison between total cross section and the same limited summation over the $2s^2nl$ terms. This figure shows the four terms of the $1s^22s2p^2$ configuration and presents quite a different picture to the $2s^22pnl$ series. Since ionization of the valence $2p$ electron would leave the system in the $1s^22s2p$ excited state of C^{2+}, we would expect the contribution from the $1s^22s^2nl$ terms to be negligible. This is indeed the case for the ^4P term (plot a) and nearly the case for the ^2D and ^2P terms (plots b and d). The ^2S term (plot c), however, exhibits a clear contribution to the ground final terms, which this

making up $20-25\%$ of the total.

This apparent discrepancy arises from the two terms of the $1s^2 2s2p$ configurations: $(^3P^o)$ and $(^1P^o)$. The $(^3P^o)$ term is metastable, but the $(^1P^o)$ term is not. Since the (^4P) term in Figure 2.9 can only ionize to the $(^3P^o)$ term of C^{2+}, the contribution to the cross section from the ground-metastable terms should be near zero. The (^2D) and (^2P) terms (plots b and d) can ionize to either the $(^3P^o)$ or $(^1P^o)$ terms, though the fraction that ionizes to the $(^1P^o)$ term is expected to be small. Thus, the contribution from the ground-metastable terms should be small, though expected to be higher than the (^4P) term. Likewise, the (^2S) term (plot c) can ionize to either (C^{2+}) term, but the fraction that ionizes to the $(^1P^o)$ term is expected to be large. Thus the contribution from the ground-metastable terms is likewise significant.

Figure 2.10 shows the total cross section (in black) compared to the contributions solely from the ground-metastable terms $2s^2nl$ (blue), and from the excited-metastable terms $2s2pnl$ (red) for the $1s^2 2s2p^2(^4P)$ and $1s^2 2s2p(^3P^o)3s(^4P^o)$ terms. These terms were chosen because they are both built on the $1s^2 2s2p(^3P^o)$ core and thus the only direct ionization is to that excited-metastable term. As expected, the contribution from the ground-metastable terms to the total ionization is minor (typically $<1\%$) while the contribution from the excited-metastable terms is significantly larger (up to 15% at the peak). The remaining contribution must again be from excitation-autoionization/Auger processes.

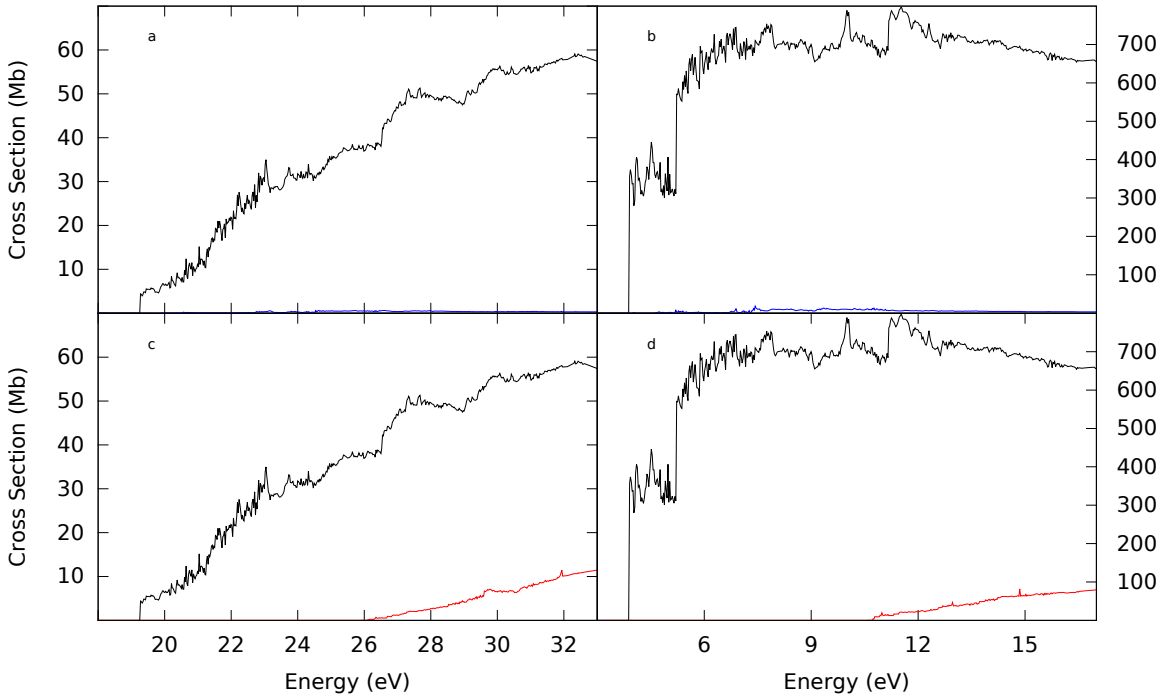

Figure 2.10: Comparison between total cross section (black), contribution from $2s^2nl$ terms (blue), and contribution from the $2s2pnl$ terms (red) for $1s^22s2p^2(^4P)$ (plots a and c) and $1s^22s2p(^3P^o)3s(^4P^o)$ (plots b and d).

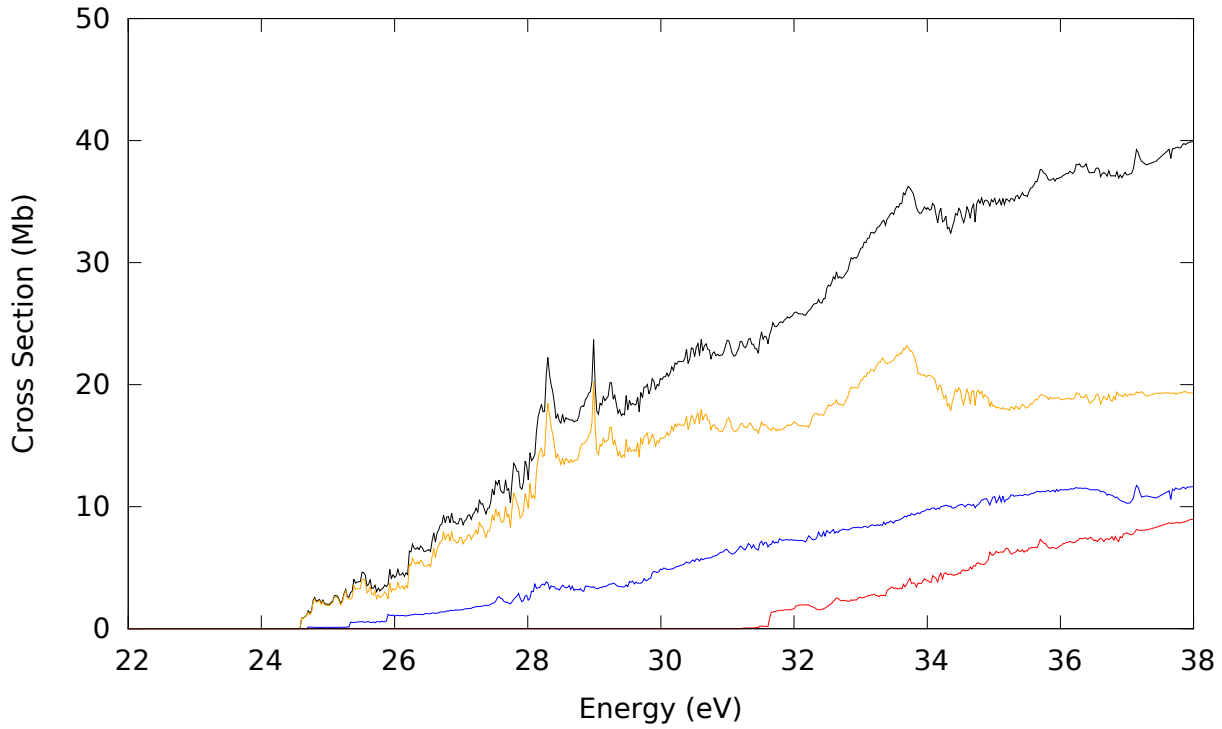

Figure 2.11: Comparison between total cross section (black), contribution from $2s^2nl$ terms (blue), contribution from the $2s2pnl$ terms (red), and contibution from the excitation-autoionization/Auger processes (orange) for ionization from $1s^22s^22p(^2P^o)$.

Finally, Figures 2.11 and 2.12 again show the ionization cross sections from the $1s^22s^22p(^2P^o)$ and $1s^22s2p^2(^4P)$ terms, where the black line is the total, blue is the direct ionization to the ground of C^{2+}, red is the direct ionization to the metastable of C^{2+}, and the orange line is the contribution from the excitation-autoionization/Auger (indirect) processes. In both cases the indirect processes are the largest contributor to the total cross section, typically >70% for the $1s^22s^22p(^2P^o)$ term and 80-100% for the $1s^22s2p^2(^4P)$ term. For the 6.5 eV range between the ionization potentials for the ground and metastable terms of C^{2+}, the indirect processes must terminate in the ground term of C^{2+}. For energies above this range, however, it is not immediately apparent whether individual excitation-autoionization/Auger processes terminate in the ground or metastable term of C^{2+}.

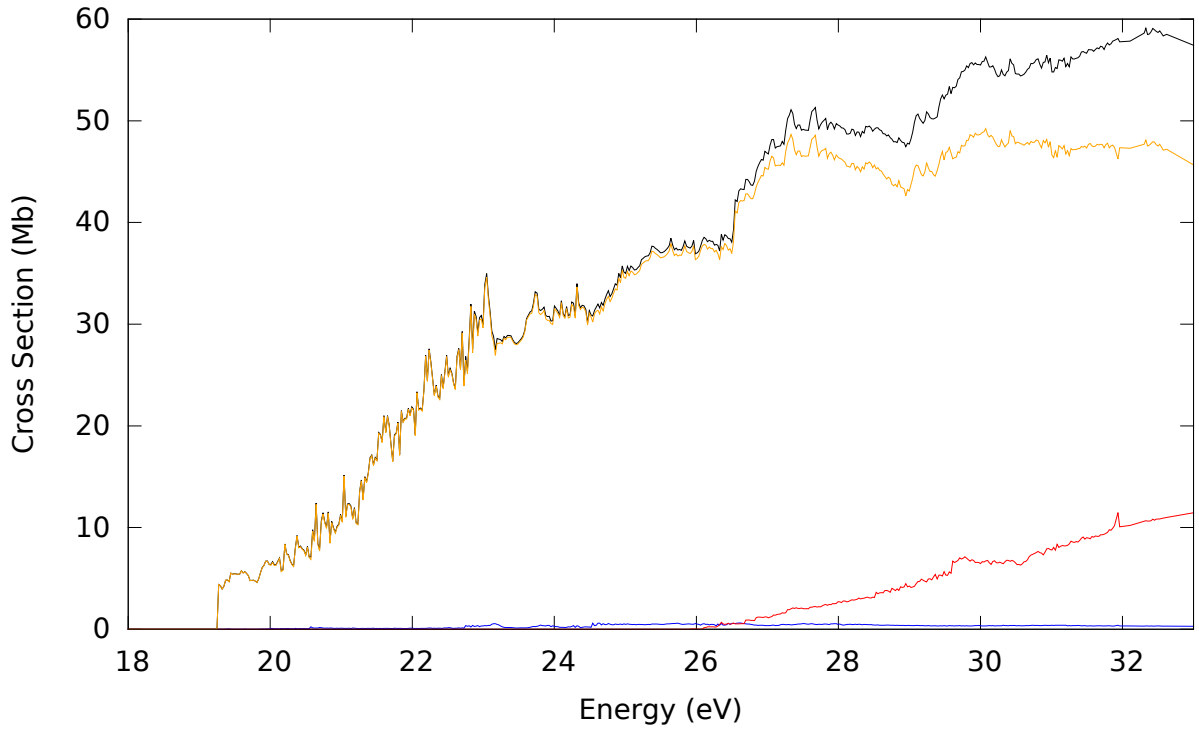

Figure 2.12: Comparison between total cross section (black), contribution from $2s^2nl$ terms (blue), contribution from the $2s2pnl$ terms (red), and contibution from the excitation-autoionization/Auger processes (orange) for ionization from $1s^22s2p^4(^4P)$.

This discussion illustrates that the R-Matrix method is an appropriate approach for resolving the ionized final state of a system, as long as an appropriately large configuration basis set is used. A further discussion of final-state resolution issues will be in Chapter 6.

Chapter 3

Electron-impact excitation of C^+

In this section, we will focus on the electron-impact excitation of C^+. New calculations are performed, with the aim of including higher n-shells than the data currently used in the ADAS database. The second motivation is to use the same atomic structure in the R-matrix electron-impact ionization and excitation cross sections, making it easier to match the initial levels of the excited state ionization cross sections with the target states in the excitation dataset.

3.1 Introduction and background

A number of previous calculations for the electron-impact excitation of C^+ have been published in the literature and the data are available for comparison. Calculations carried out in intermediate coupling have been performed most recently by Tayal et al. [37], including transitions between the 42 levels from the lowest 23 LS terms. We expand this to include all transitions between the lowest 125 levels. Tayal provides a comprehensive overview of prior calculations, so we will limit our citations to previous theoretical work to those that allow for direct comparison with the current work and to experimental results. Those include: R-matrix calculations by Keenan et al. [38], Luo and Pradhan [39], Blum and Pradhan [40], Wilson and Bell [41], and Wilson et al. [42]. Experimental measurements and theoretical calculations for the excitation cross sections for the $1s^2 2s^2 2p\ (^2Po) \rightarrow 1s^2 2s 2p^2\ (^4P)$, (^2D) and (^2S) were reported by Smith et al. [43].

The new dataset generated as part of this work will replace the existing ADAS data as the recommended data for C^+. Since the existing dataset is a hybrid with the effective collision strengths being taken from a number of sources, it is useful to provide a brief summary of the existing ADAS data. The current set includes the following configurations: $2s^22p$, $2s2p^2$, $2s^2nl$ (f3s<nl<5g), $2p^3$, $2p^2nl$ (3s <nl <3d).

The effective collision strengths in the existing dataset were taken from the Relativistic distorted-wave calculations of Zhang and Sampson [44] for transitions for the above configurations for nl <3d. The collision strengths involving the remaining levels were generated using plane-wave Born calculations based upon the Cowan atomic structure code. This level-resolved dataset was bundled to give term-resolved data, which was then supplemented with recombination and ionization data to produce the final adf04 file that was used to generate the existing ADAS GCR data for C^+.

3.2 Atomic structure

For our new excitation cross section calculations we used the same atomic structure for Models A and B as described in Section 2.2. Since we are only concerned with excitation processes between states below the C^{2+} 2s2p (^{3}P) threshold, we reduced the 2084 total levels from our Model B to the lowest 125 levels. The energies of the levels from ground through to the highest level were shifted to NIST values, as in the calculations for C^+ ionization. Table 3.1 provides a representative sample in the energy shift for the first eighteen levels. It can be seen that the differences between the calculated and NIST energies were relatively small.

3.3 Comparision with existing data

As with the ionization data in Chapter 2, we first compare our results with existing theoretical and experimental data to validate the reliability of our larger calculations. The

Configuration	Level	Energy (Ry)	NIST Energy (Ry)	Absolute Difference (Ry)
$1s^2 2s^2 2p$	$^2P^o_{1/2}$	0.000000	0.000000	0.000000
$1s^2 2s^2 2p$	$^2P^o_{3/2}$	0.001017	0.000578	0.000439
$1s^2 2s 2p^2$	$^4P_{1/2}$	0.386652	0.391875	0.005223
$1s^2 2s 2p^2$	$^4P_{3/2}$	0.387012	0.392075	0.005063
$1s^2 2s 2p^2$	$^4P_{5/2}$	0.387608	0.392333	0.004725
$1s^2 2s 2p^2$	$^2D_{3/2}$	0.697372	0.682836	0.014536
$1s^2 2s 2p^2$	$^2D_{5/2}$	0.697392	0.682813	0.014579
$1s^2 2s 2p^2$	$^2S_{1/2}$	0.939423	0.879316	0.060107
$1s^2 2s 2p^2$	$^2P_{1/2}$	1.038847	1.008082	0.030765
$1s^2 2s 2p^2$	$^2P_{3/2}$	1.039559	1.008459	0.031100
$1s^2 2s^2 3s$	$^2S_{1/2}$	1.064657	1.061584	0.003073
$1s^2 2s^2 3p$	$^2P^o_{1/2}$	1.182550	1.200361	0.017811
$1s^2 2s^2 3p$	$^2P^o_{3/2}$	1.182672	1.200462	0.017790
$1s^2 2s^2 3d$	$^2D_{3/2}$	1.303278	1.326343	0.023065
$1s^2 2s^2 3d$	$^2D_{5/2}$	1.303303	1.326356	0.023053
$1s^2 2p^3$	$^4S^o_{3/2}$	1.327434	1.294246	0.033188
$1s^2 2p^3$	$^2D^o_{3/2}$	1.398724	1.371153	0.027571
$1s^2 2p^3$	$^2D^o_{5/2}$	1.398761	1.371107	0.027654

Table 3.1: C^+ Model B energy levels compared with NIST energies.

inclusion of higher lying configurations can reduce the cross section of transitions between lower lying configurations, however the effect is usually small for the lowest transitions. Thus, we do not expect the inclusion of higher lying configurations to affect the excitation cross section between the lowest energy levels. Ground state electron-impact excitation cross-sections for the $1s^2 2s^2 2p\ (^2P^o) \rightarrow 1s^2 2s 2p^2\ (^4P)$ excitation are presented in Fig. 3.1. Due to the difficulty in extracting the resonance structure, the blue crosses provide only a representative sample of the B-spline R-Matrix calculation by Tayal [37]. The filled circles show the experimental results of Smith et al. [43]. The present models A and B are in very close agreement with the Tayal calculation and reasonable agreement with the Smith experiment.

Figures 3.2 and 3.3 show a comparison with two other excitation cross sections for transitions from the ground to low lying terms. Electron-impact excitation cross-sections for the $1s^2 2s^2 2p\ (^2P^o) \rightarrow 1s^2 2s 2p^2\ (^2D)$ excitation are presented in Fig. 3.2. The top half of the

figure shows the two current models compared with a representative sample of the Tayal [37] calculation; the bottom half shows the comparison with Lafyatis [45], Williams [46], and Smith [43] experiments. Both of our models are consistantly 10% lower than the Tayal calculation; these differences are likely due to the more involved resonance structure that arises from our extended calculation. We also show fairly good agreement with the measured values, typically falling within the experimental error bars.

Electron-impact excitation cross-sections for the $1s^2 2s^2 2p\ (^2P^o) \rightarrow 1s^2 2s 2p^2\ (^2S)$ excitation are presented in Fig. 3.3. Between the excitation threshold and 16 eV, both of our models are very close to the Tayal [37] calculation, showing only the expected differences due to the more involved resonance structure in the larger calculation. Above 16 eV, our results are consistently 20% lower than Tayal. Our calculations are just outside of the error bars for about half of the existing experimental data points[43]; however, it should be noted that obtaining absolute values from these excitation measurements is very challenging and it would not be unexpected for our cross sections to be a little lower than those of Tayal [37].

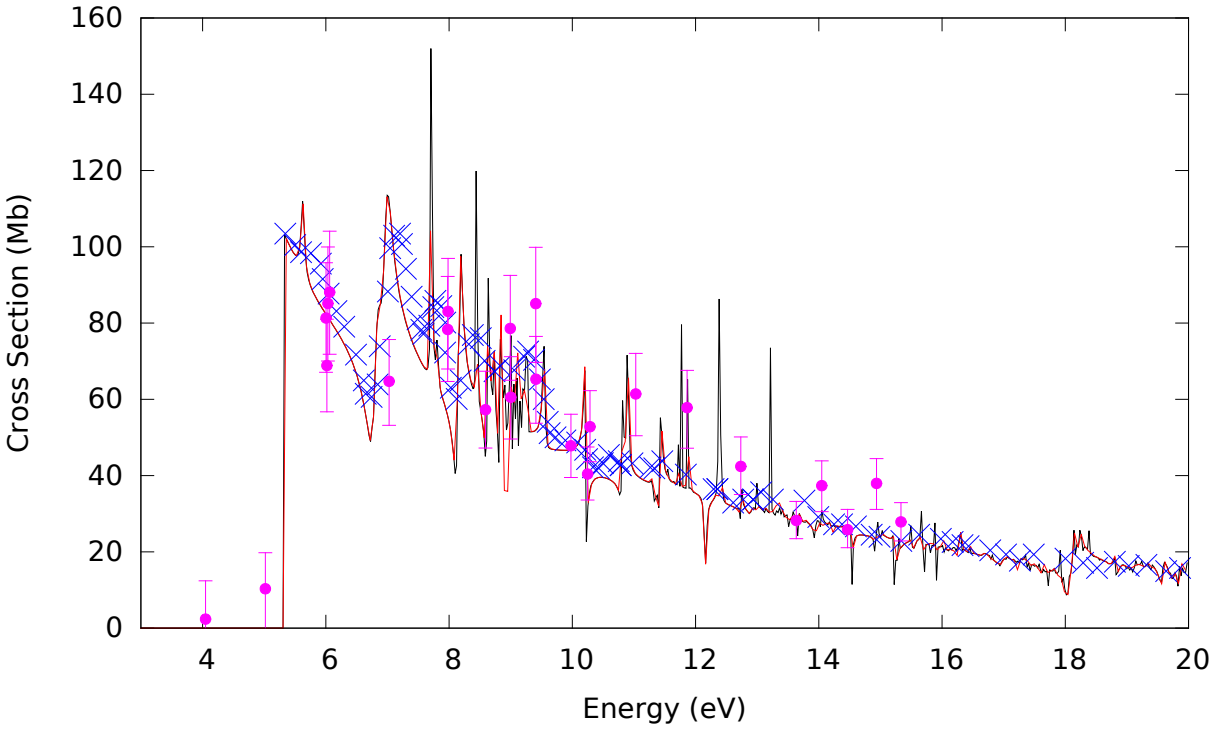

Figure 3.1: Electron-impact excitation cross section for $1s^2 2s^2 2p\ (^2P^o) \rightarrow 1s^2 2s 2p^2\ (^4P)$. Solid red curve, present Model A; Solid black curve, present Model B; blue crosses, Tayal R-Matrix; filled circles, Smith experiment.

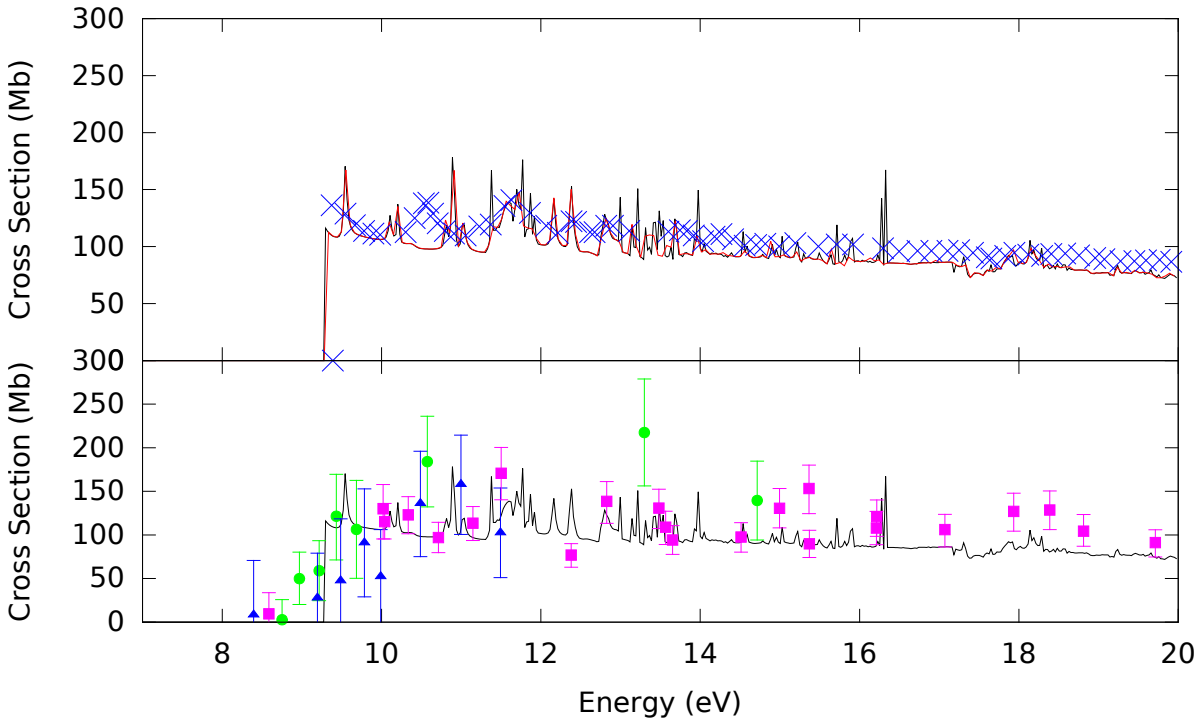

Figure 3.2: Electron-impact excitaiton cross section for $1s^2 2s^2 2p\ (^2P^o) \rightarrow 1s^2 2s 2p^2\ (^2D)$. Top: Solid red curve, present Model A; Solid black curve, present Model B; blue crosses, Tayal R-Matrix. Bottom: Solid black curve, present Model B; filled circles, Lafyatis experiment; filled triangles, Williams experiment; filled squares, Smith experiment.

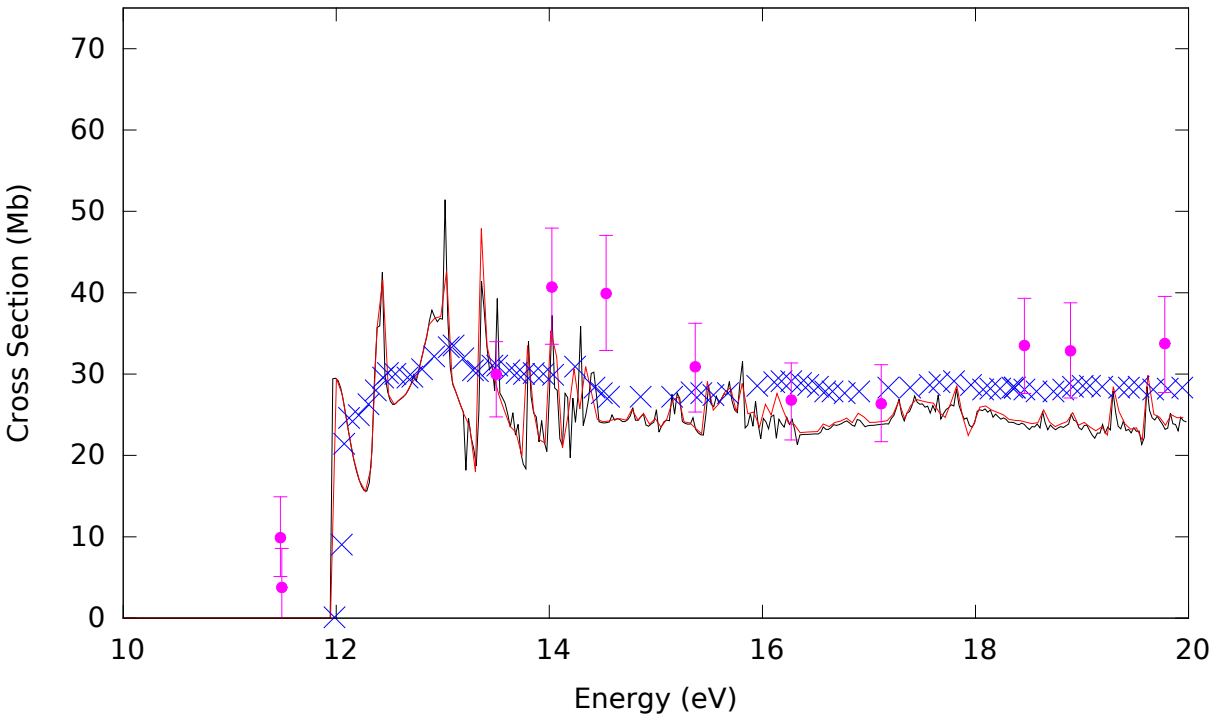

Figure 3.3: Electron-impact excitation cross section for $1s^2 2s^2 2p\ (^2P^o) \rightarrow 1s^2 2s 2p^2\ (^2S)$. Solid red curve, present Model A; solid black curve, present Model B; blue crosses, Tayal R-Matrix; filled circles, Smith experiment.

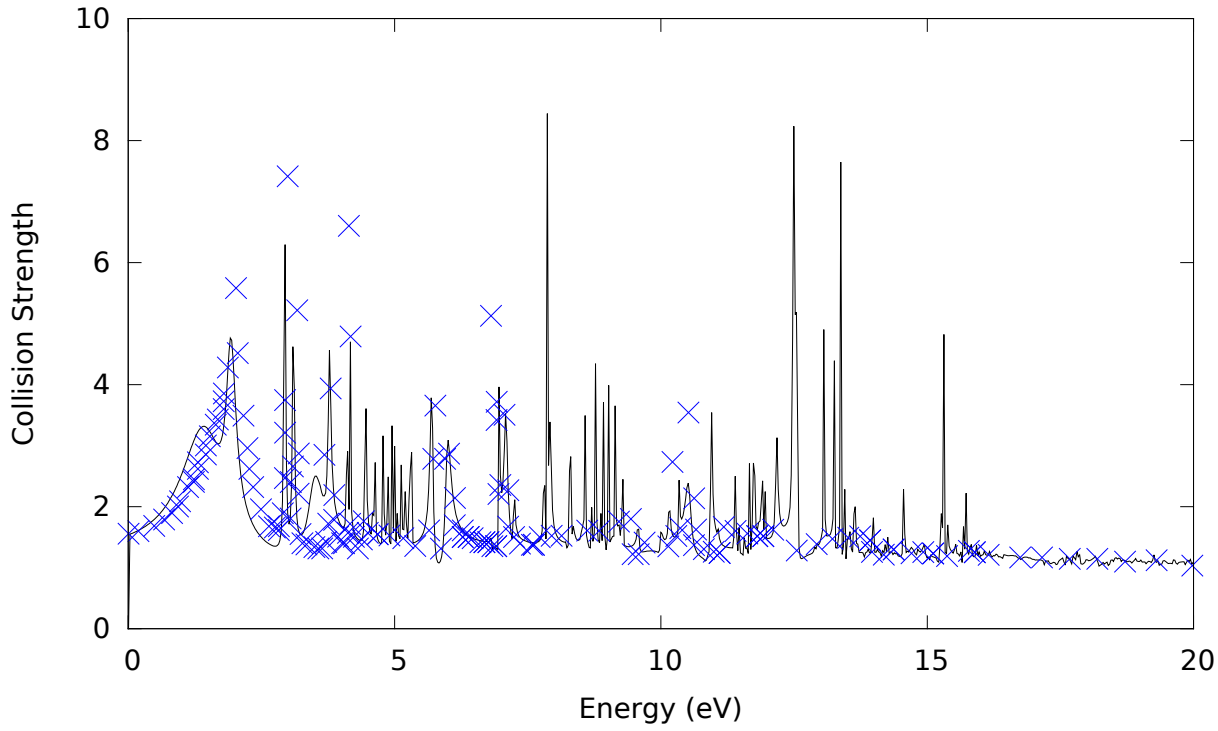

Figure 3.4: Electron-impact excitation collision strength for $1s^2 2s^2 2p\ (^2P^o_{1/2}) \rightarrow (^2P^o_{3/2})$. Solid black curve, present Model B; solid blue curve, Tayal R-Matrix.

Next we compare level-resolved excitation cross sections with those from the literature. Fig 3.4 shows the comparision between our Model B and Tayal R-Matrix [37] electron-impact excitation collision strength for the $1s^2 2s^2 2p\ (^2P^o_{3/2}) \rightarrow 1s^2 2s 2p^2\ (^2D_{5/2})$ transition. Our calculation shows very good agreement with the data of Tayal. Fig 3.5 shows the collision strength for the $1s^2 2s^2 2p\ (^2P^o_{1/2}) \rightarrow {}^2P^o{}_{3/2}$ transition. Our calculation was consistently around $10 - 15\%$ lower than Tayal. The differences in results with Tayal are likely due to the increased size of our calculation.

It can be seen that in general we have good agreement between the excitation cross sections from the new R-matrix calculations and with the available experimental measurements. There is a similar level of agreement with the available theoretical data, with some cross sections being a little smaller than the previously calculated values, something not unexpected considering the increased configuration set used in the new calculation. The other

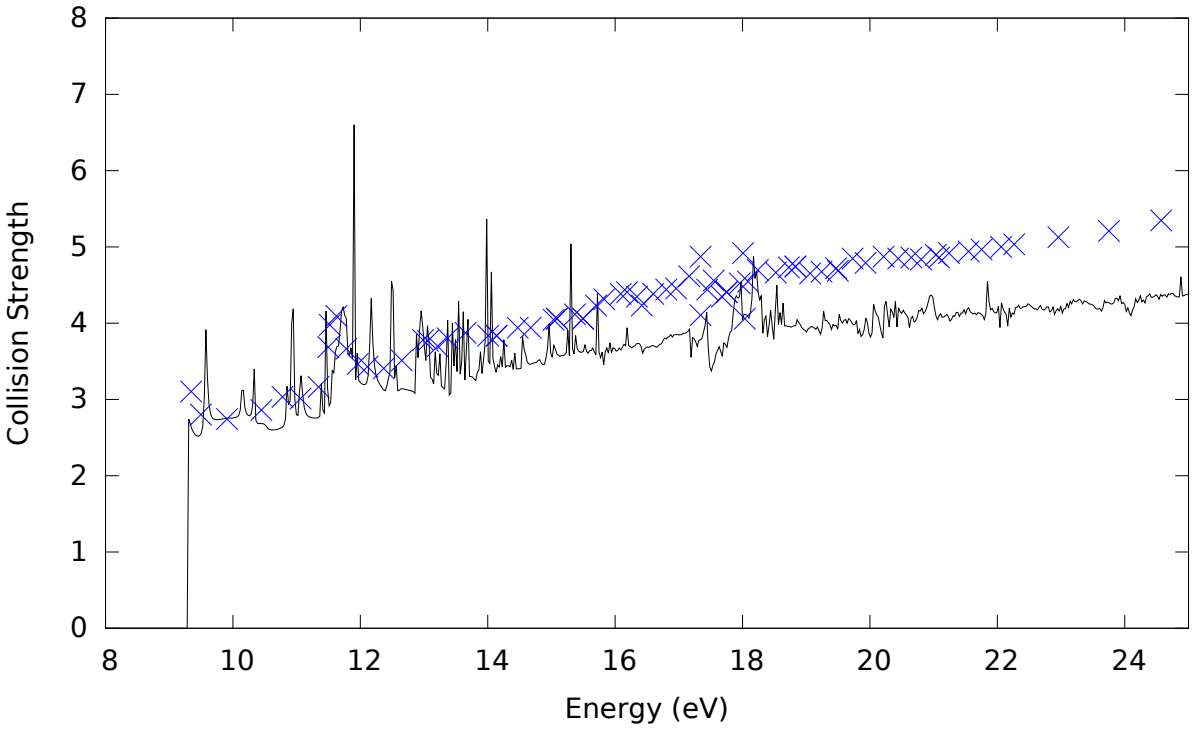

Figure 3.5: Electron-impact excitation collision strength for $1s^2 2s^2 2p\ (^2P^o_{3/2}) \rightarrow 1s^2 2s 2p^2\ (^2D_{5/2})$. Solid black curve, present Model B; solid blue curve, Tayal R-Matrix.

item of note is that the results from our models A and B are very similar. This indicates the likely convergence of the excitation results with the number of pseudostates included in the calculation.

3.4 Comparison with existing ADAS data

3.4.1 Populating the $1s^2 2s2p^2$ (^{4}P) excited metastable state

Since the excitation from the ground to the $1s^2 2s2p^2$ (^{4}P) metastable term is likely to be one of the main populating mechanisms for this term, it is of value to compare how the new excitation cross section and rate coefficients for this transition compare with the existing ADAS data. Figure 3.6 shows a comparison between the effective collision strength from our present Model B and the currently used ADAS data. As shown in Fig. 3.7, the effective collision strength from our calculation differs from ADAS by $1-5\%$ until around 1 million Kelvin, at which point the difference climbs to $20-25\%$. It should also be noted that our new calculation includes infinite energy points in the final cross section file, something not included in the previous dataset. Thus, the differences at higher temperature may be due to the inclusion of this high energy limit in the Maxwellian integration to generate the rate coefficients.

3.4.2 Transitions to excited terms in the $1s^2 2s2p^2$ configuration

As discussed in Section 1.1.2, there are many useful spectral lines arising from excited state transitions in C^+. The most common found were those arising from the $1s^2 2s2p^2$ (^{4}P, ^{2}D, ^{2}S) $\rightarrow$ $1s^2 2s^2 2p$ ($^2P^o$) multiplets. Thus, it would be interesting to look at the effective collision strengths from the ground term to the terms of the $1s^2 2s2p^2$ configuration.

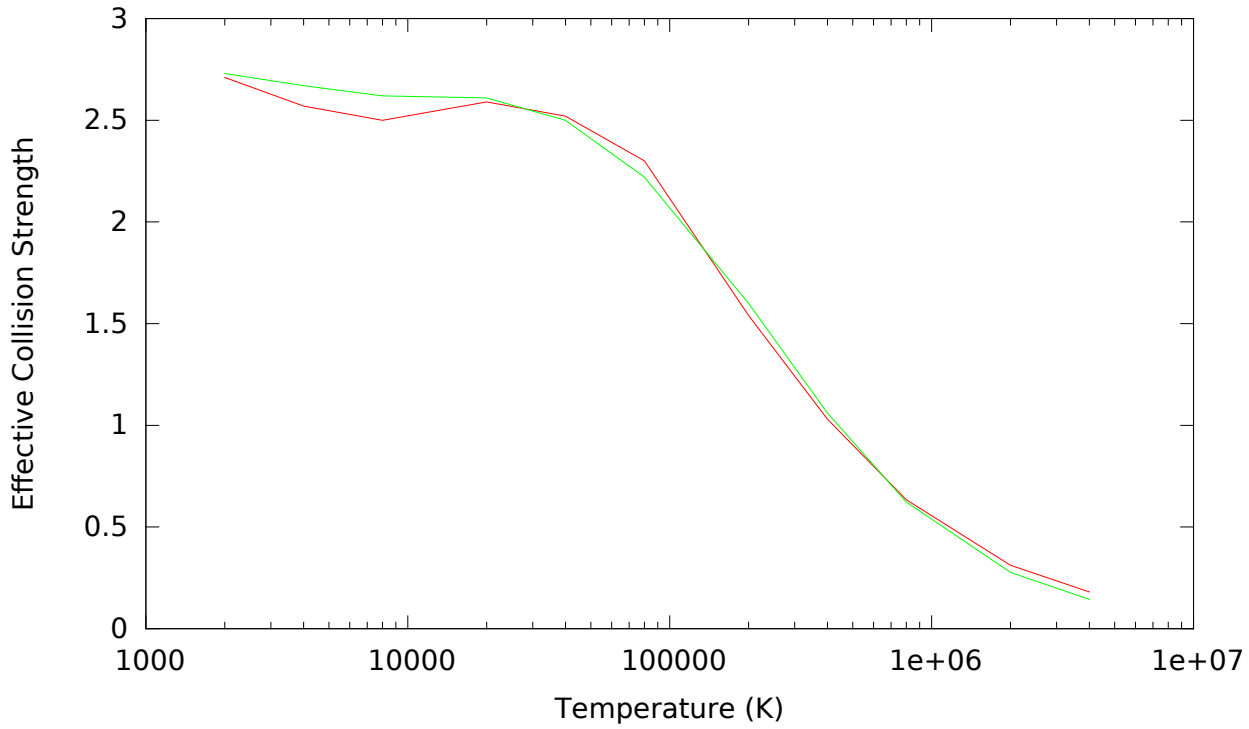

Figure 3.6: Effective collision strength for the $1s^2 2s^2 2p\ ^2P^o \rightarrow 1s^2 2s 2p^2\ ^4P$ excitation. Red is current ADAS data; green line is present Model B.

Figure 3.8 shows the comparisions for the six level-resolved transitions for $2s^2 2p\ (^2P^o) \rightarrow 2s 2p^2\ (^4P)$. All six comparision plots show similar behavior; that is, our Model B is typically $2-5\%$ higher than ADAS. The primary discrepancy between the data sets is in the $0-10,000K$ temperature range, where the ADAS data shows a local minimum and ours shows a smooth plateau. Figure 3.9 shows the comparison plots for level-resolved transitions of $2s^2 2p\ (^2P^o) \rightarrow 2s 2p^2\ (^2D)$. The two datasets agree to within $\sim$10% Figure 3.10 shows the comparisions between the level-resolved transitions for $2s^2 2p\ (^2P^o)$ and $2s 2p^2\ (^2S_{1/2})$. In this case, the differences are slighty larger, with up to $\sim$ 20% differences between the two dataset. Finally, 3.11 shows the effective collision strength for the $2s^2 2p\ (^2P^o_{1/2}) \rightarrow 2s 2p^2\ (^2P^o_{3/2})$ transition, showing very close agreement between the datasets (within 5%).

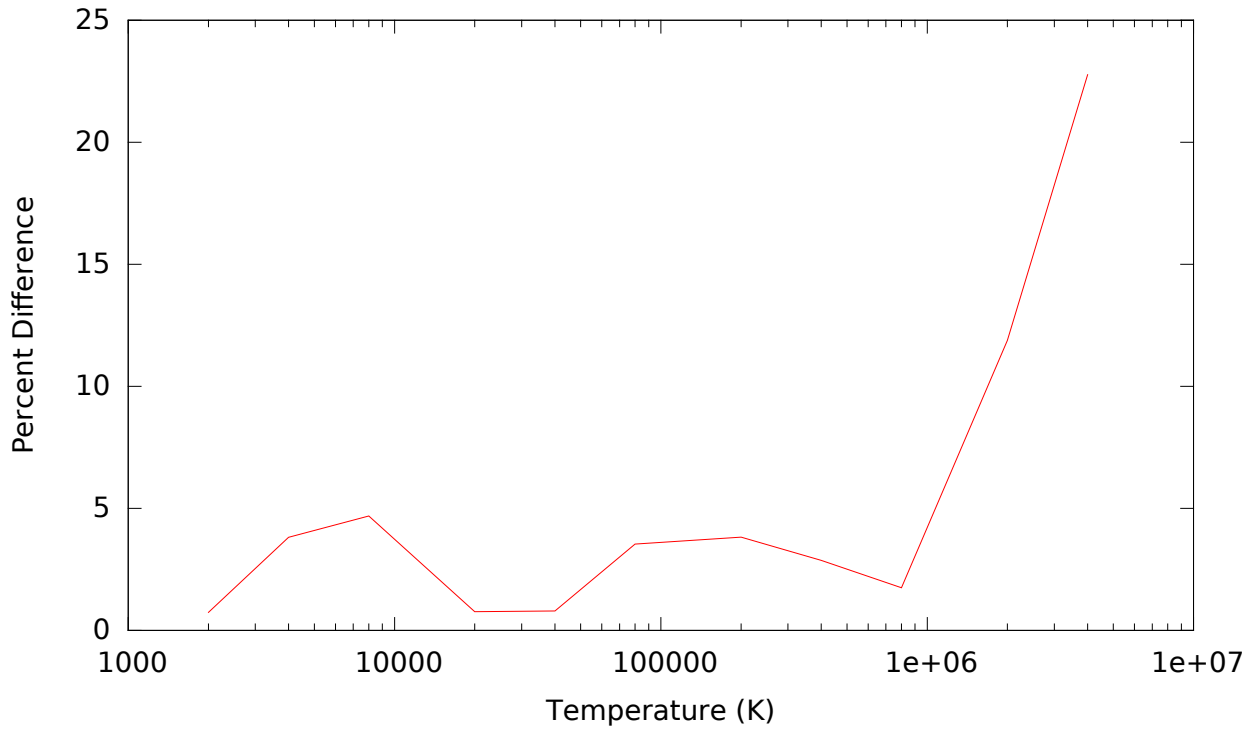

Figure 3.7: Percent difference between current ADAS data and present Model B effective collision strength for the $1s^2 2s^2 2p\ {}^2P^o \rightarrow 1s^2 2s 2p^2\ {}^4P$ excitation.

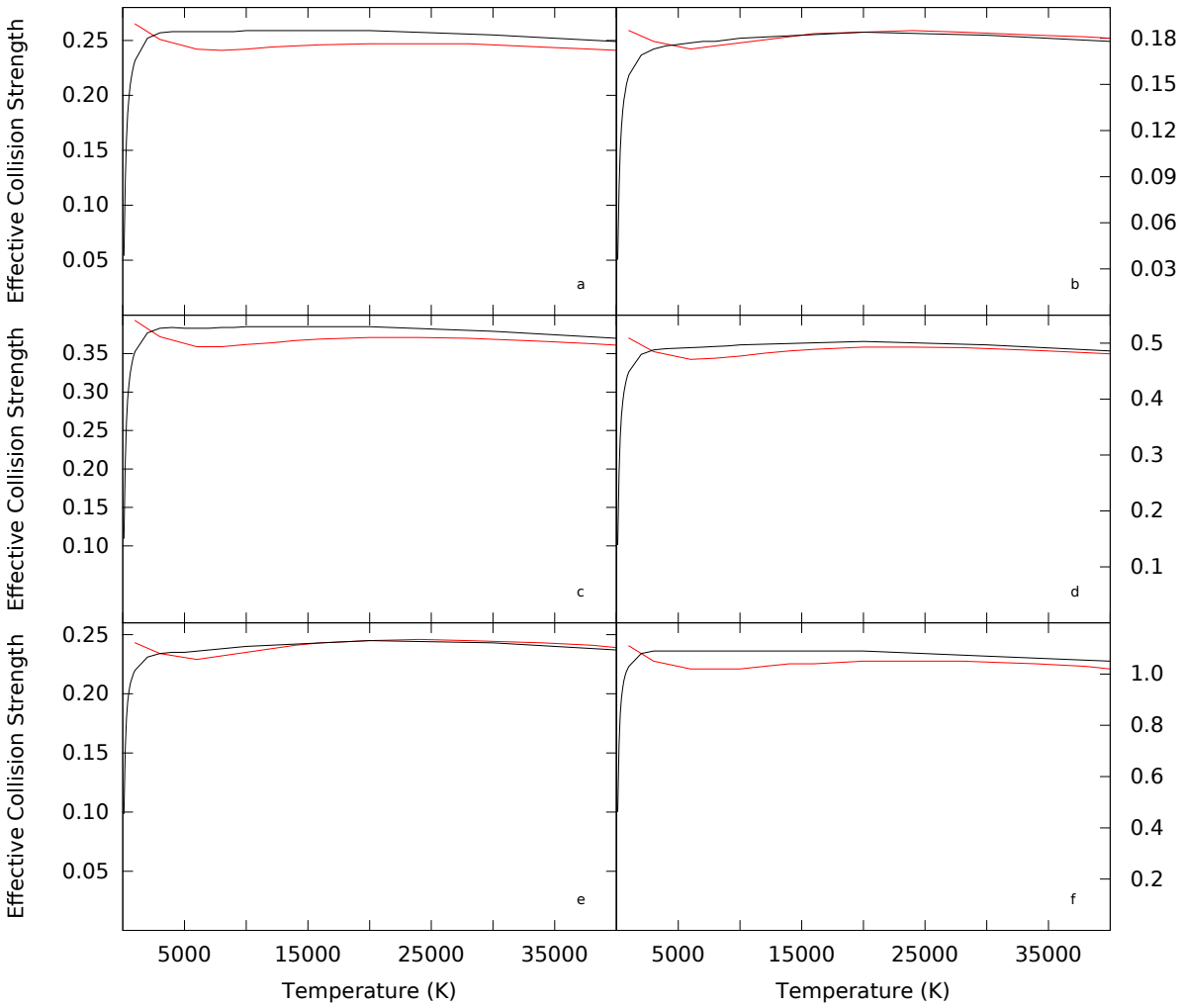

Figure 3.8: Effective collision strengths comparision between current Model B (black) and most recent ADAS data (red) for the $1s^2 2s^2 2p\ {}^2P^o_j \rightarrow 1s^2 2s 2p^2\ {}^4P_{j'}$ multiplet transitions. Listed as $j \rightarrow j'$: a) $1/2 \rightarrow 1/2$, b) $3/2 \rightarrow 1/2$, c) $1/2 \rightarrow 3/2$, d) $3/2 \rightarrow 3/2$, e) $1/2 \rightarrow 5/2$, f) $3/2 \rightarrow 5/2$

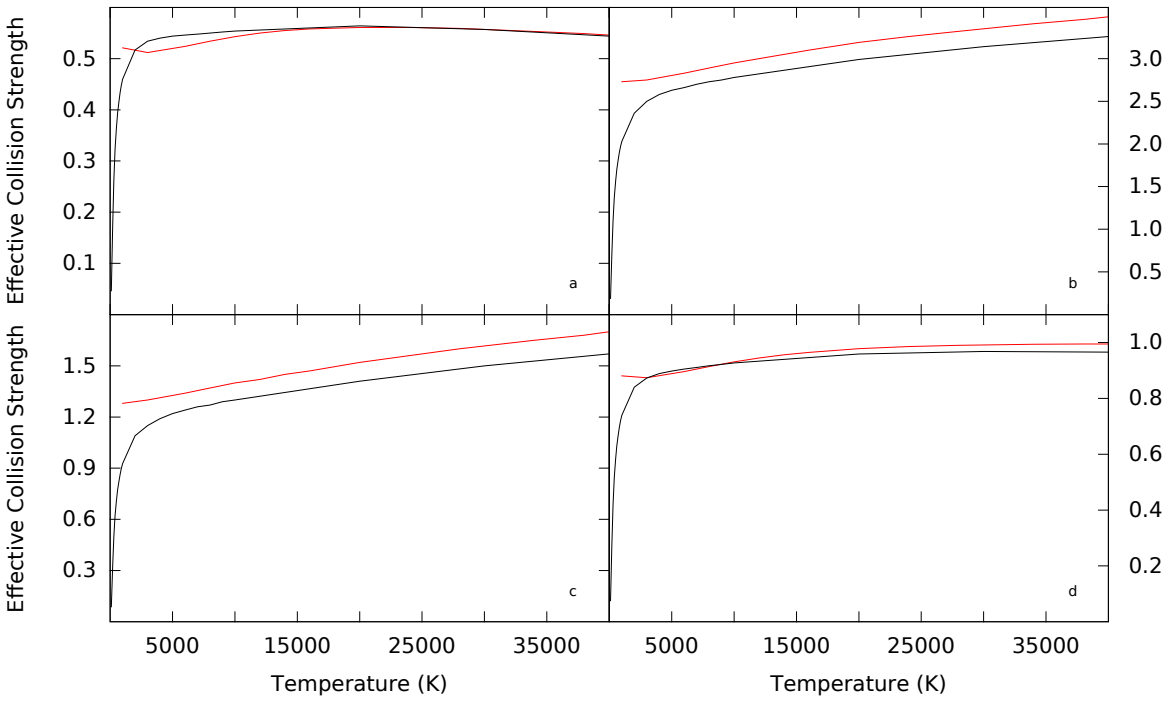

Figure 3.9: Effective collision strengths comparision between current Model B (black) and most recent ADAS data (red) for the $1s^2 2s^2 2p\ {}^2P^o_j \rightarrow 1s^2 2s 2p^2\ {}^2D_{j'}$ multiplet transitions. Listed as $j \rightarrow j'$: a) $1/2 \rightarrow 5/2$, b) $3/2 \rightarrow 5/2$, c) $1/2 \rightarrow 3/2$, d) $3/2 \rightarrow 3/2$

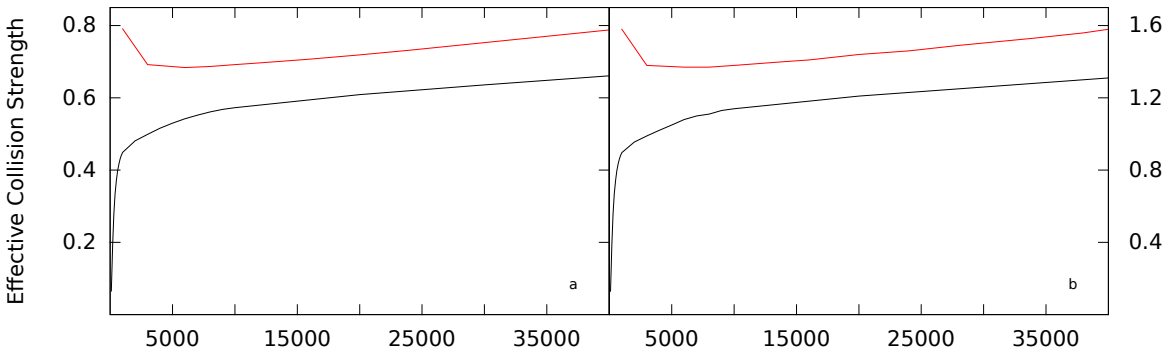

Figure 3.10: Effective collision strengths comparision between current Model B (black) and most recent ADAS data (red) for the $1s^2 2s^2 2p\ {}^2P^o_j \rightarrow 1s^2 2s 2p^2\ {}^2S_{j'}$ multiplet transitions. Listed as $j \rightarrow j'$: a) $1/2 \rightarrow 1/2$, b) $3/2 \rightarrow 1/2$

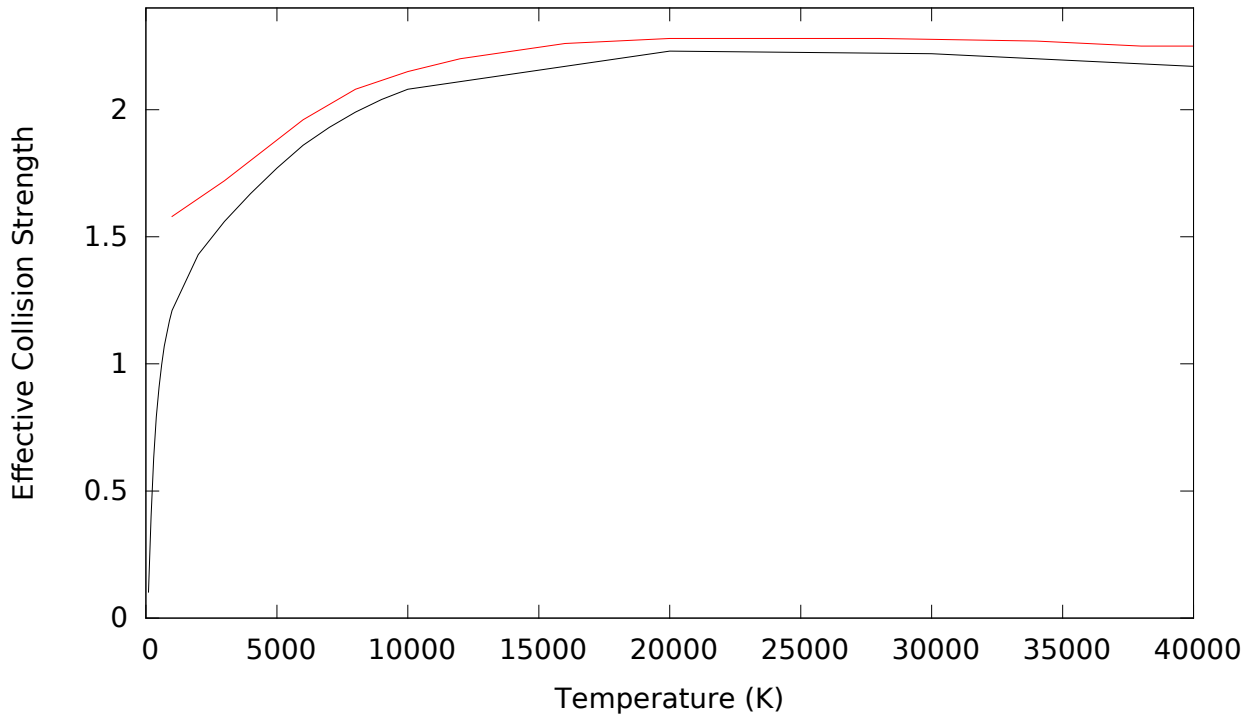

Figure 3.11: Effective collision strengths comparision between current Model B (black) and most recent ADAS data (red) for the $1s^2 2s^2 2p\ {}^2P^o_{1/2} \rightarrow 1s^2 2s 2p^2\ {}^2P^o_{3/2}$ transition.

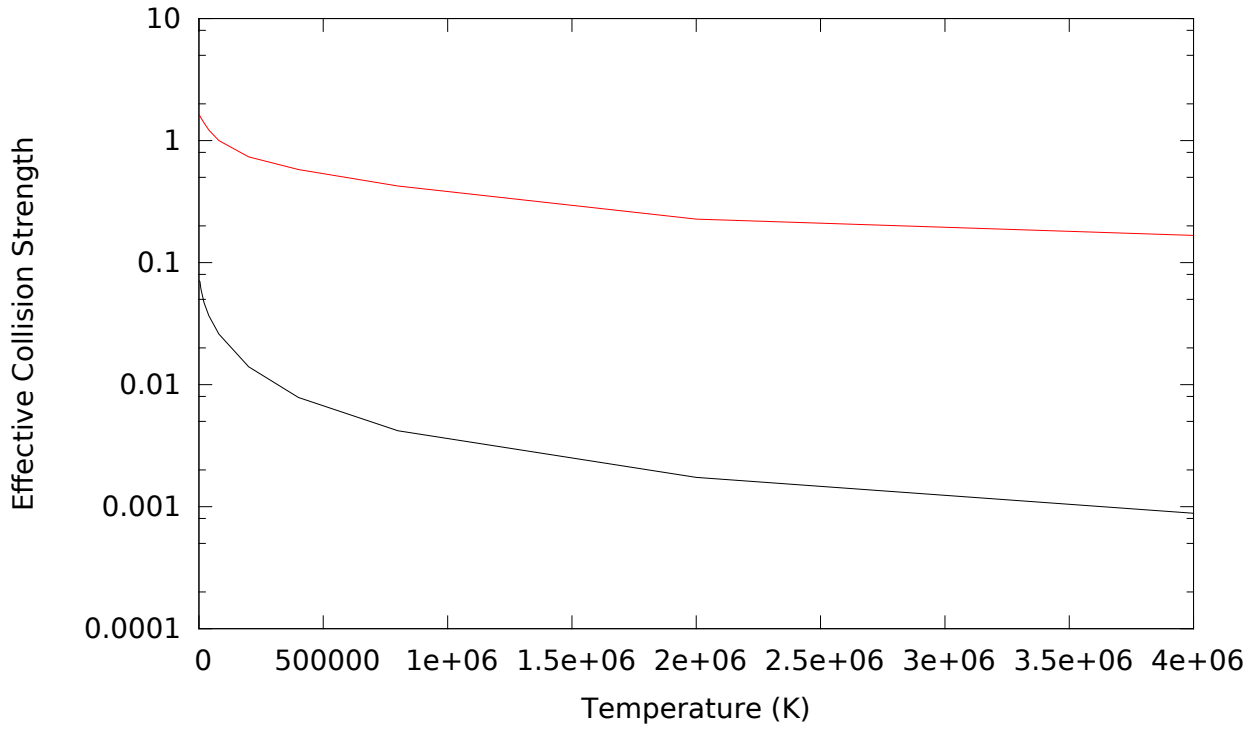

Figure 3.12: Effective collision strengths comparision between current Model B (black) and most recent ADAS data (red) for the $1s^2 2s 2p^2\ {}^4P \rightarrow 1s^2 2s 2p 3d\ {}^4F^o$ transition.

From the results of this comparison, the new data is not expected to produce large differences in the photon emissivity coefficients and line intensity values for the diagnostic lines that were mentioned. The largest differences would be in the $2s^2 2p\ ({}^2P^o)$ and $2s 2p^2\ ({}^2S_{1/2})$ multiplet.

3.4.3 Transitions to higher lying n-shells

As can be seen from the previous subsections, the new R-matrix results are in good agreement with previous R-matrix calculations and with relativistic distorted-wave calculations for excitation up to the first 3 n-shells. The higher n-shell data consists of effective collision strenghts generated using the more approximate Plane-Wave Born method. Thus, one might expect to see larger differences for excitation to these configurations.

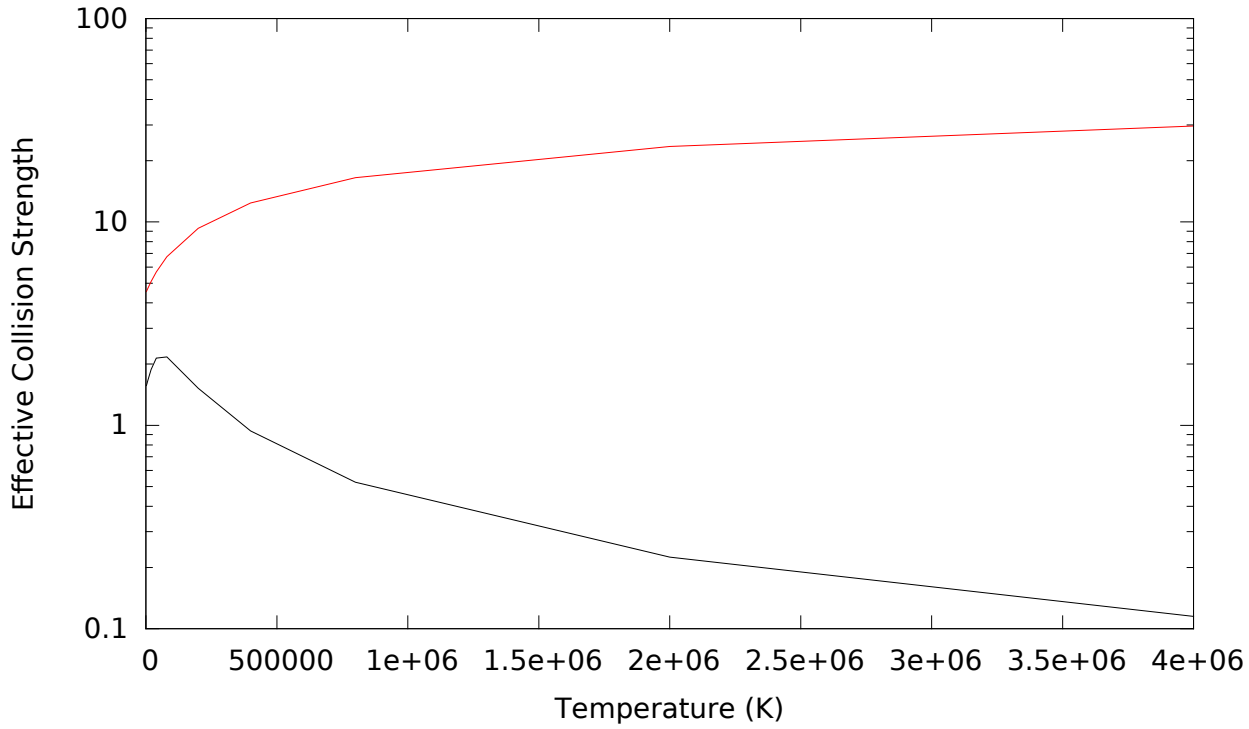

Figure 3.13: Effective collision strengths comparision between current Model B (black) and most recent ADAS data (red) for the $1s^2 2s 2p^2\ ^4P \rightarrow 1s^2 2s 2p 3d\ ^4D^o$ transition.

Figures 3.12 and 3.13 show the effective collision strength for the $1s^2 2s 2p^2\ ^4P \rightarrow 1s^2 2s 2p 3d$ ($^4P^o$, $^4D^o$) transitions. Our Model B produces rate coefficients a factor of $10 - 100$ smaller than the existing ADAS values. We would expect similar differences for all of the data created using the Plane-Wave Born method. Thus, users of the new dataset should expect to see quite large differences in the photon emissivity coefficients that involve these higher n-shells, compared to what the previous ADAS data would produce.

Chapter 4

Generalized Collisional-Radiative Modeling of C^+

The data from Chapters 2 and 3 –coupled with radiative and dielectronic-recombination rate coefficients –can be used to produce GCR rate coefficients for C^+. In this chapter a description is given of the fundamental data that is assembled to give the Generalized Collisional Radiative datafile in the specific format required for GCR processing. That is, we describe the electron-impact excitation, recombination, and ionization data. A particular focus is placed on the final state resolution of the ionization rate coefficients, a key component required for metastable-resolved GCR coefficients.

The ADAS code ADAS208 is based upon generalized collisional-radiative theory and was used to evaluate the GCR coefficients for C^+. Note that the final GCR dataset for C^+ will contain an additional contribution due to the higher n-shells, using a 'projection matrix' in the ADAS framework. This projection matrix uses approximate atomic data to supplement the high quality low n-shell data. The effect of these higher levels is projected onto the low lying levels and included in the final GCR effective rate coefficients. For the purposes of this chapter, however, we seek to determine the effects on the GCR coefficients due to the new excitation and ionization data from chapters 2 and 3. Thus, we generate GCR data using the low n-shell atomic data of this work and using the existing ADAS C^+ data, but we exclude the projection matrix for both. Without the projection matrix, the differences in the two data sets will be due solely to the changes in the fundamental data.

4.1 The behavior of the GCR coefficients

In this chapter, we explore the effect of our new data on three GCR coefficients: the effective ionization rate, effective recombination rate, and metastable cross-coupling rate coefficients. Before detailing the comparison with the new data, it would be useful to provide a summary of the general properties of the different GCR coefficients. Since the effective recombination and ionization rates are functions of both electron temperature and density, we use the 3-D plots in Figs. 4.1 and 4.2 to show the general trends for effective recombination and ionization rates.

At low temperatures the effective recombination rate coefficient (Fig. 4.1) shows a standard shape for dielectronic recombination, with this being the dominant recombination mechanism at most temperatures. As the density increases, the value of the recombination rate coefficient decreases slightly, due to some of the recombined electrons being electron-impact ionized before they have time to radiatively decay to the ground and metastable terms. At even higher electron densities, three-body recombination takes over and the rate coefficient increases dramatically, particularly at low temperatures.

The effective ionization rate coefficient is plotted in Fig. 4.2. At low electron densities the ionization rate coefficient is equivalent to the ground state ionization, and shows the characteristic temperature behavior of an ionization rate coefficient. As the electron density increases the excited states can be ionized before they have time to radiatively decay, producing an increase in the effective ionization rate coefficient. This increase can be up to a factor of 10 from the ground state ionization rate coefficient and is particularly pronounced for near neutral systems. Experimental evidence for this excited state ionization contribution was found previously using spectroscopic measurements on the DIII-D tokamak for neutral Li, see Fig. 4.3.

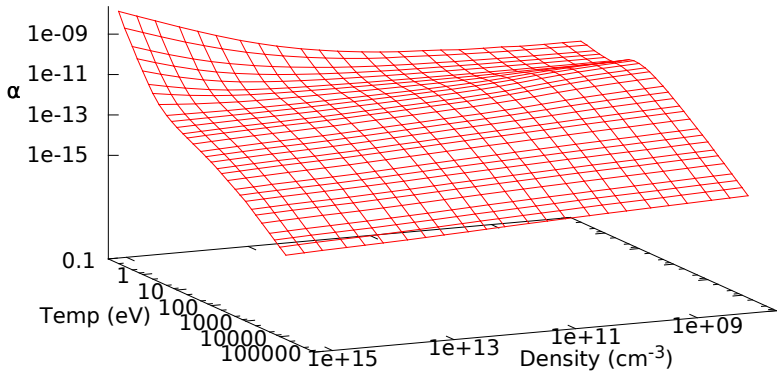

Figure 4.1: Recombination from C^{2+} to C^{+}

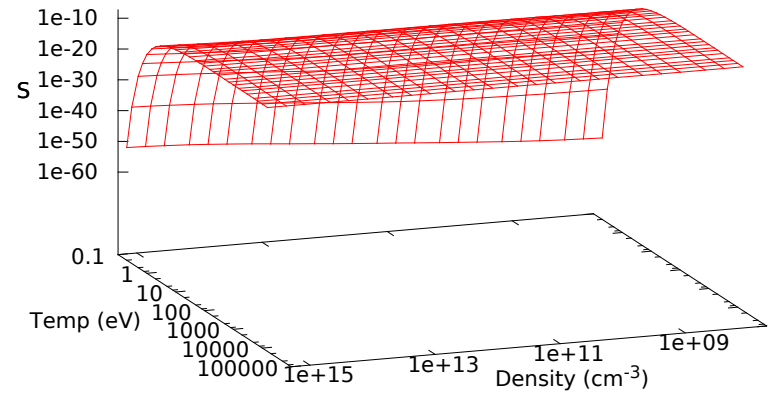

Figure 4.2: Ionization to C^{2+} from C^{+}

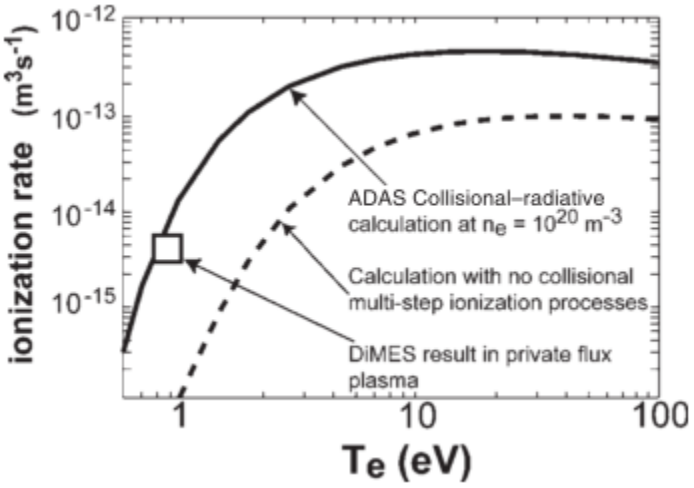

Figure 4.3: Ionization rate coefficients from ADAS, compared with measurements on DIII-D using their DiMES probe. Note the large increase in the rate coefficient for tokamak edge electron densities.

4.2 Fundamental Data for Electron-Impact Excitation

The electron-impact excitation data for the C^+ dataset is taken from the R-matrix calculation shown in Chapter 3. It was shown to be in agreement with available experimental measurements and was also in reasonable agreement with recent large-scale calculations. As outlined below, our new data includes all of the levels from the following configurations: $1s^22s^22p$, $1s^22s2p^2$, $1s^22s^2\ nl$ ($3s \leq nl \leq 5s$), and $1s^22s2pnl$ ($3s \leq nl \leq 5s$).

The level-resolved data generated from the Breit-Pauli R-matrix calculation was bundled into LS-resolved terms based on the statistical weight using the ADAS209 code. All levels below the C^{2+} $1s^22s2p$ (^3P) ionization potential were included in the adf04 file produced from the R-matrix calculation. Thus, some of the configurations with pseudo-orbitals had to be removed from the adf04 file (e.g. $1s^22s^2\ nl$ for $nl \geq 5p$), since they were only present to calculate the direct ionization of the ground and did not represent configurations with spectroscopic orbitals. The final adf04 file then contained 53 LS terms. The file contained both dipole and non-dipole radiative rates. The electric-dipole A-values were produced from the R-matrix calculation, and the non-dipole radiative rates were supplemented from a Multi-Configuration Breit-Pauli atomic structure calculation using the AUTOSTRUCTURE code[30]. Infinite energy limit points were also included in the R-matrix OMEGA file and were obtained using AUTOSTRUCTURE. Thus, the adf04 file also contains infinite energy limit points for many of the transitions.

4.3 Fundamental Data for Radiative and Dielectronic Recombination

We generate radiative recombination rate coefficients using a Gaunt factor approach [1] and added them to the electron-impact excitation rates from Chapter 3 (in a datafile called

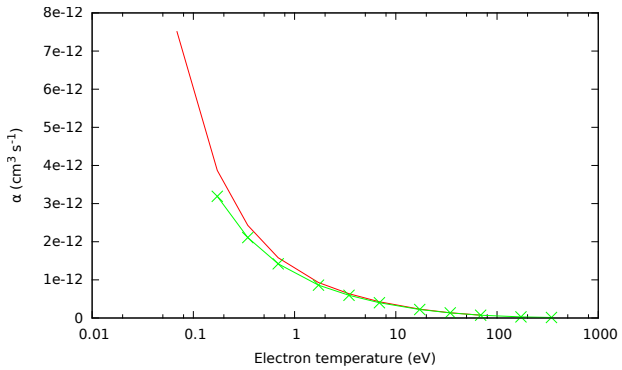

Figure 4.4: Total recombination rate coefficient (RR+DR) into the $2s^22p$ (^2P) term of C^+. The solid red line shows the results using the new dataset and the green line with crosses shows the current ADAS dataset.

adf04 file in ADAS notation). These rates were supplemented with dielectronic recombination rate coefficients from Multi-Configuration Breit-Pauli calculations from the DR project [47].

Thus, very similar recombination datasets are used in the new dataset and in the previous dataset. Figure 4.4 shows a comparison of the total recombination rate coefficient into the ground term of C^+. Note that the differences in the two datasets are relatively small, due to the very similar methods used in the calculation of the data. The differences shown in Fig. 4.4 is typical for the total recombination dataset for the other terms of C^+ in the two datasets. Thus, any differences in the effective recombination rate coefficients should be primarily due to either differences in the excitation datasets or to extra terms included in the new adf04 file.

4.4 Fundamental Data for Electron-Impact ionization

Of the different configurations included in the ionization calculation, ionization cross sections were extracted from the lowest 17 terms. This includes terms from $1s^22s^22p$, $1s^22s2p^2$,

$1s^2 2s^2$ nl (3s $\leq nl \leq$ 5s), and and $1s^2 2s2p3s$. Using the method outlined in chapter 2, it was possible to determine three ionization cross sections for each initial term: direct ionization to the $2s^2$ ground of C^{2+}, direct ionization to the 2s2p (^3P) metastable of C^{2+}, and the total ionization cross section. The total cross section would include the two possible direct ionization contributions, along with excitation-autoionization of doubly excited states above the ionization potential.

4.4.1 Final state resolution of the terms from the $1s^2 2s^2$ nl configurations

Considering the $1s^2 2s^2$ nl configurations, all of the direct ionization cross sections should lead to the ground term of C^2+, similarly much of the excitation-autoionization was to $1s^2 2s2p nl$ doubly excited states, which would then Auger to the ground term of C^{2+}. Thus, we assume that the total ionization cross section all leads to the ground term of C^{2+}.

To generate ionization rate coefficients the ionization cross section was convolved with a Maxwellian free-electron distribution function. A code was developed that used the raw R-matrix data up to the last calculated energy point, then performed a fit to the RMPS cross section that could be used to extrapolate the cross section to higher energies. The fit was based upon a well known fit [48], which also contains a high energy limit point. The high energy limit point was calculated from a photo-ionization cross section calculation.

The figures below (4.5 and 4.6) show the $2s^2 nl$ cross sections, along with the high-energy fitted lines. Also shown are the equivalent distorted-wave direct ionization cross sections. Note that two RMPS cross sections are shown on each plot, one is the total cross section and the other corresponds to direct ionization to the ground term of C^{2+}. It can be seen that the RMPS results for the direct ionization to the ground of C^{2+} are slightly below the

distorted-wave direct ionization cross sections to the ground, as is expected since the perturbative method tends to overestimate the cross section. It is also clear that there is significant excitation-autoionization present in all of the cross sections, with this contribution becoming smaller for higher excited terms. This is also expected behavior since the higher energy terms have progressively smaller ionization potentials, thus the direction ionization should begin to dominate the excitation-autoionization contribution. It is also apparent that the distorted-wave results are becoming progressively worse as one progresses to higher excited terms, which is consistent with previous cases [49].

Consider next the ionization from the 2s2p3s configuration shown in Fig.4.7. In this case, there is no direct process for ionization to the ground term. The direct ionization to the ground of C^{2+} is indeed negligible, and the direct ionization to the metastable of C^{2+} is slightly below the CADW values. There is, however, a large contribution from the ground ionization potential and higher. This can only be due to excitation-autoionization (e.g. to a $2p^2$ 3s configuration). It is likely that the majority of the doubly excited states would be followed by an Auger decay to the ground of C^{2+}. Thus, in determining the metastable population, we allocate this ionization contribution to the ground of C^{2+}, while the direct metastable contribution is allocated to the 2s2p (^{3}P) metastable. It is also of note that this cross section is slightly unusual in that there is excitation-autoionization below the first allowed direct ionization cross section threshold.

Finally, consider next the ionization from the $2s^22p$ (^2P) ground term in Fig.4.8. In this case, there is direct ionization to the ground of C^{2+}, direct ionization to the metastable of C^{2+}, and excitation-autoionization. We again assume that the excitation-autoionization leads to the ground of C^{2+}. We processed the other cross sections in a similar manner and

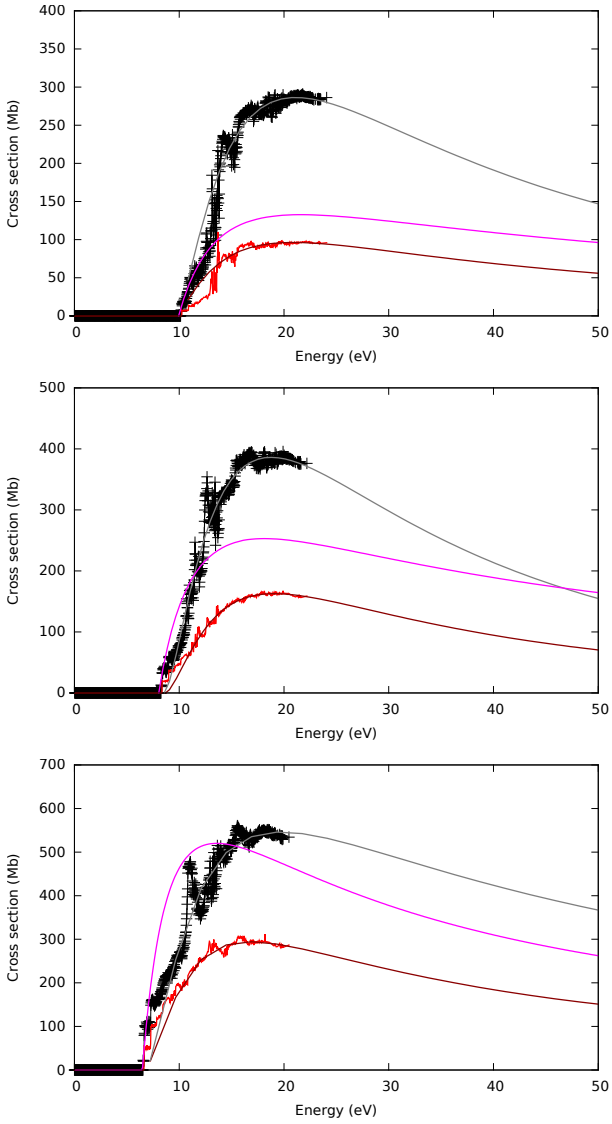

Figure 4.5: Ionization cross sections for the $1s^2 2s^2 3l$ configurations: 3s (top), 3p(middle), 3d (bottom). RMPS results are shown for the total ionization cross section (black crosses) and for direct ionization to the ground of C^{2+} (red lines). Also shown are the fits to the RMPS data (gray and dark red lines) and the CADW results for ionization to the ground term of C^{2+} (magenta lines).

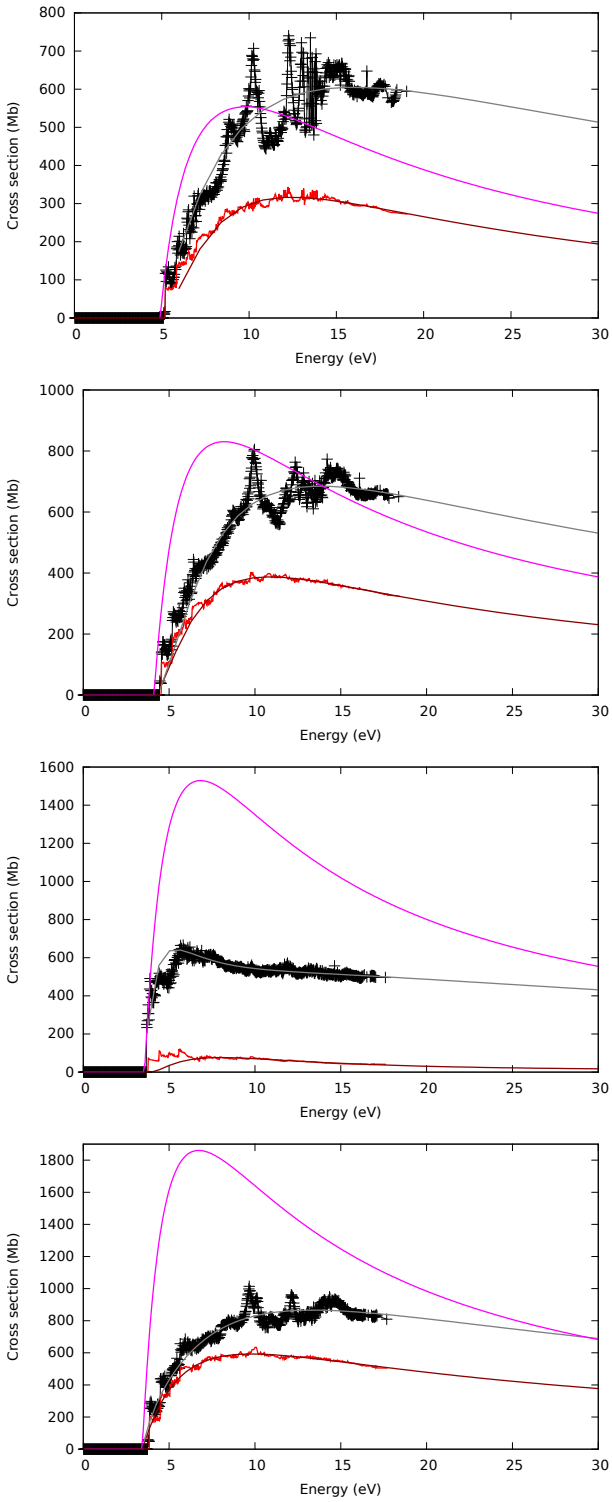

Figure 4.6: Ionization cross sections for the $1s^2 2s^2 4l$ configurations: 4s, 4p, 4d, and 4f (top to bottom). RMPS results are shown for the total ionization cross section (black crosses) and for direct ionization to the ground of C^{2+} (red lines). Also shown are the fits to the RMPS data (gray and dark red lines) and the CADW results for ionization to the ground term of C^{2+} (magenta lines).

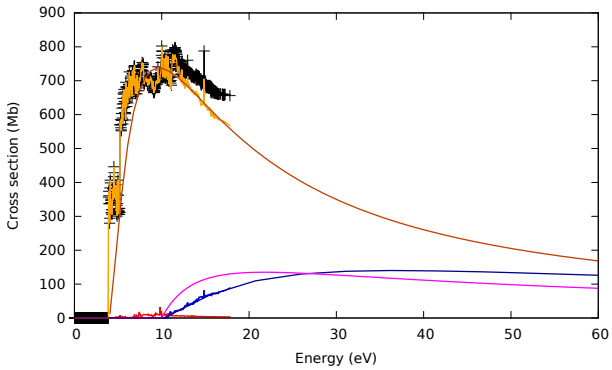

Figure 4.7: Ionization cross sections for the (^4P) term of the $1s^2 2s2p3s$ configuration. RMPS results are shown for the total ionization cross section (black crosses) and for direct ionization to the ground of C^{2+} (red line). Also shown are the fits to the RMPS data (dark orange and dark blue lines) and the CADW results for ionization to the ground term of C^{2+} (magenta line).

added the set of final-state resolved ionization rate coefficients to the adf04 file for subsequent GCR processing.

4.5 Non-metastable resolved

The simplest GCR datasets would be those for the 'stage-to-stage' ionization balance calculations (i.e., no metastable resolution). In this case there is one recombination rate coefficient from C^{2+} to C^{+} and one ionization rate coefficient from C^{+} to C^{2+}, with each coefficient being a function of electron temperature and density.

Figure 4.9 shows the effective recombination rate coefficient, comparing the new GCR data with that generated from the previous ADAS dataset. Note that for the purposes of this comparison no contribution from the projection matrix (higher n-shells) is included in the effective recombination rate coefficient, to isolate the differences due to the new atomic data. The final GCR dataset will have the projection matrix included. The rate coefficient is not strongly density-dependent. The reduction in the α coefficient with density shown

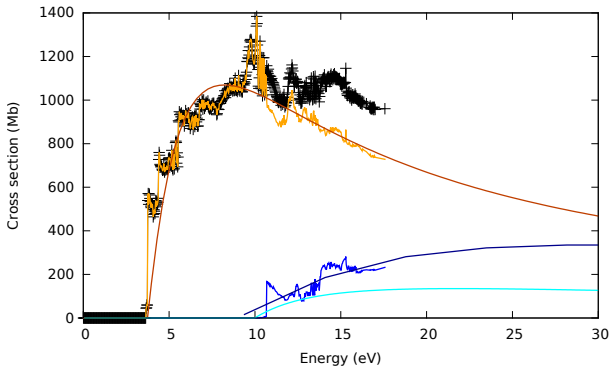

Figure 4.8: Ionization cross sections for the (^2P) term of the $1s^2 2s2p3s$ configurations. RMPS results are shown for the total ionization cross section (black crosses) and for direct ionization to the ground of C^{2+} (red line). Also shown are the fits to the RMPS (dark orange and dark blue lines) data and the CADW results for ionization to the metastable term of C^{2+} (cyan line).

earlier in this chapter is primarily to do collisional ionization of the high-n states in the projection matrix occurring before the excited states have a chance to radiate to a lower term. The collisional-redistribution effects are not as strong on the low n-shells in the adf04 file. Thus, we only show the differences as a function of electron temperature. The differences are within $\sim 50\%$, with this primarily being due to extra terms in the new adf04 file providing additional recombination channels.

Figure 4.10 shows the differences in the stage-to-stage effective ionization rate coefficient. The differences can be quite large at low temperatures, up to 80%. However, it should be noted that at these temperatures the rate coefficients are very small and so the differences do not have a large impact on the effective ionization. The temperature range for which the fractional abundance of C^+ is greater than 1% is about $0.5eV$ to about $8eV$. In this temperature range, the differences between our data and the current ADAS data are around 20 – 50%, which is consistent with the differences in the new RMPS ionization data as compared to the distorted-wave and ECIP data that is currently in the ADAS datafile.

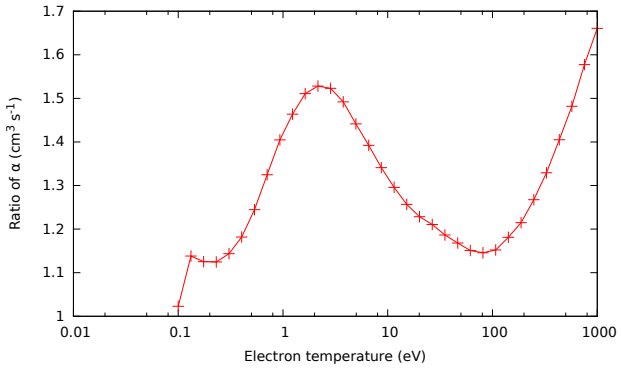

Figure 4.9: The ratio of the $C^{2+} \rightarrow C^{+}$ effective recombination rate coefficients for N_e=1×10^8 cm^{-3} as a function of electron temperature. Note that this comparison is not metastable resolved.

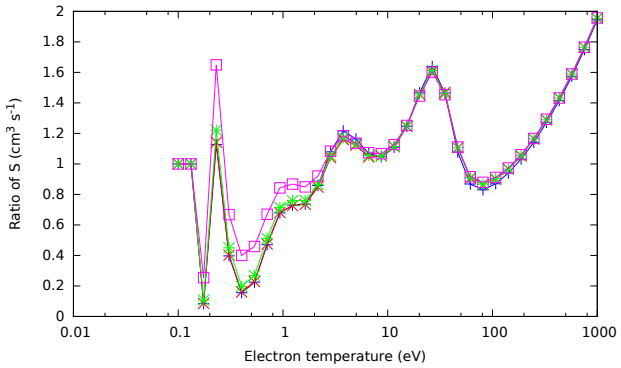

Figure 4.10: The ratio of the effective ionization rate coefficients for N_e=1×10^8 (blue), 1×10^{12} (red), 1×10^{13} (green), and 1×10^{14} (magenta) cm^{-3} as a function of electron temperature. Note that this comparison is not metastable resolved.

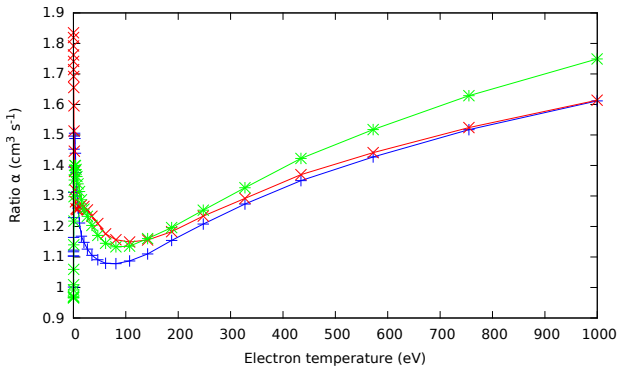

Figure 4.11: The ratio of the effective recombination rate coefficients for N_e=1×10^8 cm^{-3} as a function of electron temperature. Results are shown for $C^{2+} \rightarrow C^{+}$ metastable terms: $2s^2(^1S) \rightarrow 2s^22p(^2P)$ (blue), $2s^2(^1S) \rightarrow 2s2p^2(^4P)$ (red), and $2s2p(^3P) \rightarrow 2s2p^2(^4P)$ (green).

4.6 Metastable resolved

Figure 4.11 shows the effective recombination rate coefficient for a sample of the metastable resolved rate coefficients. As in the non-metastable case, the dependence on electron density is quite weak. The differences are again within $\sim$ 50%, with the changes being due to the extra recombination channels included in the new dataset.

As shown in Fig. 4.12, the new ionization data has a very pronounced effect on the metastable-resolved ionization rate coefficient. Note that the ionization from the ground of C^+ to the metastable of C^{2+} shows the largest difference, though mostly at very low temperatures when the rate coefficients are already very small. The other metastable resolved ionization rate coefficients have differences of up to a factor of two in the temperature region of interest, while the ionization from the C^+ ground to the C^{2+} metastable has difference of more than a factor of 10 in the appropriate temperature region. The differences can be traced to the ionization rate coefficient being significantly smaller in the previously used ADAS datafile. As a consistency check on the RMPS rate coefficient, CADW cross sections were used to generate rate coefficients and they were similar in magnitude to the RMPS results while being much greater than the existing ADAS rate coefficient for this transition.

Thus, the new RMPS rate coefficient for this transition is our recommended value.

4.7 Summary

In this chapter an overview has been given of a new GCR dataset for C^+. A method was described that allowed the final state of the C^{2+} ion to be identified in the RMPS ionization cross sections. The new GCR recombination rate coefficients show small differences with the previous ADAS dataset, as does the state-to-state GCR ionization rate coefficient. Quite large differences are observed in the metastable resolved GCR ionization rate coefficients and we expect the new atomic data to make a significant difference in the modeling applications.

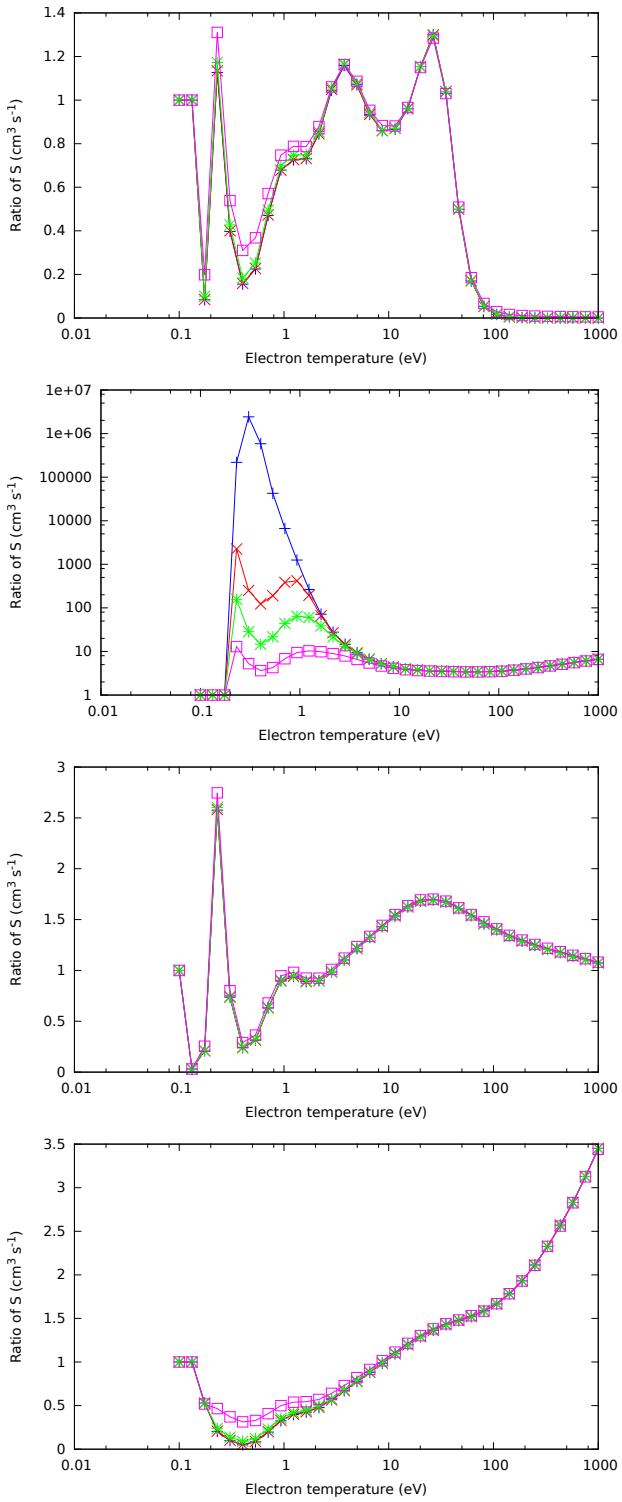

Figure 4.12: The ratio of the new effective ionization rate coefficients to the current ADAS rate coefficient for N_e=1×10^8 (blue), 1×10^{12} (red), 1×10^{13} (green), and 1×10^{14} (magenta) cm^{-3} as a function of electron temperature for the $C^+ \rightarrow C^{2+}$ metastable terms: $2s^2 2p(^2P) \rightarrow 2s^2(^1S)$, $2s^2 2p(^2P) \rightarrow 2s2p(^3P)$, $2s2p^2(^4P) \rightarrow 2s^2(^1S)$, $2s2p^2(^4P) \rightarrow 2s2p(^3P)$ (top to bottom).

Chapter 5

Electron-impact excitation of Ar^{2+}

5.1 Introduction and background

In very low temperature astrophysical plasmas, such as H II regions, the energy in the free electrons and protons is not sufficient to excite any atoms or ions outside of their ground terms. Thus, any excitation (electron or proton-impact) tends to excite just within the levels of the ground term. So in Ar^{2+} this would correspond to transitions between the J=0,1, and 2 levels of the $1s^2 2s^2 2p^4$ (^3P) term. As a result, these fine structure emission lines becomes an important power loss mechanism from the plasma, something not encountered in typical higher temperature plasmas. The challenge is that these plasmas can have temperatures as low as 10 K. The work presented in this chapter is aimed at improving the electron-impact excitation data for such power loss studies for Ar^{2+}. Collaborators on this project are working on proton-impact excitation data for Ar^{2+} that will be combined with the data recommended in this chapter and used in astrophysical models.

Figure 5.1 shows a sample spectrum from an H II region. Note the very narrow spectral features, these correspond to low temperature fine-structure transitions from a number of elements, including argon. One of the Ar III lines is marked in the spectrum. An accurate knowledge of the low temperature fine-structure excitation rates is important in understanding such ultra low temperature plasmas.

In this chapter, we produce new scattering cross sections for fine-structure electron-impact transitions within the ground term of Ar^{2+}. The R-Matrix method is used to solve both the Breit-Pauli Hamiltonian and the fully-relativistic Dirac equation. The focus of

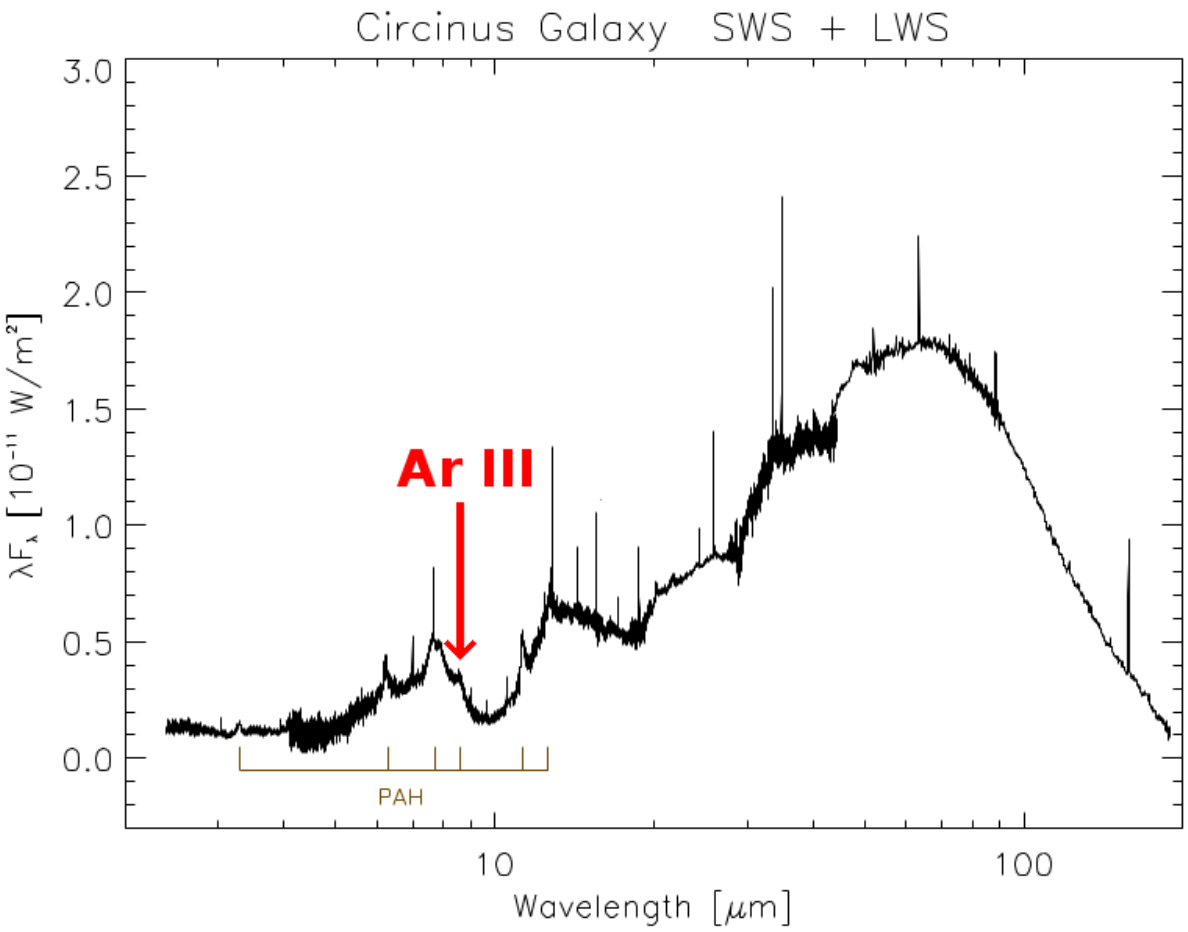

Figure 5.1: Observation of the Circinus Galaxy with *ISO*. The very narrow spectral lines, as a consequence of long upper state lifetimes, are all due to fine-structure features in the ground term.

these calculations is on low collisional energies to allow for collision strength and rate coefficient calculations down to 10K. The BP and relativistic structure packages that we use and the R-matrix theory are outlined in section 1.2.4. Since the effective collision strengths are expected to be quite sensitive to the atomic structure, we use the calculations with the closest match to NIST energies and NIST A-values, as these should have the most accurate atomic structure.

5.2 Breit-Pauli and Dirac structure results

For the semi-relativistic (Breit-Pauli) calculation, we used the atomic structure package AUTOSTRUCTURE [30] to generate the radial orbitals in a Thomas-Fermi Amaldi-Dirac potential and using orbital scaling parameters to optimize the atomic structure of the target. Configurations included: $1s^2 2s^2 2p^6 3s^2 3p^4$, $1s^2 2s^2 2p^6 3p^4 3d^2$, $1s^2 2s^2 2p^6 3p^6$. The scaling parameters we used were applied to the $2p$, $3s$, and $3p$ orbitals and had the following values: $\lambda_{2p} = 1.0194$, $\lambda_{3s} = 1.0413$, and $\lambda_{3p} = 1.067$. There were a total of 53 LS terms in our calculation, leading to 117 j-resolved levels. Note that since we are interested primarily in transitions within the ground term, there is no advantage in including configurations with higher n-shells, as we do not expect their terms to mix with the ground term.

To ensure spectroscopic accuracy, we shifted to NIST energies in stage 3 of the calculation as summarized in table 5.1. The agreement is excellent for the levels of the ground term, with the largest difference found for the excited ^{1}D term.

For the fully-relativistic case, we used the relativistic structure code GRASP to generate the radial orbitals. Configurations included: $1s^2 2s^2 2p^6 3s^2 3p^4$, $1s^2 2s^2 2p^6 3p^4 3d^2$, $1s^2 2s^2 2p^6 3p^6$, $1s^2 2s^2 2p^6 3s 3p^4 3d$, $1s^2 2s^2 2p^6 3s^2 3p^2 3d^2$. As in the semi-relativistic case, we shifted to NIST energies to ensure spectroscopic accuracy. The shifts are summarized in table 5.1. Overall,

Ground configuration: Ar^{2+} $1s^2 2s^2 2p^6 3s^2 3p^4$							
Level	NIST (Ry)	BP (Ry)	BP Diff (Ry)	BP % Diff	Dirac (Ry)	Dirac Diff (Ry)	Dirac % Diff
$^3P_2$	0.00000	0.00000	0.00000	-	0.00000	0.00000	-
$^3P_1$	0.01013	0.01030	0.00017	1.6	0.01013	0.00007	0.6
$^3P_0$	0.01431	0.01462	0.00031	2.1	0.01431	0.00001	0.06
$^1D_2$	0.12767	0.15976	0.03209	20	0.12767	0.02220	13.9
$^1S_0$	0.30314	0.29896	0.00418	1.4	0.30314	0.01071	3.6

Table 5.1: BP and DARC energy levels and comparison with NIST values.

the Dirac structure results were closer to NIST than the Breit-Pauli results, thus the Dirac R-matrix results will represent our recommended dataset for these fine structure transitions. The Breit-Pauli results will provide a useful estimate of the likely uncertainties on the recommended data.

5.3 Cross section comparisons

In Figure 5.2, we show the electron-impact excitation cross section for the $^3P_2 \rightarrow {}^3P_1$ transition, with the black curve showing the results of the Breit-Pauli calculation and the red curve showing the DARC data. In general, these two calculations show very good agreement, with the DARC data generally 3-5% lower than the Breit-Pauli. As expected - given that there is no change in parity in this transition - the cross section is relatively flat and we see that the Rydberg resonance peaks are significant relative to the magnitude of the background. Also of note is that the resonant structure of both calculations is nearly identical, due to the close similarities in the underlying atomic structure.

In Figure 5.3, we show the electron-impact cross section for the $^3P_2 \rightarrow {}^3P_0$ transition, with the black curve showing the results of the Breit-Pauli calculation and the red curve showing the DARC data. Again, these two calculations show good agreement, generally showing the DARC data 6-8% lower than the Breit-Pauli.

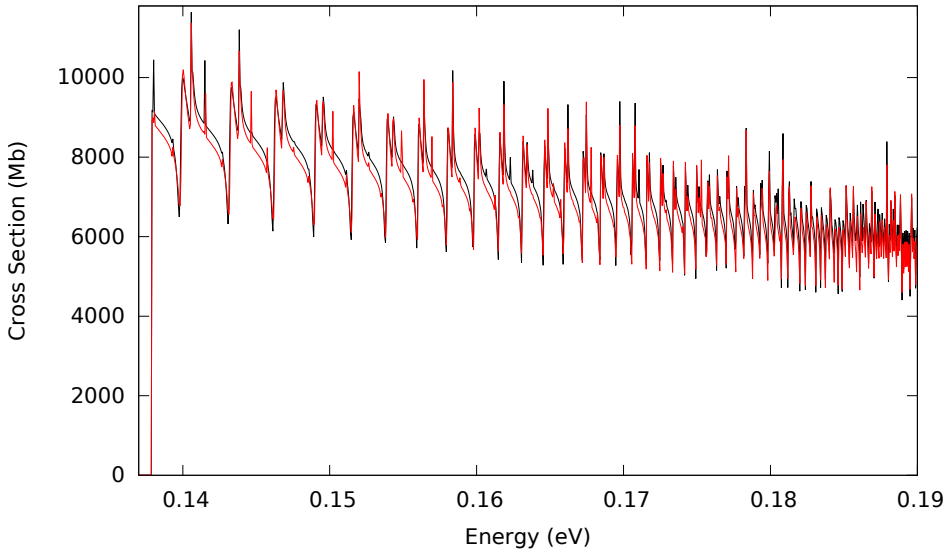

Figure 5.2: Electron-impact excitation cross section for $^3P_2 \rightarrow {}^3P_1$. Solid black curve, BP; Solid red curve, DARC

In Figure 5.4, we show the electron-impact cross section for the $^3P_1 \rightarrow {}^3P_0$ transition, with the black curve representing the results of the Breit-Pauli calculation and the red curve showing the DARC data. Again, these two calculations show agreement within about 6-8%, though there is no trend for one data set being lower than the other. As in the previous transition, the resonance structure shows small variations in energy positions. These differences will contribute to our estimate of the uncertainty on our recommended data.

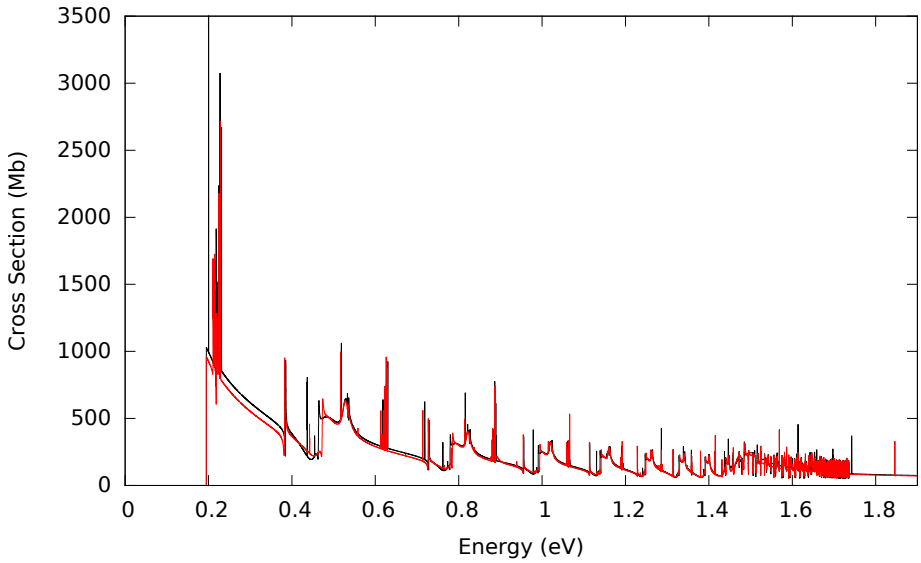

Figure 5.3: Electron-impact excitation cross section for $^3P_2 \rightarrow {}^3P_0$. Solid black curve, BP; Solid red curve, DARC

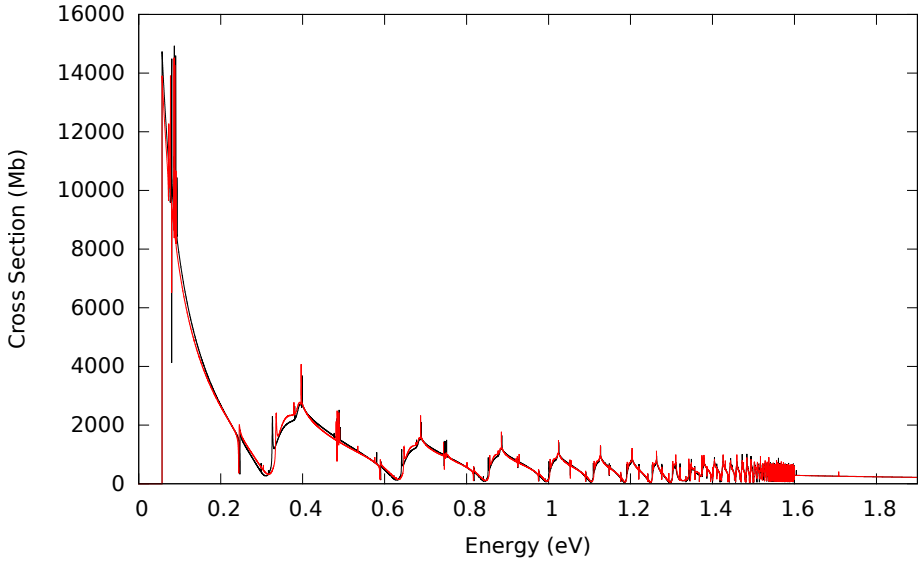

Figure 5.4: Electron-impact excitation cross section for $^3P_1 \rightarrow {}^3P_0$. Solid black curve, BP; Solid red curve, DARC

5.4 Effective Collision Strengths

The consistency of the BP and DARC calculations should provide a lower bound on the error that could be used by modelers to propagate an uncertainty through their spectral modeling codes. We show in this section a comparison of the effective collision strengths for the fine-structure transitions. Note that the differences in these values is caused by differences in the cross sections shown in the previous section. Before a comparison can be made, we first show the convergence checks that were performed.

5.4.1 Convergence

As discussed previously, transitions within the ground term are heavily influenced by the Rydberg resonance structure. This is especially true in low-temperature environments, where the Maxwellian electron distribution peaks at a temperature below the transition threshold. The primary contribution to the integral in equation 1.45 occurs in the high energy tail of the Maxwellian as shown in Fig. 5.5, so the resonance peaks become a significant contributor to the total effective collision strength. Fig 5.6 illustrates how small the electron distribution becomes at 1000 K (purple line), 100 K (blue line), and 10 K (green line). Thus, it is crucial that the energy mesh used in the cross section calculations be fine enough to resolve as much of the resonance structure as possible.

For each of our BP and DARC collision strength calculations, we used a mesh of 20,000, 40,000, and 80,000 energy points to allow for convergence testing. Figures 5.7, 5.8, and 5.9 show the percent difference between the energy meshes for effective collision strengths for the $^3P_2 \rightarrow {}^3P_1$, $^3P_2 \rightarrow {}^3P_0$, and $^3P_1 \rightarrow {}^3P_0$ transitions, respectively. The red line is the percent difference between the 20,000 and 40,000 point calculations and shows an average difference of around 0.5%, while the blue line is the percent difference between the 40,000 and 80,000 point calculations. Since the percent difference has dropped to below 0.1%, we can conclude that the 80,000 point mesh has fully resolved all relevant resonance peaks in these transitions. The relatively large percent differences at the extremely low temperatures

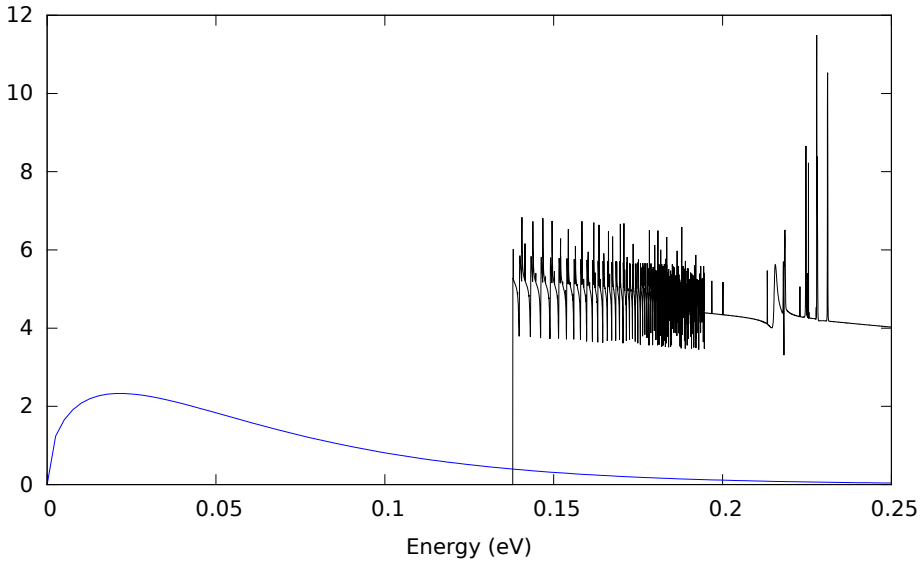

Figure 5.5: The solid blue curve shows the Maxwellian energy distribution for electrons at a temperature of 500K and the solid red curve is sample collision strength data. The overlap region is the primary contributor to the effective collision strength integral.

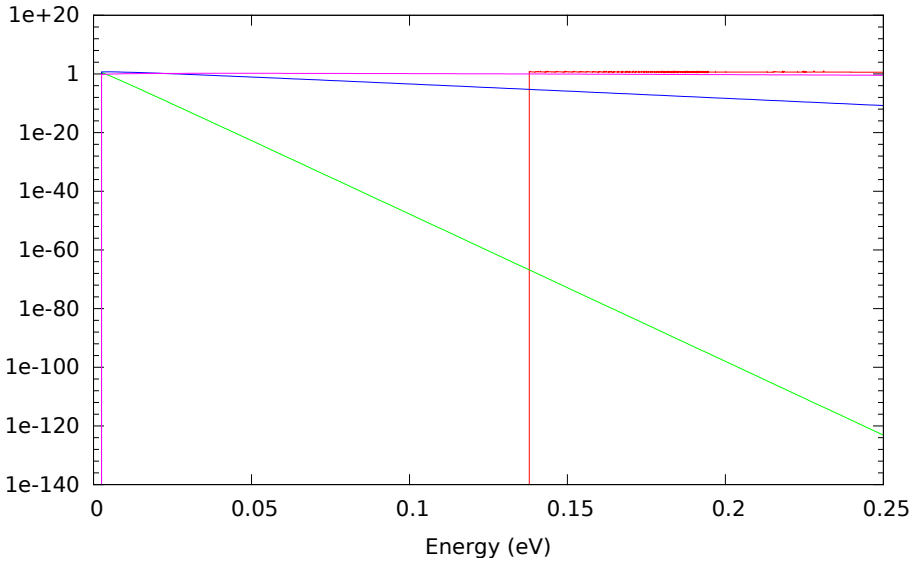

Figure 5.6: The solid green curve shows the Maxwellian energy distribution for electrons at a temperature of 10 K; the solid blue line shows the distribution for 100 K electrons; the solid purple line shows the distribution for 1000 K electrons; the solid red curve is sample collision strength data.

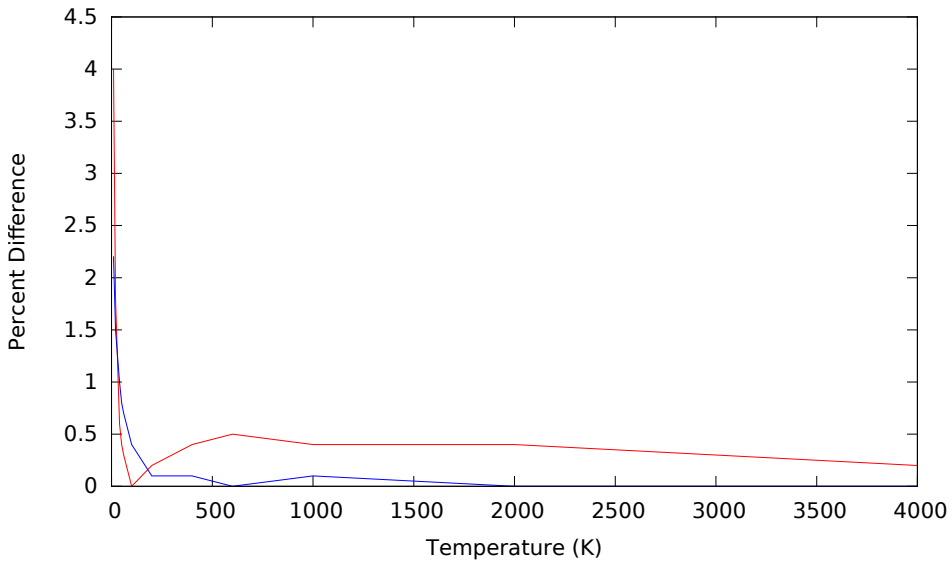

Figure 5.7: Percent difference between 20,000-40,000 point (red curve) and the 40,000-80,000 point (blue curve) effective collision strengths for the BP calculation for the $^3P_2 \rightarrow {}^3P_1$ transition.

(approx. 0-100K) arise from the fact that the finer meshes have slightly different points at which the collision strength calculation has its first non-zero value.

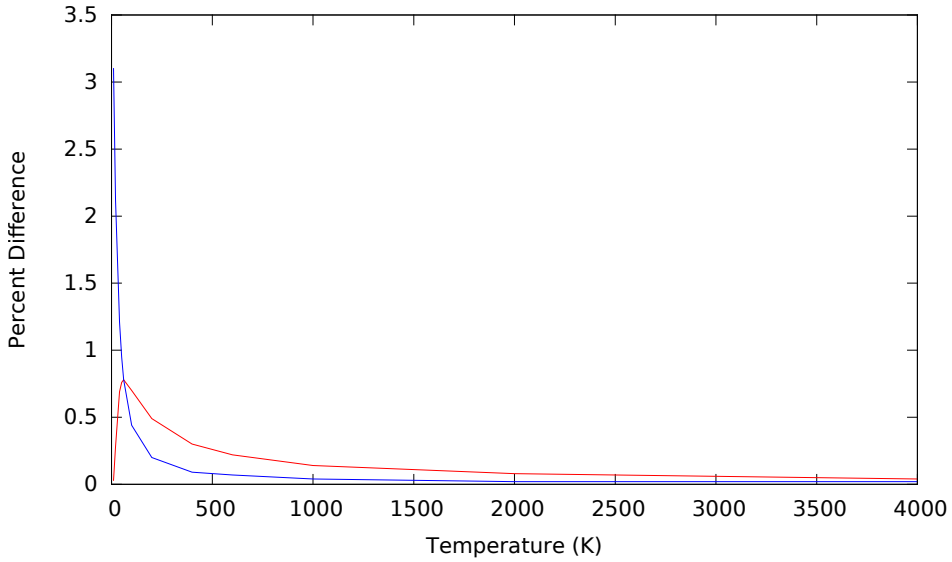

Figure 5.8: Percent difference between 20,000-40,000 point (red curve) and the 40,000-80,000 point (blue curve) effective collision strengths for the BP calculation for the $^3P_2 \rightarrow {}^3P_0$ transition.

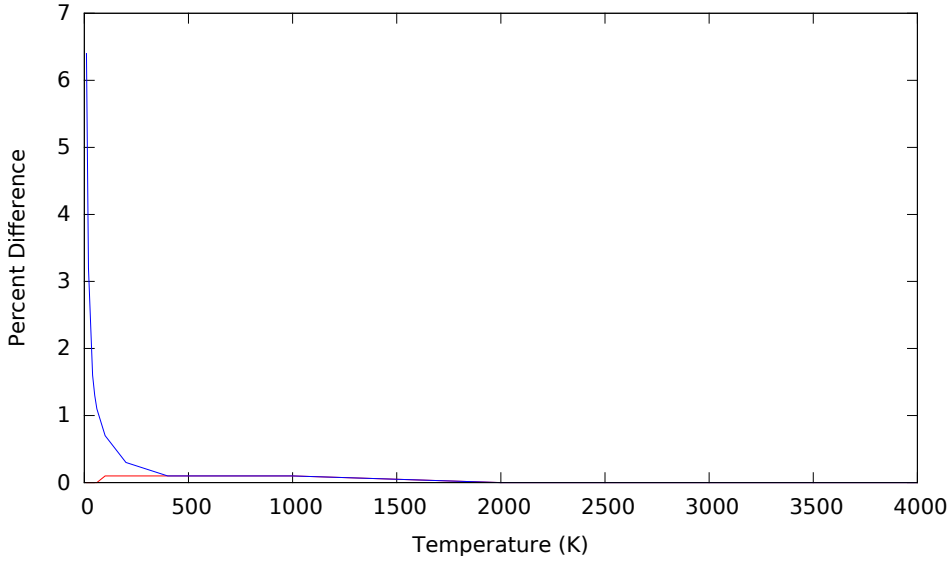

Figure 5.9: Percent difference between 20,000-40,000 point (red curve) and the 40,000-80,000 point (blue curve) effective collision strengths for the BP calculation for the $^3P_1 \rightarrow {}^3P_0$ transition.

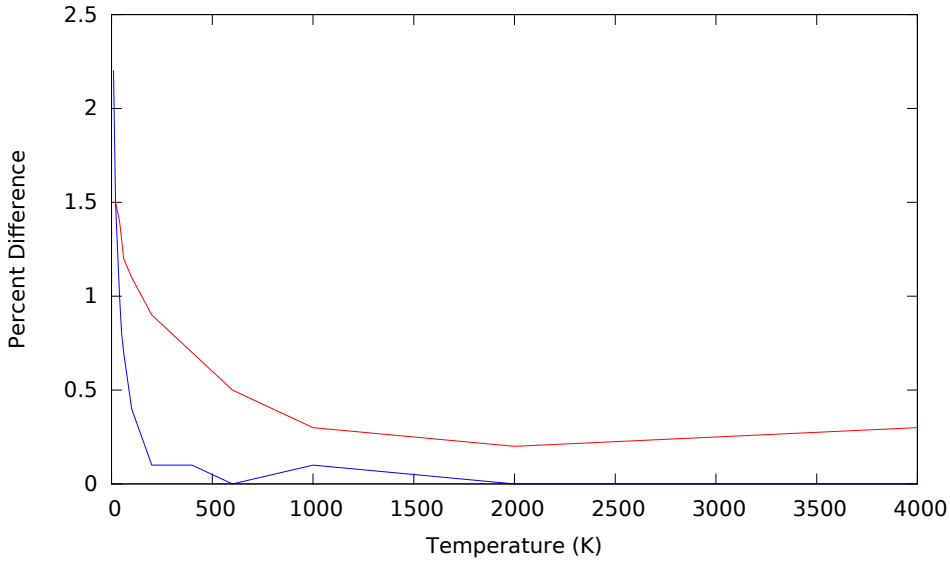

Figure 5.10: Percent difference between 20,000-40,000 point (red curve) and the 40,000-80,000 point (blue curve) effective collision strengths for the DARC calculation for the $^3P_2 \rightarrow {}^3P_1$ transition.

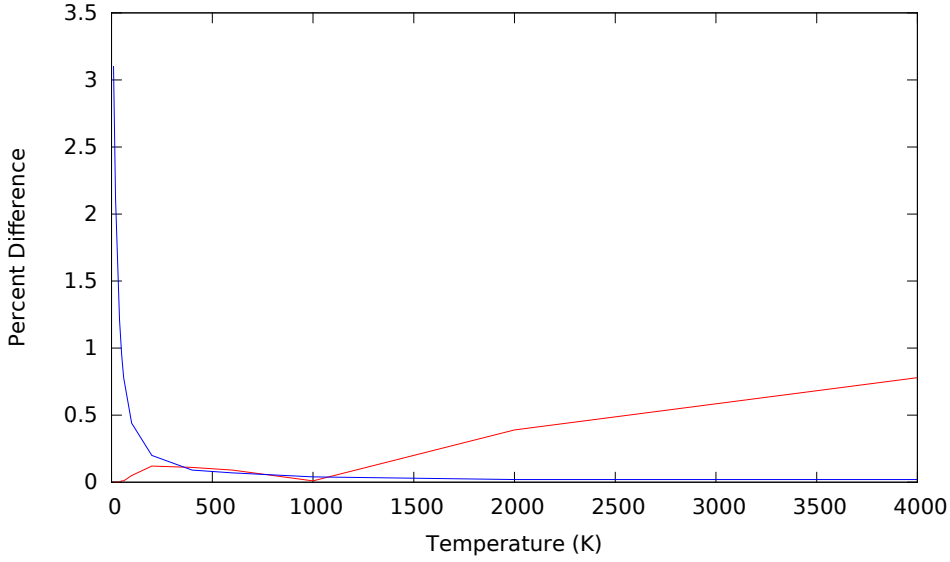

Figure 5.11: Percent difference between 20,000-40,000 point (red curve) and the 40,000-80,000 point (blue curve) effective collision strengths for the DARC calculation for the $^3P_2 \rightarrow {}^3P_0$ transition.

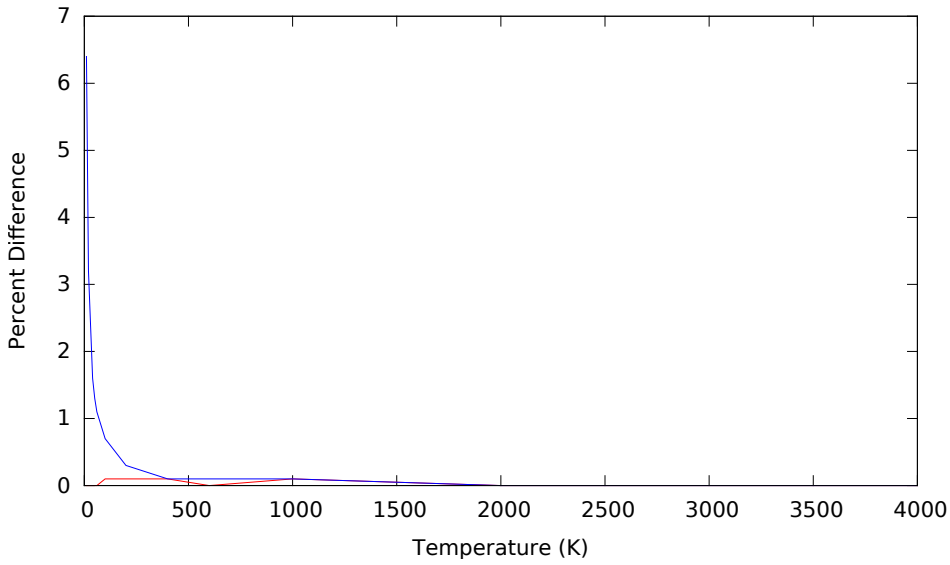

Figure 5.12: Percent difference between 20,000-40,000 point (red curve) and the 40,000-80,000 point (blue curve) effective collision strengths for the DARC calculation for the $^3P_1 \rightarrow {}^3P_0$ transition.

5.4.2 Comparison of Converged Results

In Figure 5.13, we show the effective collision strengths for the $^3P_2 \rightarrow {}^3P_1$ transition, with the black curve showing the results of the Breit-Pauli calculation, the red curve showing the DARC data, and the blue showing the results calculated by Munoz Burgos et al. [5]. The results of our calculations show very good agreement between the DARC and the BP results, with the DARC calculation being consistently 3-4% lower than the BP. This is expected given the similar trend in the cross sections. Our results also show reasonable agreement with that of Munoz, with the largest differences in the BP and DARC results being about 4% and 6%, respectively.

In Figure 5.14, we show the effective collision strengths for the $^3P_2 \rightarrow {}^3P_0$ transition, with the black curve showing the BP results, the red curve showing the DARC data, and the blue showing the results found by Munoz Burgos. The results of our calculations show very good agreement, with the DARC calculation consistently around 5% lower than the BP, which is again expected given the similar trend in the cross sections. Our results begin to diverge more noticeably from that of Munoz with largest differences in the BP and DARC results being about 11% and 16%, respectively. It should be noted that the calculation of Munoz Burgos et al.[5] was not optimized for these fine structure transitions, but was focused on generating data for the higher lying levels.

In Figure 5.15, we show the effective collision strengths for the $^3P_1 \rightarrow {}^3P_0$ transition, with the same color scheme used previously. The results of our calculations are again in very good agreement, with the DARC calculations about 4% lower than the BP, which is again expected. In this transition, our BP results are at worst about 14% higher and our DARC results are about 10% higher than Munoz Burgos et al. [5].

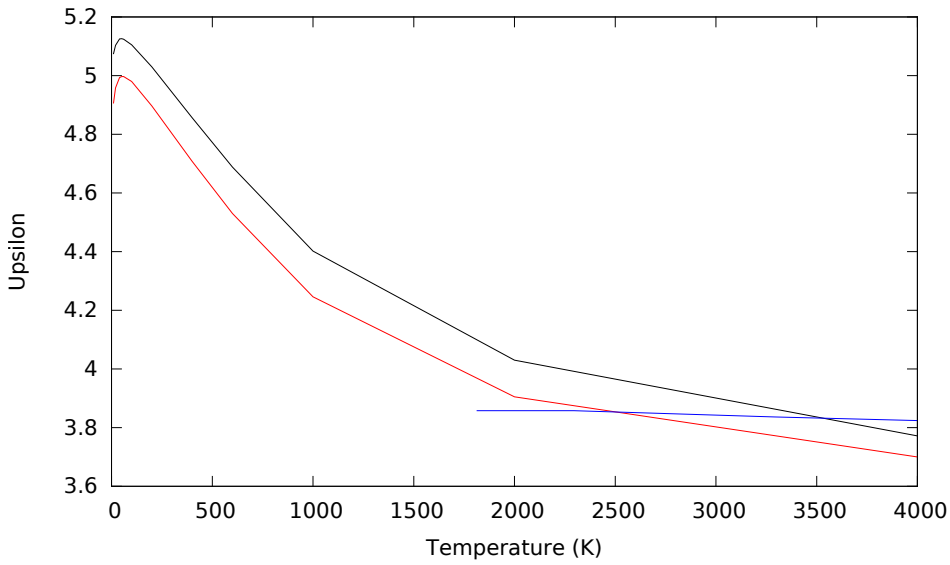

Figure 5.13: Rate coefficients for $^3P_2 \rightarrow {}^3P_1$. Solid red curve, BP; Solid black curve, DARC; Solid blue curve, Munoz

All three of the effective collision strengths show a small bump in the 50K - 100K range with a subsequent decreasing trend in the $^3P_2 \rightarrow {}^3P_1$ and $^3P_1 \rightarrow {}^3P_0$ transitions and a plateau in the $^3P_2 \rightarrow {}^3P_0$ transition through a temperature of 4000K. This is particularly noteworthy because it is not possible to deduce this behavior from the previous work, which emphasizes the need for these calculations when analyzing collisions in low-temperature environments.

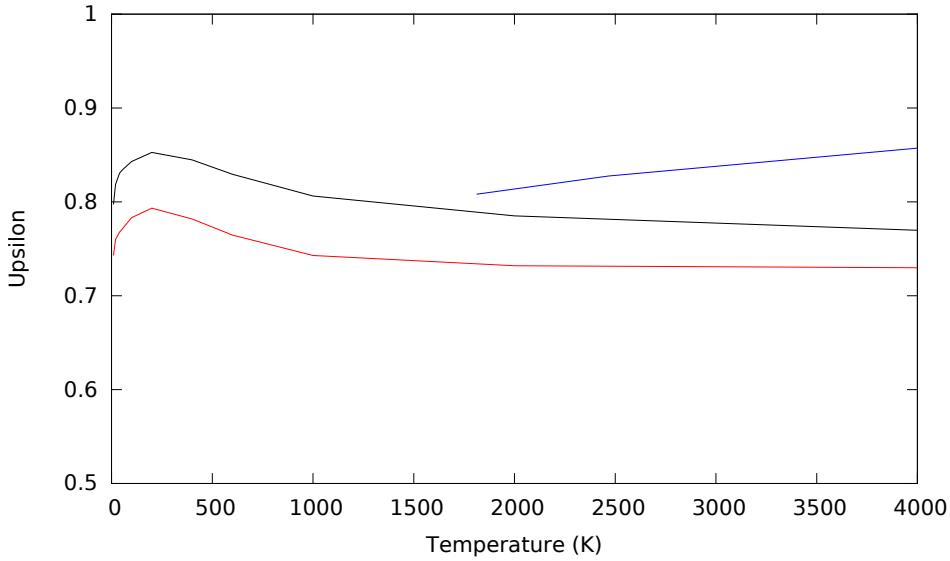

Figure 5.14: Rate coefficients for $^3P_2 \rightarrow {}^3P_0$. Solid red curve, BP; Solid black curve, DARC; Solid blue curve, Munoz

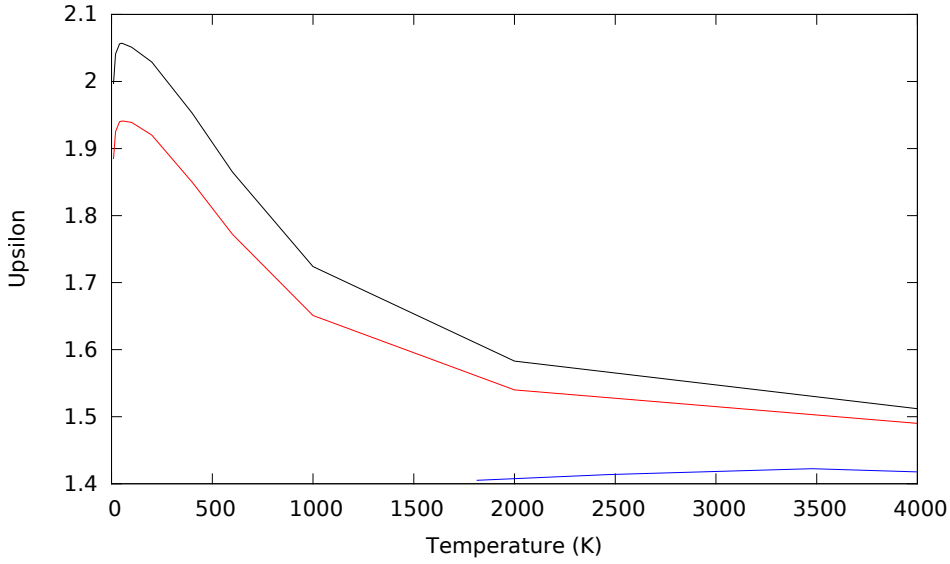

Figure 5.15: Rate coefficients for $^3P_1 \rightarrow {}^3P_0$. Solid red curve, BP; Solid black curve, DARC; Solid blue curve, Munoz

Thus, our recommended dataset consists of the the Dirac R-matrix effective collision strengths and the difference between the Dirac and the Breit-Pauli results provide a lower bound on the uncertainty of the effective collision strength values. This data has been passed on to the astrophysical modelers (along with the uncertainties) and will be combined with proton collision data in the modeling codes.

Chapter 6

Nitrogen ionization - An investigation into final state resolution issues

In this chapter we present term-resolved ionization cross sections for neutral nitrogen. Recently we performed a new RMPS calculation for neutral N and a comparison of some of these results with TDCC calculations has been presented in the literature [50]. There is also a previous B-spline R-matrix calculation [51]. In this chapter we summarize the comparison of these theoretical results and produce a set of recommended cross sections and rate coefficients that are resolved by both the initial and final terms. As part of this investigation a number of interesting issues were discovered regarding the possible final state for some of the excited term ionization processes, these will be discussed in more detail below.

6.1 Overview

Nitrogen has an important application in a number of areas of spectroscopy. In the modeling of auroral emission at 100-200 km, with the metastable ionization of the N atom having potential importance [52]. In controlled fusion energy experiments nitrogen is used to radiatively cool tokamak divertors [53]. The JET- EFDA tokamak found that nitrogen seeding was beneficial in restoring high pedestal temperatures and confinement in their new ITER-like wall configuration [54]. Such experiments require accurate electron-impact ionization cross sections to model the transport of nitrogen in the plasma.

Previous calculations for the electron-impact ionization of the N atom have concentrated on the ground configuration. For example, calculations using the standard Born approximation [55, 56] and the Born-Ochkur approximation [57, 58] are generally found to have a higher

total cross section when compared to a crossed-beams experiment [59]. Recently, B-spline R-matrix with pseudo-states (RMPS) calculations were carried out for the $1s2s^22p^3$ (^4S), (^2D), and (^2P) ground configuration terms of the N atom [51]. The ^4S term calculations from this B-spline R-matrix calculation are in reasonable agreement with experiment [59].

As discussed in Chapter 2, in order to assemble a complete dataset for a given ion charge in the GCR framework it is necessary to resolve both the initial and final states in any ionization processes. However, it is often the case that no data exists for excited state ionization cross sections. In these cases, approximate cross section data for direct ionization is calculated and is based upon some semi-empirical formulae such as the Lotz [60], ECIP [61], or Burgess-Chidichimo [62] methods. The other possibility is to use the n^4 scaling that was discovered by Lee et al [63] and extrapolate data from lower n-shells. Both the semi-empirical approximation methods and the n^4 scaling are based upon the behavior of the ionization potential for the excited states. Typically, small ionization potentials indicate large ionization cross sections. This leads to an interesting scenario that has not been previously studied for certain excited states. If an excited state cannot ionize to the ground of the next ion stage, but instead leads to a metastable state or excited state, care must be taken in the ionization potential used in the above semi-empirical methods. If one were to use inaccurately low ionization potentials for the excited states, there would be a dramatic overestimation of the ionization cross section. This was found to be the case for the $1s^22s2p^2$ configuration of C^{2+}, as shown in chapter 2. For the case of N excited state ionization a larger number of excited states fit this description of being unable to ionize directly to the ground of the next ion stage.

A fundamental assumption in GCR modeling is that the set of ground and metastable levels contains the overwhelming majority of the population in an ion stage, with the effective ionization, recombination and metastable cross-coupling coefficients providing the

connection between them. Thus, resolving the final state of any ionization process is critical. Previous considerations of excited state ionization were for excited states with a single excited electron outside of a core, with this valence shell electron providing the largest ionization cross section for that configuration and leading to a ground state of the next ion stage. This was the basis for the n^4 scaling found previously for excited state ionization [63]. There have been some cases where an inner shell ionization would lead to the population of an excited state of the next ion stage, but these are usually small rate coefficients, and it has been safe to simply assume that they would radiate to the ground and metastable states of that ion stage. Alternatively some ground configurations could ionize to either the ground or metastable states of the next ion stage. Neutral N on the other hand, with the presence of multiple parent terms, has cases where some of the excited states can not ionize to the ground, and determining their final state requires some careful thought. The purpose of this chapter is to use N as an illustration of how to deal with such scenarios. Thus, we will be discussing the generation of final state resolved data for N and at the same time developing a method for dealing with all such future systems in a GCR framework.

Consider the energy level diagram shown in Fig. 6.1. One can see that for neutral N there is a Rydberg series of lines built upon a $2s^22p^2$ (^{3}P) core, a second Rydberg series built upon a $2s^22p^2$ (^{1}D) core and a third series built upon a $2s^22p^2$ (^{1}S) core. The first series has an infinite number of levels, converging onto the ground state ionization potential. The other two only have a small number of terms that are below the ^{3}P ionization potential (4 for the ^1D and 1 for the ^1S). Thus, we can divide the possible ionization processes into four separate categories.

- Direct ionization from the terms of the ground configuration ($2s^22p^3$). In this case the 2p ionization has to terminate in a term of the N^+ ground configuration. These are all considered to be metastable in the GCR framework. Deciding upon how the rate

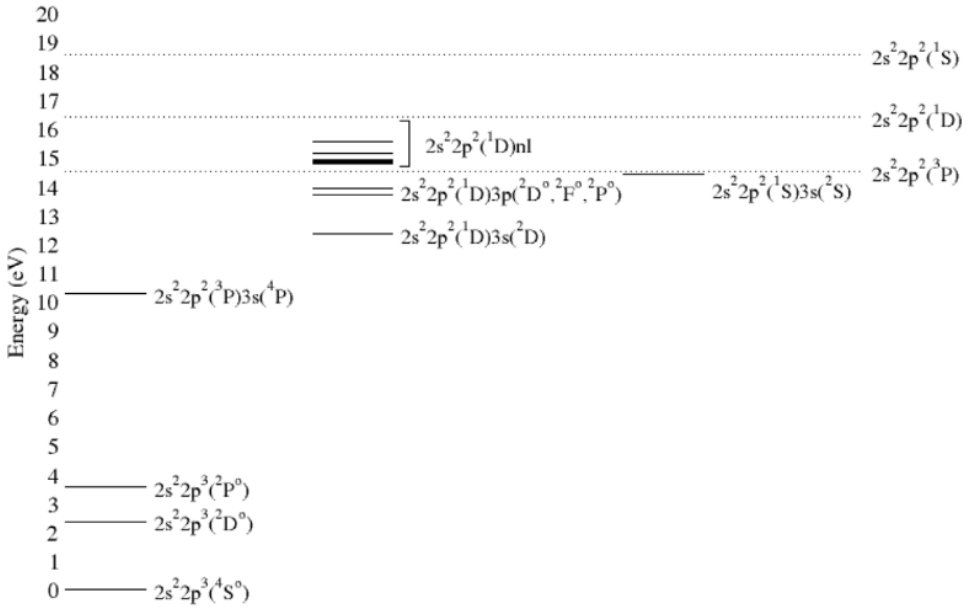

Figure 6.1: Energy level diagram for neutral N, showing the metastable states of N^+. Not shown are the $2s2p^4$ (^4P) terms listed on NIST.

gets split between these ground and metastable terms is the key issue here, which we discuss in section 6.3.

- Direct ionization of the nl electron from the $2s^22p^2(^3P)$ nl Rydberg series. In this case all of the valence shell ionization cross section has to lead to the $2s^22p^2$ (^3P) term of N^+. The issue here is whether there is any predictable n-scaling that can be extracted from our calculations, in a similar manner to previous work on H [49], Be [63], and B [63].

- Direct ionization of the nl electron from the $2s^22p^2(^1D)$ nl and $2s^22p^2(^1S)$ nl Rydberg series. In this case the ionization has to terminate in the $2s^22p^2(^1D)$ and $2s^22p^2(^1S)$ terms of N^+, respectively.

- The role of the terms of the $2s^22p^2(^1D)$ nl and $2s^22p^2(^1S)$ nl configurations that lie above the ^3P ionization potential. These would possibly contribute to excitation-autoionization in lower lying configuration, either through a valence shell excitation or (more interestingly) through an excitation of the core term.

As part of these discussion points, we are also interested in the role of mixing, and expect many terms to be strongly mixed together.

6.2 Description of the TDCC and RMPS calculations

TDCC calculations were carried out for the electron-impact ionization of the $1s^22s^22p^3$, $1s^22s2p^4$, and $1s^22s^22p^23l(l = 0 - 2)$ configurations of the N atom. The details of the calculation can be found in [50]. CADW calculations using the HF ionization potentials were used to top up the TDCC calculations for high angular momentum.

For the work of [50] RMPS calculations were also carried out for the electron-impact ionization of the $1s^22s^22p^3$ (^4S), (^2D), (^2P) LS terms of the ground configuration. Two RMPS calculations were carried out for each term. In model 1, we considered the direct ionization of the 2p orbital. We included 555 $LS\Pi$ terms coming from the 56 configurations of $1s^22s^22p^3$, $1s^22s2p^4$, and $1s^22s^22p^2nl(n = 3 - 12, l = 0 - 5)$. Of the 555 $LS\Pi$ terms, 440 lay above the ionization limit for the lowest (^4S) term. In model 2, we considered the direct ionization of the 2s orbital and indirect ionization contributions coming from $2s \rightarrow nl$ excitation-autoionization. We included 968 $LS\Pi$ terms coming from the 45 configurations of $1s^22s^22p^3$, $1s^22s2p^4$, $1s^22p^5$, and $1s^22s2p^3nl(n = 3-11, l = 0-4)$. Of the 968 $LS\Pi$ terms, 950 lay above the ionization limit for the lowest (^4S) term. Next we consider the different categories of ionization that were outlined previously.

Initial term of $2s^2 2p^3$	Final Term of $2s^2 2p^2$ ^3P	^1D	^1S
^4S	1.0	0	0
^2D	0	0.5	0.5
^2P	0.5	0.27	0.22

Table 6.1: N Angular Factors

6.3 Direct ionization from the terms of the ground configuration ($2s^2 2p^3$)

Figure 6.2 shows the ionization processes for the three terms of the $2s^2 2p^2$ ground configuration, comparing the TDCC and RMPS results. The new RMPS results are in reasonable agreement with the previous B-spline RMPS results, with the new RMPS results being a little higher than the B-spline RMPS results due to extra excitation-autoionization included in the new calculation. The results for the ^4S ionization are in good agreement with the experimental measurements [59]. Note that the TDCC results are configuration-averaged, so are the same on all three plots. It is possible to term-resolve the direct ionization using a set of angular factors [64]. These were evaluated to produce a set of initial and final term resolved TDCC results, see Fig. 6.3. Note that the agreement is not as good as one might have expected. This is due to the final terms being not being pure (an assumption in the angular factor method). If one also includes the mixing coefficients of the final terms then there is good agreement between the TDCC and RMPS results. Note that the $2s^2 2p^3$ (^4S) term has to ionize to the ground term of N^+ ($2s^2 2p^2$ (^3P)), while the ^2D term can go to either of the first two terms of N^+. The ^2P term can ionize to all three terms of the $2p^2$ configuration. Table 6.1 shows the angular factors for the possible initial and final terms for the two ground configurations.

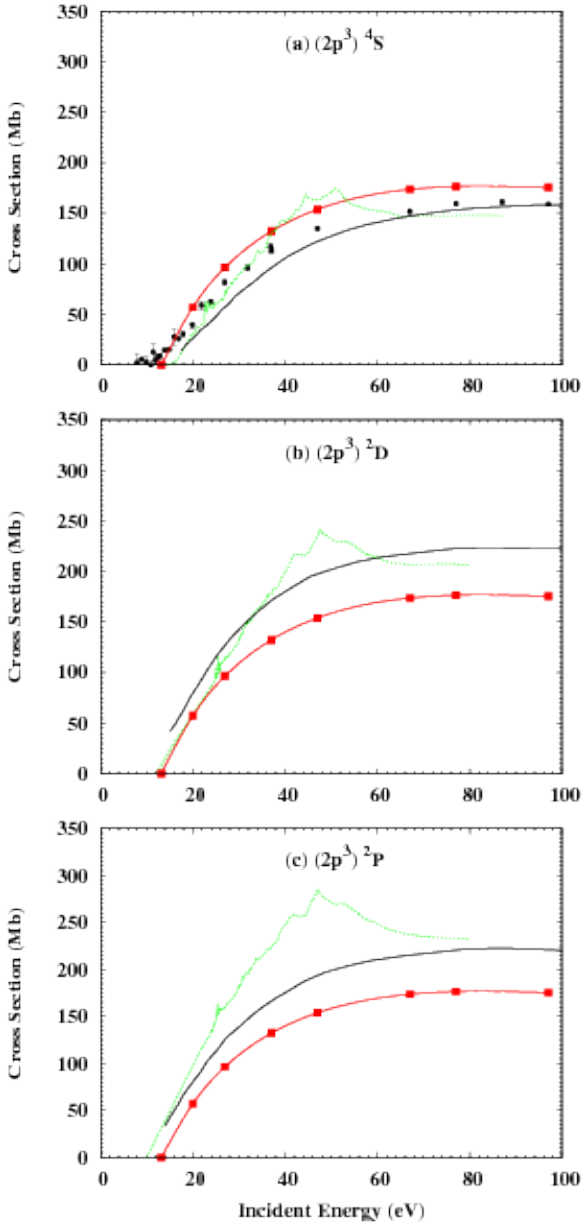

Figure 6.2: Electron-impact ionization of the N(1s 2s^2 2p^2 (^4S), (^2D), and (^2P) LS terms. The solid line shows the B-spline RMPS results for, the dotted line shows the new RMPS results and the solid line with squares shows the TDCC results.

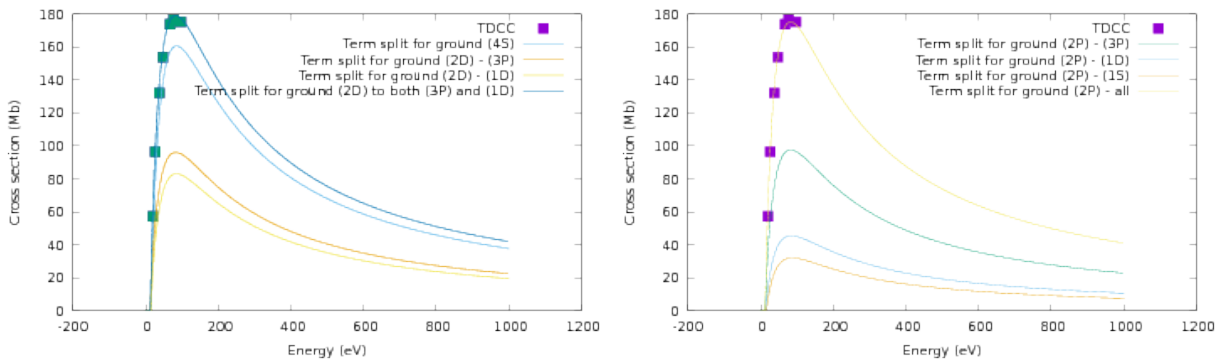

Figure 6.3: Term-resolution of the TDCC cross sections for the ground configuration.

For neutral N, we use the RMPS data as our final recommended data. We note that having both initial and final state resolution in the data means that it can be used directly in any GCR modeling calculations.

6.4 Direct ionization of the nl electron from the $2s^2 2p^2(^3P)$ nl Rydberg series

Figure 6.4 shows a comparison of the TDCC and CADW results for the $2p^2$ 3s, $2p^2$ 3p, and $2p^2$ 3d configurations. Since the valence shell ionization of the $2s^2 2p^2(^3P)$ nl Rydberg series is unlikely to change the term of the core, all of these ionizations have to ionize to the ground term of N^+. There are an infinite number of this Rydberg series, our energy level diagram 6.1 shows just a small number of them. The R-matrix calculation included data up to $nl = 11g$. Our RMPS results have a number of cross sections for this series that produced cross sections that could be used to generate rate coefficients. Thus, these were used to generate rate coefficients to supplement the excitation datafile (adf04 file), with the final state being the ground term of N^+.

The only remaining question on this series is whether we can extrapolate our low n-shell data to higher n-values. It has been previously shown that the direct ionization cross section scales as n^4 at sufficiently high n-shells where the classical behavior would take over. Thus, we checked whether this would be possible from our RMPS results. Unfortunately there were not enough resolved cross sections for the higher n-shells to allow such a scaling law to be explored. A larger calculation in the future would be of great benefit for such a study.

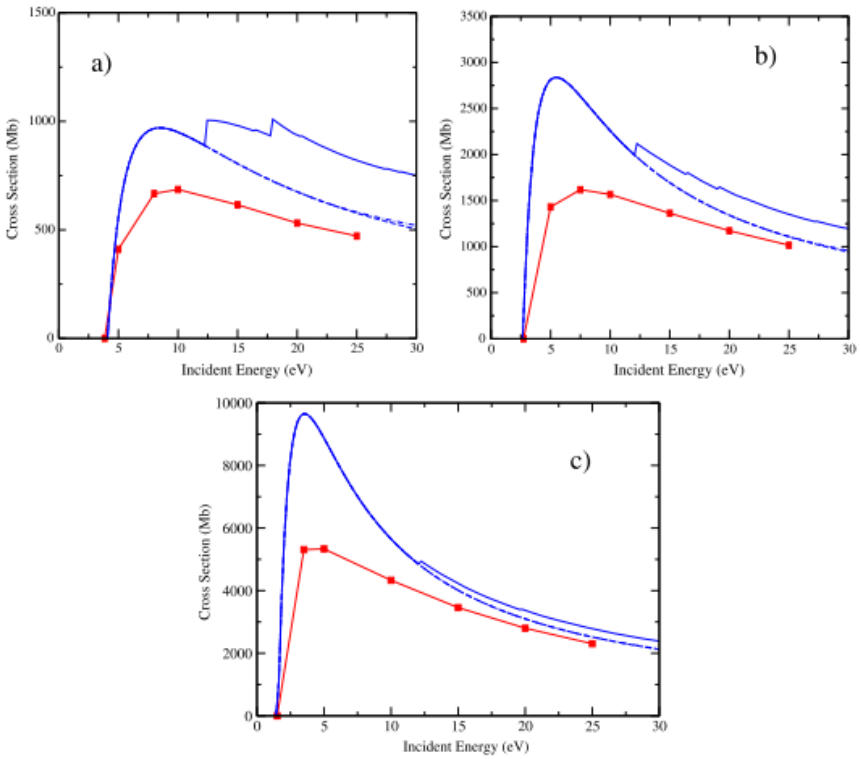

Figure 6.4: Comparison of the TDCC and CADW results for $2p^2$ 3s, $2p^2$ 3p, and $2p^2$ 3d configurations.

6.5 Direct ionization of the nl electron from the $2s^2 2p^2(^1D)$ nl and $2s^2 2p^2(^1S)$ nl Rydberg series

The direct ionization of nl electron for these series has to lead to a final state that is the same as the core term (i.e., the parent term). Thus, the 4 terms for the (^{1}D) nl series and 1 term for the $(^1S)nl$ that are below the ground ionization potential are all of interest in this regard. We extracted some of these cross sections from the R-matrix calculation, to explore the issue of final state resolution. We would expect the valence shell ionization to not be possible to the ground term of N^+, but to terminate on the (^1D) or (^1S) terms of N^+. There is also the interesting possibility that one could get excitation-autoionization contribution starting at a lower energy than the direct ionization process.

6.6 The role of autoionizing terms

For the $2s^2 2p^2(^1D)$ nl and $2s^2 2p^2(^1S)$ nl Rydberg series, excitation of either the core term, or excitation of an nl electron would easily lead to autoionizing configuration. These could ionize to the ground or to metastable ters depending upon their energies. It seems likely that excitation of the core to an excited term, with its low excitation energy, would be more likely to lead to autoinizing levels just above the ground ionization potential, with a subsequent Auger decay resulting in a ground state ion. Resolving such final states in the RMPS calculation is extremely challenging and requires further code development.

Similarly, resolving the final state for the excited state direct ionization for the $2s^2 2p^2(^1D)$ nl and $2s^2 2p^2(^1S)$ nl Rydberg series using the same method as shown for C^+ also requires further code development. While, this is beyond the scope of this project, it would be a fruitful avenue for future research projects. Thus, at the moment it is not clear how much of the excited state RMPS ionization cross section for these excited terms would be due to

excitation-autoionization (which could lead to the ground state or metastable terms of N^+), or direct ionization which would presumably lead to metastable terms in N^+.

Thus, while the generation of final state resolution is not currently possible for N^+, the framework outlined above should provide a useful guide to how to approach the different categories of excited states. To summarize, direct ionization of the $2s^22p^2$ nl configurations would have a contribution to the ground and metastable states of N+ if the core is a ^3P term, and would lead to a metastable state if the core is a ^{1}S or ^{1}D term. Excitation of the core term could lead to autoionizing levels that would Auger to the ground of N^+ and excitation of the nl electron could lead to autoionizing terms that could Auger to the ground or metastable terms, depending upon their energy.

Chapter 7

Conclusions and future work

The work in this dissertation has focused on the calculation of non-perturbative electron-impact data for a number of scenarios. The case of C^+ was considered first, with new electron-impact excitation and ionization data being generated using the R-matrix with pseudostates approach. For both the excitation and ionization cross sections, good agreement was found with the available experimental measurements and the non-perturbative calculations from the literature. For the excitation data currently used in the ADAS database good agreement was found for the lower n-shells ($n < 3$), while large differences were found for the higher n-shells. For the electron-impact ionization cross sections an interesting case for the $1s^2 2s 2p^2$ configuration was explored and it was found that it was not possible for the terms of this configuration to directly ionize to the ground term of C^{2+}. Instead, direct ionization led to the metastable term of C^{2+}. The RMPS cross sections were processed to resolve the final states, with the results being consistent with this picture. It was also found that there was significant excitation-autoionization contributions, leading to the ground term of C^{2+}. We believe that this is the first time that final-state metastable resolved RMPS ionization data has been evaluated. The new atomic data for C^+ was used to generate Generalized Collisional-Radiative Coefficients for C^+, with the results being compared to existing ADAS GCR data.

The case of electron-impact of neutral nitrogen was also investigated. The focus here was not on producing a final dataset, but to explore the issues of final state resolution for this more complicated system. Nevertheless, a number of useful cross sections were extracted. Good agreement was found with literature values and with experimental measurements. The

Time-Dependent Close-Coupling data was term-resolved using angular factors and mixing coefficients. The RMPS data allowed us to explore the issue of excited state ionization. While some states could ionize to the ground and metastable states of N^+, two classes of excited terms could only ionize to metastable states of N^+. The code development required to produce final-state resolution for these cross sections is part of the future work that would be interesting to pursue from this research. Thus, a framework was developed to show what would be expected from such a study.

The R-matrix codes were also used to evaluate fine-structure excitation within the ground term of Ar^{2+}. Rate coefficients were generated at very low temperatures (down to 10 K), for application to the interstellar medium and other low temperature astrophysical objects. Because of the very low temperatures involved, care had to be taken that the atomic structure was as accurate as possible. Thus, optimization was performed for the target system, followed on by both semi- and fully-relativistic R-matrix calculations. The calculations were in good agreement with each other and were used to produce a recommended set of rate coefficient, with the difference in the calculations giving an indication of the likely uncertainties in the calculations. These uncertainties are typically less than 10%.

The future work leading on from this part of the project would be to continue these calculations for other fine-structure transitions of interest to the low temperature astrophysical objects. Other students have recently completed calculations for N, N^+, and Ar^+. Future calculations would include the low charge states of Fe. These electron-impact rate coefficients should be combined with proton-impact rate coefficients and used to model the spectral emission from low temperature astrophysical objects.

Bibliography

[1] H. P. Summers, W. J. Dickson, M. G. O'Mullane, N. R. Badnell, A. D. Whiteford, D. H. Brooks, J. Lang, S. D. Loch, and D. C. Griffin. Ionization state, excited populations and emission of impurities in dynamic finite density plasmas: I. The generalized collisional radiative model for light elements. *Plasma Physics and Controlled Fusion*, 48:263–293, February 2006.

[2] T. Pütterich, R. Neu, R. Dux, A. D. Whiteford, M. G. O'Mullane, and ASDEX Upgrade Team. Modelling of measured tungsten spectra from ASDEX Upgrade and predictions for ITER. *Plasma Physics and Controlled Fusion*, 50(8):085016, August 2008.

[3] T. Pütterich, R. Neu, R. Dux, A. D. Whiteford, M. G. O'Mullane, H. P. Summers, and ASDEX Upgrade Team. Calculation and experimental test of the cooling factor of tungsten. *Nuclear Fusion*, 50(2):025012, February 2010.

[4] J. G. Doyle, H. P. Summers, and P. Bryans. The effect of metastable level populations on the ionization fraction of Li-like ions. *"Astronomy and Astrophysics"*, 430:L29–L32, January 2005.

[5] J. M. Munoz Burgos, S. D. Loch, C. P. Ballance, and R. F. Boivin. VizieR Online Data Catalog: Electron-impact excitation of ArIII (Munoz Burgos+, 2009). *VizieR Online Data Catalog*, 350, April 2009.

[6] L. Lauro-Taroni et al. *Proceedings of the 21st EPS Conference on Controlled Fusion and Plasma Physics*, 1:102, 1994.

[7] S. Wiesen, D. Reiter, V. Kotov, M. Baelmans, W. Dekeyser, A. S. Kukushkin, S. W. Lisgo, R. A. Pitts, V. Rozhansky, G. Saibene, I. Veselova, and S. Voskoboynikov. The new SOLPS-ITER code package. *Journal of Nuclear Materials*, 463:480–484, August 2015.

[8] `http://w3.pppl.gov/transp`.

[9] C. S. Chang, S. Ku, and H. Weitzner. Numerical study of neoclassical plasma pedestal in a tokamak geometry. *Physics of Plasmas*, 11:2649–2667, May 2004.

[10] *The DIII-D National Fusion Program Five-Year Plan*, 2013.

[11] Th. Henning and F. Salama. Carbon in the universe. *Science*, 282(5397):2204–2210, December 1998.

[12] D. G. York. The interstellar medium near the sun. III - Detailed analysis of the line of sight to lambda Scorpii. *"Astrophysical Journal"*, 264:172–195, January 1983.

[13] D. C. Eder. Ionization equilibrium in isolated H II regions. *"Astrophysical Journal"*, 290:244–250, March 1985.

[14] R.E. Stencel, J.L. Linsky, A. Brown, C. Jordan, K.G. Carpenter, R.F. Wing, and S. Czyzak. Density sensitive cii lines in cool stars of low gravity. *Mon. Not. R. Astr. Soc.*, 196:47P–53P, 1981.

[15] E. Avrett, E. Landi, and S. McKillop. Calculated resonance line profiles of [mgii], [cii], and [si iv] in the solar atmosphere. *The Astrophysical Journal*, 779:155–173, 2013.

[16] T.H. Pwa, J.E. Mo, and S.R. Pottasch. Nebular and interstellar absorption lines in planetary nebulae: the case of ngc 6543. *Astron. Astrophys.*, 139:L 1–L 4, 1984.

[17] G.A. Doschek, U. Feldman, and L. Cohen. Chromospheric limb spectra from skylab: 2000 to 3200 a. *The Astrophysical Journal Supplement Series*, 33:101–111, 1977.

[18] J. N. Bahcall and R. A. Wolf. Fine-structure transitions. *Astrophysical Journal*, 152:701, 1968.

[19] A.G.G.M. Tielens and D. Hollenbach. Photodissociation regions i basic model. *Astrophysical Journal*, 291:722–746, 1985.

[20] R. Meijerink, A. E. Glassgold, and J. R. Najita. Atomic Diagnostics of X-Ray-Irradiated Protoplanetary Disks. *"Astrophysical Journal"*, 676:518–531, March 2008.

[21] Ğ. Barinovs, M. C. van Hemert, R. Krems, and A. Dalgarno. Fine-Structure Excitation of C^+ and Si^+ by Atomic Hydrogen. *"Astrophysical Journal"*, 620:537–541, February 2005.

[22] D.W. Savin, L. Allamandola, S. Federman, P. Goldsmith, C. Killbourne, K. Oberg, D. Schultz, and S.W. Weaver, 2010.

[23] P.C. Stancil. In D.R. Shultz, editor, *In proceedings of the 2010 NASA Astrophysics Workshop*, 2011.

[24] V. Stancalie, V. F. Pais, and A. Mihailescu. Fine-structure splitting calculation in the Ar III ion: comparison of perturbative (Breit-Pauli) and non-perturbative (MCDF-EAL) predictions. *European Physical Journal D*, 66:84, March 2012.

[25] D. R. Bates, A. E. Kingston, and R. W. P. McWhirter. Recombination Between Electrons and Atomic Ions. I. Optically Thin Plasmas. *Proceedings of the Royal Society of London Series A*, 267:297–312, May 1962.

[26] E. P. Wigner. Resonance Reactions. *Physical Review*, 70:606–618, November 1946.

[27] E. P. Wigner and L. Eisenbud. Higher Angular Momenta and Long Range Interaction in Resonance Reactions. *Physical Review*, 72:29–41, July 1947.

[28] P. G. Burke and W. D. Robb. The R-Matrix Theory of Atomic Processes. *Advances in Atomic and Molecular Physics*, 11:143–214, 1976.

[29] P.G. Burke and K.A. Berrington, editors. *Atomic and Molecular Processes: An R-Matrix Approach*. Institute of Physics Publishing, 1993.

[30] N. R. Badnell. A Breit-Pauli distorted wave implementation for AUTOSTRUCTURE. *Computer Physics Communications*, 182:1528–1535, July 2011.

[31] D.C. Griffin and M.S. Pindzola. Non-perturbative quantal methods for electron-atom scattering processes. *Adv. At. Mol. Phys.*, 54:203–235, 2006.

[32] K.G. Dyall, I.P. Grant, C.T. Johnson, F.A. Parpia, and E.P. Plummer. Grasp: A general-purpose relativistic atomic structure program. *Computer Physics Communications*, 55(3):425–456, October 1989.

[33] J.A. Ludlow, S.D. Loch, M.S. Pindzola, C.P. Ballance, D.C. Griffin, M.E. Bannister, and M. Fogle. Electron-impact ionization of c^+ in both ground and metastable states. *Phys. Rev. A*, 78, 2008.

[34] C.P. Ballance, S.D. Loch, J.A. Ludlow, Sh.A. Abdel-Naby, and M.S. Pindzola. Electron-impact ionization of c^+ excited states. *Phys. Rev. A*, 84, 2011.

[35] A. Burgess, D. G. Hummer, and J. A. Tully. Electron Impact Excitation of Positive Ions. *Royal Society of London Philosophical Transactions Series A*, 266:225–279, April 1970.

[36] I. Yamada, A. Danjo, T. Hirayama, A. Matsumoto, S. Ohtani, H. Suzuki, T. Takayanagi, H. Tawara, K. Wakiya, and M. Yoshino. *J. Phys. Soc. Jpn.*, 58:1585, 1989.

[37] S.S. Tayal. Electron impact excitation collision strength for transitions in cii. *A&A*, 486:629–636, 2008.

[38] F.P. Keenan, D.J. Lennon, C.T. Johnson, and A.E. Kingston. Fine-structure population ratios for the ^{2}p ground state of cii. *Mon. Not. R. Astr. Soc.*, 220:571–576, 1986.

[39] D. Luo and A.K. Pradhan. R-matrix calculations for electron-impact excitation of c^+, n^2+, and o3+ including fine structure. *Phys. Rev. A*, 41(1):165–173, 1990.

[40] R.D. Blum and A.K. Pradhan. Rate coefficients for the excitation of infrared and ultraviolet lines in cii, niii, and oiv. *The Astrophysical Journal Supplement Series*, 80:425–452, 1990.

[41] N.J. Wilson and K.L. Bell. Effective collision strengths for ground-state and $2s^22p$-$2s2^2$ fine-structure transitions in cii. *Mon. Not. R. Astron. Soc.*, 337:1027–1034, 2002.

[42] N.J. Wilson, K.L. Bell, and C.E. Hudson. Effective collision strengths for electron impact excitation of cii. *A&A*, 432:731–736, 2004.

[43] S.J. Smith, M. Zuo, A. Chutjian, S.S. Tayal, and I.D. Williams. Electron excitation cross sections for the cii transitions. *The Astrophysical Journal*, 463:808–817, 1996.

[44] H. L. Zhang and D. H. Sampson. Relativistic Distorted-Wave Collision Strengths and Oscillator Strengths for the 105 Δn = 0 Transitions with n = 2 in the 85 B-Like Ions with 8 <= Z <= 92. *Atomic Data and Nuclear Data Tables*, 56:41–104, January 1994.

[45] G.P. Lafyatis and J.L. Kohl. Measurement of electron-impact excitation in boronlike carbon. *Phys. Rev. A*, 36(1):59–65, 1987.

[46] I.D. Williams, J.B. Greenwood, B. Sringengan, R.W. O'Neill, and I.G. Hughes. A technique for absolute measurements in near threshold excitation of positie ions: application to excitation of c+. *Meas. Sci. Technol.*, 9:930–938, 1998.

[47] N. R. Badnell, M. G. O'Mullane, H. P. Summers, Z. Altun, M. A. Bautista, J. Colgan, T. W. Gorczyca, D. M. Mitnik, M. S. Pindzola, and O. Zatsarinny. Dielectronic recombination data for dynamic finite-density plasmas. I. Goals and methodology. *"Astronomy & Astrophysics"*, 406:1151–1165, August 2003.

[48] S. M. Younger. Electron impact ionization cross sections and rates for highly ionized atoms. *"Journal of Quantitative Spectroscopy and Radiative Transfer"*, 26:329–337, 1981.

[49] S. D. Loch, C. P. Ballance, M. S. Pindzola, and D. P. Stotler. The role of excited state ionization data on H and He generalized collisional-radiative coefficients. *Plasma Physics and Controlled Fusion*, 51(10):105006, October 2009.

[50] S A Abdel-Naby, M S Pindzola, A J Pearce, C P Ballance, and S D Loch. Electron-impact ionization of the n atom. *Journal of Physics B: Atomic, Molecular and Optical Physics*, 48(2):025203, 2015.

[51] Y. Wang, O. Zatsarinny, and K. Bartschat. B-spline R-matrix-with-pseudostates calculations for electron-impact excitation and ionization of nitrogen. *"Physical Review A"*, 89(6):062714, June 2014.

[52] S. H. Pandya and K. N. Joshipura. Ionization of metastable nitrogen and oxygen atoms by electron impact: Relevance to auroral emissions. *Journal of Geophysical Research (Space Physics)*, 119:2263–2268, March 2014.

[53] R. Neu, A. Kallenbach, M. Balden, V. Bobkov, J. W. Coenen, R. Drube, R. Dux, H. Greuner, A. Herrmann, J. Hobirk, H. Höhnle, K. Krieger, M. Kočan, P. Lang, T. Lunt, H. Maier, M. Mayer, H. W. Müller, S. Potzel, T. Pütterich, J. Rapp, V. Rohde, F. Ryter, P. A. Schneider, J. Schweinzer, M. Sertoli, J. Stober, W. Suttrop, K. Sugiyama, G. van Rooij, and M. Wischmeier. Overview on plasma operation with a full tungsten wall in ASDEX Upgrade. *Journal of Nuclear Materials*, 438:S34–S41, July 2013.

[54] F. Romanelli and J. EFDA Contributors. Overview of the JET results with the ITER-like wall. *Nuclear Fusion*, 53(10):104002, October 2013.

[55] E. J. McGuire. Inelastic Scattering of Electrons and Protons by the Elements He to Na. *"Physical Review A"*, 3:267–279, January 1971.

[56] K. Omidvar, H. L. Kyle, and E. C. Sullivan. Ionization of Multielectron Atoms by Fast Charged Particles. *"Physical Review A"*, 5:1174–1187, March 1972.

[57] G. Peach. Ionization of neutral atoms with outer 2p, 3s and 3p electrons by electron and proton impact. *Journal of Physics B Atomic Molecular Physics*, 3:328–349, March 1970.

[58] G. Peach. Ionization of atoms and positive ions by electron and proton impact. *Journal of Physics B Atomic Molecular Physics*, 4:1670–1677, December 1971.

[59] E. Brook, A. C. H. Smith, and M. F. A. Harrison. Measurements of the electron impact ionisation cross sections of He, C, O and N atoms. *Journal of Physics B Atomic Molecular Physics*, 11:3115–3132, September 1978.

[60] W. Lotz. An empirical formula for the electron-impact ionization cross-section. *Zeitschrift fur Physik*, 206:205–211, April 1967.

[61] A. Burgess and H. P. Summers. The recombination and level populations of ions. I - Hydrogen and hydrogenic ions. *"Monthly Notices of the RAS"*, 174:345–391, February 1976.

[62] A. Burgess and M. C. Chidichimo. Electron impact ionization of complex ions. *"Monthly Notices of the RAS"*, 203:1269–1280, June 1983.

[63] T.-G. Lee, S. D. Loch, C. P. Ballance, J. A. Ludlow, and M. S. Pindzola. Electron-impact-ionization cross sections for excited states of B^{q+} (q=0-2) and an investigation into n scaling of ionization cross sections. *"Physical Review A"*, 82(4):042721, October 2010.

[64] D. H. Sampson. Branching ratios for excitation to highly excited levels or ionization of complex ions. *"Physical Review A"*, 34:986–1006, August 1986.